

3460,

JNCASR
Acc. No. 3460
LIBRARY

LIBRARY
JAWAHARLAL NEHRU CENTRE
FOR ADVANCED SCIENTIFIC RESEARCH
JAKKUR POST
BANGALORE - 560 064

JNCASR
620.193 P04



LIBRARY
JAWAHARLAL NEHRU CENTRE
FOR ADVANCED SCIENTIFIC RESEARCH
JAKKUR POST
BANGALORE - 560 064

New Strategies for the Synthesis and Characterization of Nanotubes and Nanowires

A THESIS SUBMITTED IN PARTIAL FULFILMENT
For OF THE DEGREE OF
MASTER OF SCIENCE
AS A PART OF THE INTEGRATED Ph.D. PROGRAMME

by

S. R. C. Vivek Chand



CHEMISTRY AND PHYSICS OF MATERIALS UNIT
JAWAHARLAL NEHRU CENTRE FOR ADVANCED SCIENTIFIC
RESEARCH

Bangalore – 560 064

APRIL 2004

620193
P04

LIBRARY
JAWAHARLAL NEHRU CENTRE
FOR ADVANCED SCIENTIFIC RESEARCH
JAKKUR POST
BANGALORE - 560 064

Dedicated to my parents

DECLARATION

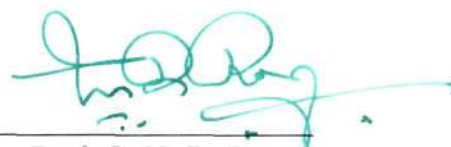
I hereby declare that the matter embodied in the thesis entitled “**New Strategies for the Synthesis and Characterization of Nanotubes and Nanowires**” is the result of investigations carried out by me at the Chemistry and Physics of Materials Unit, Jawaharlal Nehru Centre for Advanced Scientific Research, Bangalore, India under the supervision of Prof. C. N. R. Rao and that it has not been submitted elsewhere for the award of any degree or diploma.

In keeping with the general practice in reporting scientific observations, due acknowledgement has been made whenever the work described is based on the findings of other investigators.


S. R. C. Vivek Chand

CERTIFICATE

I hereby certify that the matter embodied in this thesis entitled “**New Strategies for the Synthesis and Characterization of Nanotubes and Nanowires**” has been carried out by Mr. S. R. C. Vivek Chand at the Chemistry and Physics of Materials Unit, Jawaharlal Nehru Centre for Advanced Scientific Research, Bangalore, India under my supervision and that it has not been submitted elsewhere for the award of any degree or diploma.



Prof. C. N. R. Rao
(Research Supervisor)

Acknowledgements

- ◇ I express my sincere gratitude to Prof. C. N. R. Rao, F.R.S. for suggesting the problems, invaluable guidance, constant encouragement and moral support. His enthusiasm and passion for doing science has inspired me in taking up experimental research. I am extremely fortunate to work with him. He has not just been a research supervisor, but a real father figure for me. I am extremely grateful to him for his keen interest in my academic and personal welfare.
- ◇ It has been a great pleasure working with Dr. Govindaraj. I am extremely grateful to him for teaching me the various aspects of experimental research and for his constant encouragement throughout the project work.
- ◇ I thank Anil, Basavaraj, Srinath, Srinivas, Vasu and Usha madam for their help in various measurements. I also thank Kavitha, Motin and Dr. Chandrabhas for the Raman spectroscopic measurement. I would like to thank Dr. Raju for his immense help during the NSP work.
- ◇ I thank my collaborators Dr. Sudheendra, Leonard, Gautam and Leskey Cele for their invaluable help.
- ◇ I thank my teachers both in IISc and JNC especially Profs. K. L. Sebastian, T. N. Guru Row, J. Gopalakrishnan, P. K. Das, A. G. Samuelson, S. Chandraskharan, P. Balaram, S. Yashonath, M. S. Hegde, A. Umarji, A. R. Chakravarthy, S. Narasimhan and G. U. Kulkarni for their informative courses.
- ◇ I would like to thank my lab mates, Gautam, Leonard, Kalyani and Dr. Manashi for their fruitful discussions and wonderful work atmosphere.

- ◇ I also thank my friends, Leo, Gautam, Sudhee, Vinod, Kalyani, Neena, Reji, John, Pushpa, Lakshmi, Thiru, Dash, Selvi, Jaya, Kabra, Kapoor, Rinki, Ved, Arun, Mandal, Sandeep, Kirthi, Jamal and my IISc batchmates especially Praveen, Girish, Tinku, Animesh, Arnab, Subhas, Asish Pal and Rudra. I also thank my batchmate Ayan for the wonderful time we have had in the last 3 years.
- ◇ I also thank Deepak, Meenakshi and Prit for all their help and affection. I also thank Nikki for always being there with me.
- ◇ I also thank my seniors Dr. Anupama and Dr. Vaidhyanathan for their help and suggestions during course-work.
- ◇ I thank Dr. Waghmare, Rajesh and Shithal for the excellent Computer facilities provided.
- ◇ I also thank Vinod, John and Leonard for their help during the course of writing this thesis.
- ◇ I would like to thank Mrs. Rao and Mr. Sanjay for their love and care towards me.
- ◇ Finally, I would like express by deepest regards to my parents, sister and Susee for their love, patience, understanding and motivation.

New Strategies for the Synthesis and Characterization of Nanotubes and Nanowires (Synopsis)¹

Carbon nanotubes and nanowires constitute an important class of nanomaterials and are excellent models to study the relationship between electrical transport, optical and other properties with dimensionality and size confinement. Chapter 1 presents a brief overview of the synthesis, properties and potential applications of carbon nanotubes as well as nanowires.

The use of nebulized spray pyrolysis for the synthesis of carbon nanotubes is outlined in Chapter 2. Multi-walled carbon nanotubes (MWNTs) with fairly uniform diameters and aligned MWNT bundles have been obtained by using solutions of organometallics such as ferrocene in hydrocarbon solvents. Well-graphitized MWNTs were obtained with a solution of ferrocene in xylene. Single-walled nanotubes (SWNTs) were obtained when cobaltocene or nickelocene is used along with toluene. $\text{Fe}(\text{CO})_5$ in mixture with acetylene also yielded aligned MWNT bundles. The procedure described can be scaled up for large-scale production.

Chapter 3 discusses the purification of single-walled carbon nanotubes (SWNTs) and MWNTs by hydrogen treatment. The method involves acid washing followed by hydrogen treatment around 1000 °C. While acid washing dissolves the metal particles, the hydrogen treatment removes amorphous carbon as well as the carbon coating on the metal nanoparticles. The high quality of the nanotubes obtained after purification has been verified by electron microscopy, X-ray diffraction and spectroscopic methods.

Chapter 4 discusses a new method based on nebulized spray pyrolysis for

¹Papers based on the above studies have been published in *J. Nanoscience and Nanotechnology*, 2, 631 (2002), *Proc. Ind. Acad. Sci. (Chem. Sci.)*, 115, 509 (2003) and *Chem. Phys. Lett.* 386, 313 (2004). A Communication has been accepted for publication in *J. Phys. Chem.*(2004). Another communication has been submitted for publication.

the preparation of nanowires of metals. The method, involving the decomposition of the metal acetate precursor for the synthesis of zinc, cadmium and lead nanowires. The nanowires are obtained in copious quantities and are single-crystalline. Oxidation of metal nanowires gives one-dimensional oxidic nanostructures. In the case of zinc metal, tubular ZnO is obtained.

Chapter 5 deals with polyaniline (PANI)- carbon nanotubes composites. Composites of PANI have been prepared with pristine multi-walled and single-walled nanotubes as well as nanotubes subjected to acid treatment and subsequent reaction with thionyl chloride. The composites have been characterized by various techniques, including X-ray diffraction, electron microscopy as well as infrared and Raman spectroscopy. Electrical resistivities of the PANI-nanotube composites have been measured and compared with those of the nanotubes and PANI.

Contents

Acknowledgements	v
Synopsis	vii
1 Nanotubes and Nanowires: An Introduction	1
1.1 Fullerenes and carbon nanotubes	2
1.2 Nanowires	13
2 Carbon Nanotubes by Nebulized Spray Pyrolysis	19
2.1 Introduction	19
2.2 Nebulized Spray Pyrolysis	20
2.3 Experimental	22
2.4 Results and Discussion	23
2.5 Conclusions	39
3 A new method of purification of carbon nanotubes based on hydrogen treatment	41
3.1 Introduction	41
3.2 Experimental	43
3.3 Results and Discussion	45
3.4 Conclusion	54
4 A new method for the preparation of metal nanowires by the nebulized spray pyrolysis of precursors	57
4.1 Introduction	57
4.2 Experimental	58
4.3 Results and Discussion	59
4.4 Conclusions	70

5	Polyaniline-carbon nanotube composites	71
5.1	Introduction	71
5.2	Experimental	72
5.3	Results and Discussion	74
5.4	Conclusions	81
	Bibliography	83

Chapter 1

NANOTUBES AND NANOWIRES: AN INTRODUCTION

Understanding the properties of nanometer sized objects is one of the important challenges in modern scientific era. Accordingly, there has been a large interest in the synthesis and study of clusters, nanocrystals, nanotubes, nanowires and other nanomaterials [1]. Initial efforts towards this goal started with Michael Faraday in the 19th century [2]. Faraday studied colloids of gold and termed them as "divided metals", now popularly known as nanoparticles. The properties of nanosized materials are quite different from that of bulk and these differences arise as there are more atoms on the surface (i.e. large surface/volume ratio). For example, the variation of bandgap of different semiconductor nanocrystals as a function of diameter is shown in Figure 1.1. One observes an increase in the bandgap as the diameter of the nanoparticle decreases. Very small nanoparticles (or clusters) behave like molecules with discrete energy levels. The properties of a nanosystem can also be modified by changing the shape(or dimension). The effect of dimension on the electronic structure of a material is illustrated in Figure 1.2. The nanoparticles are zero-dimensional and exhibit molecule like behavior. Two dimension nanomaterials such as thin films exhibit steps in their electronic density of states (DOS) while van Hove singularities (sharp spikes) are observed in the case of one-dimensional analogues. It is generally accepted that quantum confinement of electrons by the potential wells of nanometer-sized structures may provide one of the most powerful means to control electrical, optical, magnetic and thermoelectric properties of a solid

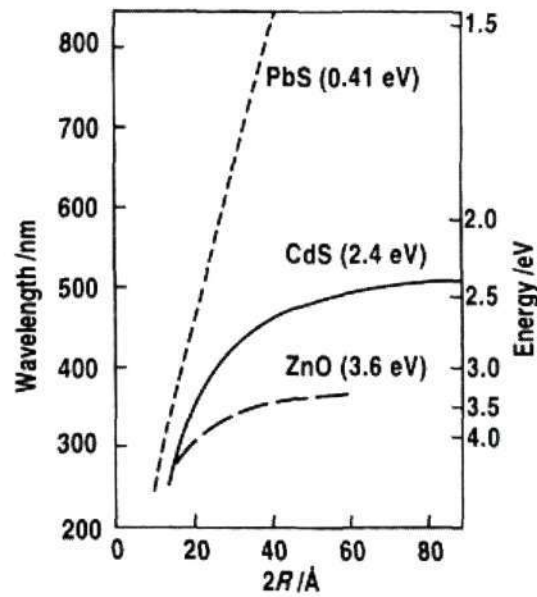


Figure 1.1: Variation of bandgap of semiconductor nanoparticles as a function of their diameter.

state functional material [3]. The ability to tune the properties by controlling the size and shape makes them attractive for potential future application in various fields. In this chapter, a brief summary of the current understanding of the various synthetic methodologies, properties and phenomena associated with one-dimensional nanomaterials such as carbon nanotubes and their inorganic analogues, nanowires are described.

1.1 Fullerenes and carbon nanotubes

Ever since the discovery of fullerenes in 1985 by Kroto *et al.* [4] there has been an enormous interest in the synthesis and properties of carbon nanomaterials. Fullerenes are clusters of carbon with three coordinate carbon atoms tiling the spherical or nearly spherical surfaces, the best known example C_{60} , with a truncated icosahedral structure formed by twelve pentagonal rings and twenty hexagonal rings. The coordination at every carbon atom is not

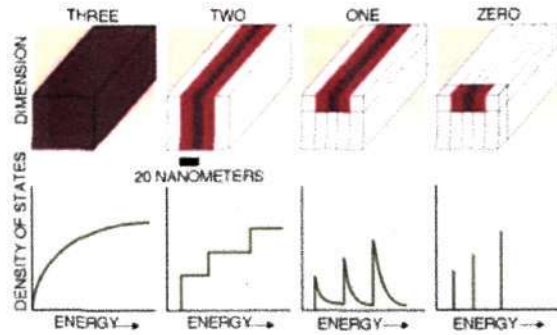


Figure 1.2: Effect of dimension on the electronic properties of a metallic system.

planar, slightly pyramidalized, with some sp^3 character present in the essentially sp^2 carbons. The curvature needed for the formation of closed structure is due to the presence of five-member rings. Computer generated models of various fullerene molecules are shown in Figure 1.3. Fullerenes can be produced in large quantities by the arc evaporation of graphite [5]. Carbon nanotubes, the nearly one-dimensional analogue of fullerenes were discovered by Iijima [6]. Nanotubes can be multi-walled with a central tubule surrounded by graphitic layers separated at approximately 3.4 \AA . A single-walled carbon nanotube (SWNTs) unlike multi-walled carbon nanotubes (MWNTs) consist of a single tubule without additional graphitic layers. Transmission electron micrograph of MWNTs are given in Figure 1.4.

Several methods for the synthesis of carbon nanotubes have been developed. MWNTs have been traditionally prepared by the arc evaporation of graphite [6]. A current of 60-100 A across a potential drop of about 25 V gives high yields of carbon nanotubes. Carbon nanotubes have been produced in large quantities using plasma arc-jets, by optimizing the quenching process in an arc between a graphite anode and a cooled copper electrode [7]. Single-walled carbon nanotubes (SWNTs) were first synthesized by metal-catalyzed dc-arc of graphite electrodes [8,9]. The graphite anode is normally filled with metal powders such as Fe, Co or Ni and pure graphite is used as the

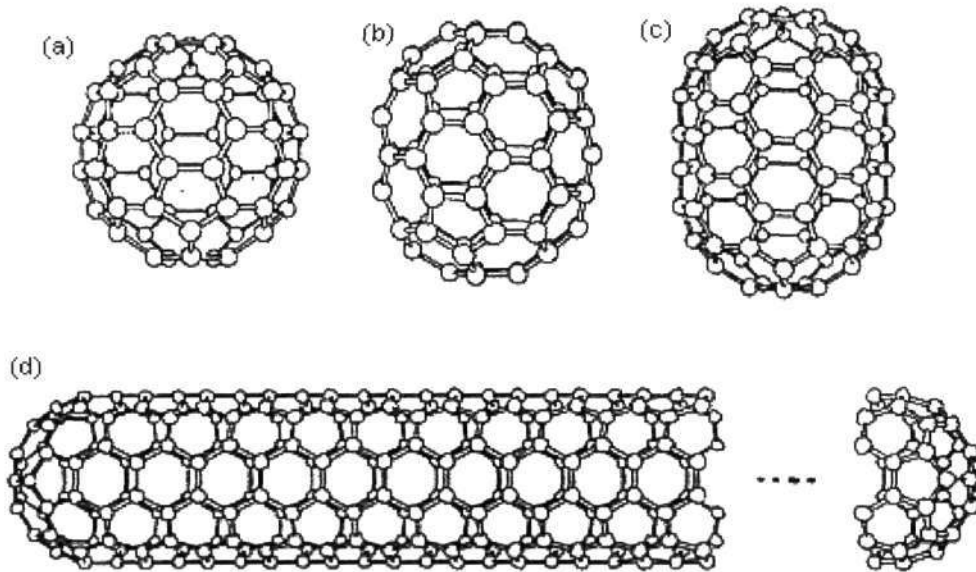


Figure 1.3: Models of (a) C_{60} , (b) C_{70} , an isomer of C_{80} and (d) a nanotube.

cathode. Large quantities of SWNTs can be obtained by using a mixture of 1 at.% of Y and 4.2 at.% of Ni [10]. SWNTs have also been synthesized by the condensation of a laser-vaporized carbon-nickel-cobalt mixture at 1200°C [11]. The decomposition of hydrocarbons over small metal catalyst has been the focus area of research in the synthesis of carbon nanotubes due to their scalability and ease of synthesis [12–14]. Nanotubes have also been prepared under electrochemical [15] and hydrothermal conditions [16]. MWNTs have been obtained by the decomposition of acetylene under inert conditions over Fe or Co/graphite [17, 18] and Fe/SiO₂ [19]. The presence of transition metal catalyst is essential for the formation of nanotubes and the diameter of the nanotube is determined by the size of the metal particles [20]. Aligned MWNT bundles have been obtained by chemical vapor deposition over transition metal catalyst embedded in the pores of mesoporous silica or the channels of alumina membranes [21, 22]. Plasma-enhanced chemical vapor deposition on nickel-coated glass using acetylene and ammonia has been employed by Ren *et al.* [23] to obtain aligned MWNT bundles. The

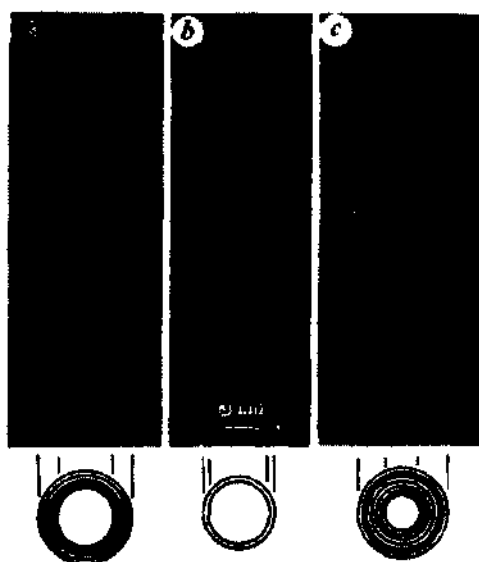


Figure 1.4: Models of (a) C_{60} , (b) C_{70} , an isomer of C_{80} and (d) a nanotube.

mechanism of growth of nanotubes by this method and the exact nature of the metal particles are not clear, although a nucleation process involving the metal particles is considered important. Pyrolysis of metallocenes such as ferrocene and other organometallic compounds like nickel and iron phthalocyanine in a two stage furnace provides a straight forward procedure to prepare carbon nanotubes [24–33]. The parameters that can be varied in these pyrolysis reactions are heating rate of the catalyst precursor, flow rate of the carrier gas and the pyrolysis temperature. These methods have yielded MWNTs [24–26], aligned MWNT bundles [27,28], aligned metal-filled MWNTs [29], Y-junction MWNTs [30,31] as well as single-walled carbon nanotubes (SWNTs) [32,33] under various experimental conditions. Aligned MWNT bundles have been obtained when a large heating rate of catalyst precursor was used and SWNTs under dilute catalyst and hydrocarbon conditions. Dai *et al.* [34] have prepared SWNTs by the disproportionation of CO at 1200°C over Mo particles of few nanometer dispersed in a fumed alumina matrix. Flahaut *et al.* [35] have synthesized SWNTs by passing a H_2 - CH_4 mixture over transition metal containing oxide spinels, obtained by

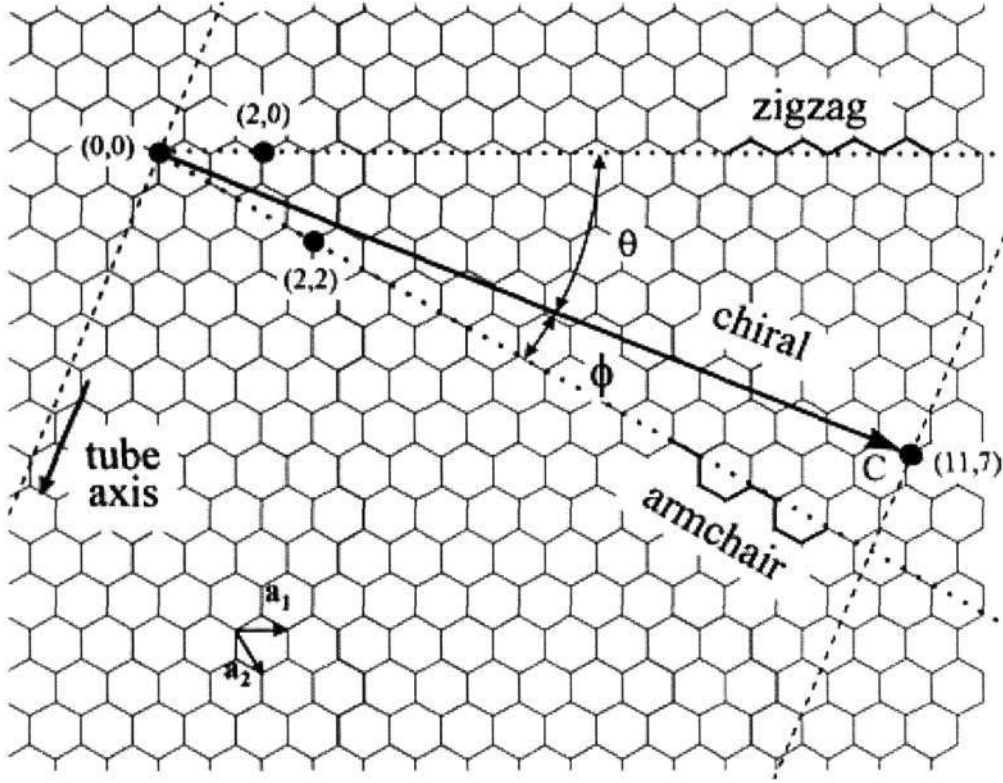


Figure 1.5: Rolling up of graphite to obtain a nanotube

the combustion route. Y-junction nanotubes can be obtained when an addition carbon source containing sulphur is incorporated. The advantage of the precursor method is that the aligned bundles are produced in one step, at a relatively low cost, without prior preparation of substrates.

A SWNT can be visualized by cutting C_{60} structure across the middle and adding a cylinder of graphite of the same diameter. If the C_{60} is bisected normal to a five-fold axis, an armchair tube is obtained and if it is bisected normal to a three fold axis, a zigzag tube is formed. In addition, a variety of chiral tubes can be obtained with the screw axis along the axis of the tube (armchair and zigzag nanotubes are achiral). Nanotubes can be defined by a chiral angle θ and a chiral vector C given by equation (1.1) where a_1 and a_2 are unit vectors in a 2D graphene lattice, while n and m are integers.

$$C = n a_1 + m a_2 \quad (1.1)$$

The vector C connects two crystallographically equivalent sites on a 2D graphene sheet while the chiral angle is the angle it makes with respect to the zigzag direction (Figure 1.5). A tube is formed by rolling up the graphite sheet such that the two points connected by the chiral vector coincide. The nanotube can be specified by the pair of integers (n,m) , which have a wide range of values. For the armchair nanotubes, $n = m \neq 0$ while $n \neq 0, m = 0$ for the zigzag nanotubes. For a nanotube defined by the index (n, m) , the diameter, d , and chiral angle, θ , are given by the equations 1.2 and 1.3, where $a = 1.42 \text{ \AA}$ and $0 \leq \theta \leq 30^\circ$.

$$d = a \cdot (m^2 + m \cdot n + n^2)^{1/2} / \pi \quad (1.2)$$

$$\theta = \arctan(-\sqrt{3} \cdot m / (2n + m)) \quad (1.3)$$

The MWNTs consist of capped concentric cylinders separated by 3.45 \AA , which is close to the separation between the (002) planes in graphite. The carbon nanotubes are capped by dome-shaped hemispherical fullerene-type units. The capping unit consists of pentagons and hexagons. SWNTs have defects like bends, which are due the presence of pentagons and heptagons on opposite sides of the tube [36].

Raman spectroscopy, electron microscopy and diffraction techniques have been widely used for the characterization of carbon nanotubes. Electron diffraction studies establish the presence of helicity [37]. The XRD pattern of MWNTs show only the $(hk0)$ and $(00l)$ reflections but no (hkl) reflections [38]. Raman spectroscopy provides important insights into the structure of nanotubes. Raman active phonon modes have been calculated by Jishi *et al.* [39] using a zone-folding model. The frequency of the allowed modes depend on the diameter and chiral angle of the tube. Diameter selective resonance behavior of SWNTs were observed by Rao *et al.* [40]. Resonant

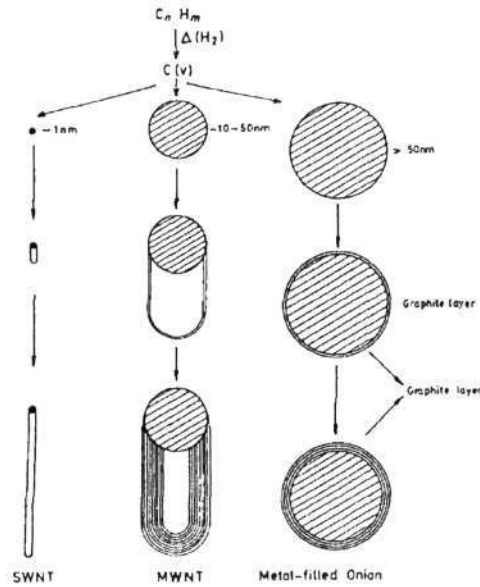


Figure 1.6: Schematic representation of the dependence of carbon nanostructure obtained by hydrocarbon pyrolysis on the diameter of the catalyst particle [12].

Raman spectroscopy on isolated single nanotubes has been used to determine (n, m) [41].

Several growth models have been proposed for carbon nanotubes growth by the arc discharge process as well as by the pyrolysis route. Endo and Kroto [42], based on the observation of C_2 ejection from the C_{60} in the mass spectrometry, suggest that tube formation process is a consequence of the formation of fullerenes. Isotope scrambling experiments show that under the conditions of formation, the plasma has vaporized atoms of carbon. Given the right conditions the tip opens and the nanotube grows [43]. Iijima *et al.* [44] have presented evidences based on electron microscopy for the open-ended growth of carbon nanotubes. Baker and Harris [45] have suggested a four step process for the growth of nanotubes by the pyrolysis route. The hydrocarbon decomposes on the metal surface to release hydrogen and carbon, which dissolves in the metal in the first step. The second step involves the diffusion of carbon through the metal particle and its precipitation on the rear face to

form the body of the filament. The supply of carbon onto the front face is faster than the diffusion through the bulk, causing accumulation of carbon on the front face, which would lead to the physical blocking of the active surface. Surface diffusion of carbon prevents this problem. In the last step, over-coating and deactivation of the catalyst particle leads to the termination of the growth. Oberlin *et al.* [46] have proposed a mechanism where bulk diffusion is insignificant and the carbon is transported by surface diffusion. A mechanism based on the formation of a hemispherical graphene cap on the catalyst particle has been proposed by Dai *et al.* [34]. Here the nanotubes grow from such a yarmulke and the diameter of the nanotube is controlled by the size of the catalyst particle with nanometer-sized yielding SWNTs. A salient feature of this model is the absence of the possibility of dangling bond creation at all stages of growth. SWNTs produced by the arc-discharge and laser ablation process may also be formed by this yarmulke process.

Carbon nanotubes exhibit a wide range of interesting properties [12]. Graphite is a semi-metal with valence and conduction bands degenerate at only six corners (K_B) of the hexagonal first Brillouin zone. In SWNTs, the wavevector k is quantized along the circumferential direction due to periodic boundary condition. Therefore, only a particular set of states, which are parallel to the corresponding tube axis are allowed (Figure 1.7) and a SWNT can be metallic or semiconducting depending on the diameter and chirality [47-49]. SWNTs are metals when $(n - m) / 3$ is an integer, and otherwise they are semiconductors. Low-temperature scanning tunnelling microscopy (STM) and scanning tunnelling spectroscopy (STS) studies of SWNTs reveal the atomically resolved images of the graphene cylinders (Figure 1.8) and their size-specific transport properties in agreement with theoretical predictions [50, 51]. Due to their nearly one-dimensional electronic structure, electron transport in metallic SWNTs and MWNTs occurs ballistically over

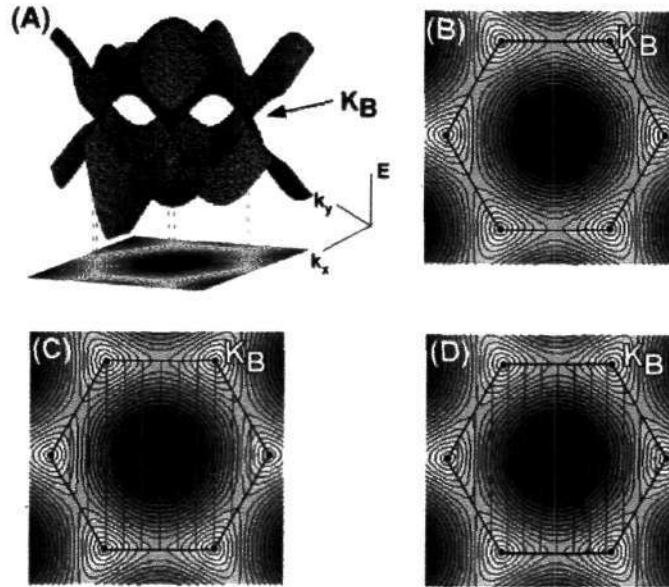


Figure 1.7: (A) Three dimensional plot of the π and π^* graphene energy bands and (B) a 2D projection. (C) and (D) Allowed wavevectors for a metallic (9,0) SWNT and semiconducting (10,0) SWNT respectively. The black hexagons define the first Brillouin zone of the graphene sheet, and the black dots in the corners are the K_B points. Blue lines represent allowed wavevectors, k , within the first Brillouin zone [51].

long nanotube lengths, enabling them to carry high currents with essentially no heating [52]. Carbon nanotubes also behave as field effect transistors (FETs) and have potential application in nanoelectronics [53,54]. Complex three-point nanotube junctions have been proposed as the building blocks of nanoelectronics by Menon and Srivastava [55]. The Y- and T-type junctions appear to defy the conventional models in favor of an equal number of five- and seven-membered rings to create nanotube junctions. It has been suggested that Y-junctions can be created with an equal number of five- and eight membered rings [55]. Y-junction MWNTs obtained by the pyrolysis route show asymmetry in the I-V curve around zero bias found at the Y junction [30] and have potential application in nano-circuits based on carbon nanotubes. SWNTs exhibit large thermoelectric power at high temperatures. The large thermoelectric power indicates the breaking of electron-hole

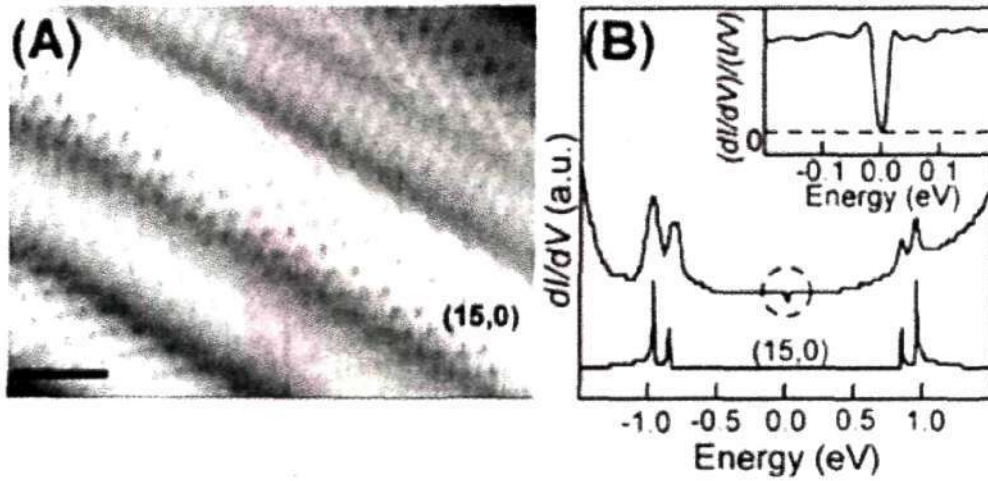


Figure 1.8: (A) Atomically resolved STM image of a (15,0) SWNT and (B) Tunnelling conductance, dI/dV , for (15,0) zigzag SWNT, with corresponding calculated DOS shown below. The inset shows curvature induced energy gap [51].

symmetry due to the self-assembly of nanotubes into crystalline lattices [56]. Phonons also propagate easily along the nanotube. The measured room temperature thermal conductivity for an individual MWNT ($> 3000 \text{ W/mK}$) is greater than that of natural diamond and the basal plane of graphite (both 2000 W/mK) [57].

Graphite, carbonaceous materials and carbon fibre electrodes are commonly used in fuel cells, batteries and other electrochemical applications. There have been several investigations for the use of carbon nanotubes for energy storage. The small dimensions, smooth topology and perfect surface specificity make carbon nanotubes suitable for energy storage. The high electrochemically accessible surface area of porous nanotube arrays, combined with their high electronic conductivity and useful mechanical properties, makes them attractive as electrodes for devices employing electrochemical double-layer charge injection. Examples include supercapacitors with giant capacitances in comparison with those of ordinary dielectric-based capacitors [58, 59], and electromechanical actuators that may be useful in



Figure 1.9: Emitting image of a fully sealed 4.5" SWNT-FE display (developed by Samsung Corp. [64]).

robots [60]. Hydrogen and Lithium have been electrochemically stored in carbon nanotubes. Early reports that carbon nanotubes can store considerable amounts of hydrogen created high expectations [61]. Gundiah *et al.* [62] have systematically measured H_2 adsorption on well-characterized samples of SWNTs, MWNTs, aligned multi-walled nanotube bundles as well as carbon fibres. The hydrogen storage does not exceed 3.7 wt % and carbon nanotubes fall short of expectations for use in automotive industry.

Field emission properties of carbon nanotubes have direct application in vacuum microelectronic devices. Carbon nanotubes are ideal as field emission (FE) sources due to their small diameter, high chemical stability, high mechanical strength and low carbon mobility [63]. Carbon nanotube based FE devices such as displays, x-ray generators, gas discharge tube protectors and microwave amplifiers have been made. Shown in Figure 1.9 is a 4.5" colour field emission display based on SWNTs cold cathodes fabricated at Samsung [64]. Carbon nanotubes based FE devices can be operated at room temperature which eliminates heating of cathode as in conventional FE

sources. The possibility of miniaturization of devices, high current density, narrow energy distribution and quick start could lead to the commercialization of CNT based FE devices. Carbon nanotubes, produced by ferrocene pyrolysis deposited on a tungsten tip exhibits high emission current densities with good performance characteristics [65]. The optical limiting properties of the carbon nanotubes are considered important for applications involving high power lasers. The optical limiting behavior of visible nanosecond laser pulses in the SWNT suspensions occurs mainly due to nonlinear scattering [66]. Gas and glucose sensors based on carbon nanotubes have been developed [67].

1.2 Nanowires

One-dimensional nanostructures such as wires, belts, rods and tubes of important inorganic materials have been synthesized in the last few years [3,68]. Nanowires are expected to play an important role as both interconnects and functional units in fabricating electronic, optoelectronic, electrochemical and electromechanical devices. One dimensional nanowires can be prepared by a variety of physical methods which include lithography techniques such as electron-beam (e-beam) or focused ion beam (FIB) writing, proximal probe patterning and extreme UV or x-ray photolithography. Several chemical methods have been developed for the synthesis of nanowires. An important aspect of the 1D structures relates to their crystallization, wherein the evolution of a solid from a vapour, a liquid, or a solid phase involves nucleation and growth. As the concentration of the building blocks (atoms, ions or molecules) of a solid becomes sufficiently high, they aggregate into small nuclei (clusters) through homogeneous nucleation [68,69]. These clusters serve as seeds for the further growth to form larger clusters. The main synthetic strategies employed for the synthesis of nanowires are:

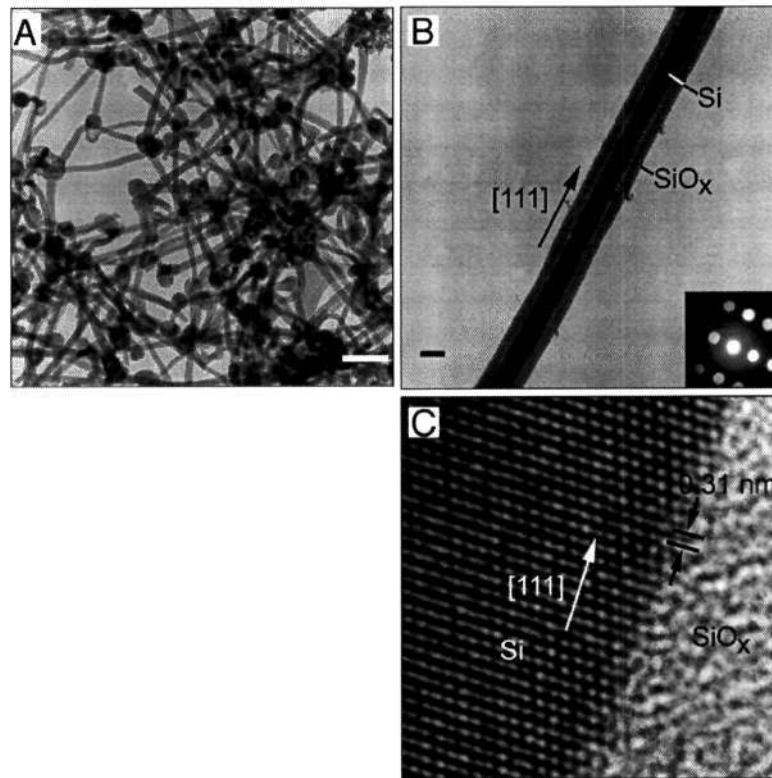


Figure 1.10: Silicon nanowires obtained by the VLS method [74].

- ◇ Growth from vapor phase involving either the vapour-solid (VS) or the vapour-liquid-solid (VLS) mechanism. Several classes of nanowires have been prepared employing this approach.
- ◇ Use of intrinsically anisotropic crystallographic structure of a solid to obtain 1-D nanostructures. Se [70, 71], Te [72] as well as molybdenum chalcogenides [73] have been prepared.
- ◇ Use of various templates which include porous membranes such as anodic alumina (AAO) membranes and track-etched polymer membranes. Existing one-dimensional structures such carbon nanotubes and nanowires have been used as templates for the synthesis of nanowires as well as nanotubes.
- ◇ Use of supersaturation to control and modify the growth habitat of

the seed.

- ◊ Appropriate capping agents have been used to kinetically control the growth rates at various facets of the seed.
- ◊ Self assembly of zero-dimensional nanostructures.

In 1960s, Wigner [69] proposed the VLS mechanism for the growth of large single-crystalline silicon whiskers. According to the mechanism, the anisotropic growth is promoted by the presence of the liquid alloy/solid interface. Nanowires of Si, Ge and binary semiconductors such as GaAs, ZnO etc. have been prepared using this route (Figure 1.10). Laser ablation of appropriate targets [74, 75] and thermal evaporation [76] of appropriate precursor has been used for the synthesis of nanowires by this method. Until recently, the only evidence for the growth of nanowires by the VLS mechanism is the presence of droplets at the end of the nanowires. Wu *et al.* [77] have reported real-time observation of Ge nanowire growth in an *in-situ* high-temperature TEM, which demonstrates the validity of the VLS mechanism (Figure 1.11). The experimental observations suggest that there are three stages in the growth: metal alloying, crystal nucleation and axial growth. Lee and coworkers [78] have proposed an oxide assisted growth mechanism for the growth of Si nanowires in the absence of catalyst. In the presence of SiO₂, the yield of the Si nanowires increases. Si_xO ($x > 1$) vapours are generated by the thermal evaporation or laser ablation which decomposes to give Si nanowires. One dimensional nanostructures can be obtained by the VS process if one can control the nucleation and growth process. Nanowires of several oxide like ZnO, SnO₂, etc. have synthesized by the process. Carbothermal route is a simple route for the synthesis of several classes of nanowires. The process involves the heating a mixture of the precursor (generally oxide) with carbon (activated carbon or carbon nanotubes) in a suitable atmosphere [79]. The first step normally involves the formation of a volatile metal suboxide by the

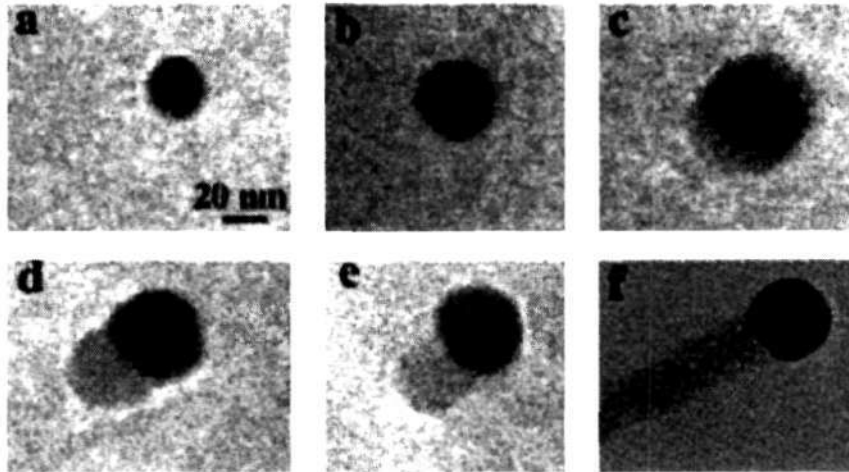


Figure 1.11: In-situ TEM images recorded during the process of nanowire growth. (a) Au nanoclusters in solid state at 500 °C; (b) alloying initiated at 800 °C, at this stage Au exists mostly in solid state; (c) liquid Au/Ge alloy; (d) the nucleation of Ge nanocrystal on the alloy surface; (e) Ge nanocrystal elongates with further Ge condensation and eventually forms a wire (f) [77].

reaction with carbon. Oxide, nitride or carbide nanowires are obtained when the suboxide is heated in the presence of O_2 , NH_3 , N_2 or C. Solution based approaches utilize the anisotropic growth dictated by the crystallographic structure of the solid material, or confined and directed by templates, or kinetically controlled by supersaturation, or by the use of appropriate capping agent. Buhro and coworkers [80] have developed a low-temperature solution-liquid-solid (SLS) method for the synthesis of crystalline nanowires of III-V semiconductors. A metal with a low melting point is used a catalyst and the desired material material generated through the decomposition of organometallic precursor. Korgel *et al.* [81] have extended this strategy for the synthesis of Si and Ge nanowires in supercritical fluids.

Due to their high surface area, the nanowires exhibit significantly lower melting point which is inversely proportional to the diameter of the nanowire [82]. Single crystalline 1D nanostructures are supposed to have significantly superior mechanical properties than their counterparts that have larger dimensions. SiC nanorods pinned at one end of the solid surface have a

Young's modulus of 610-660 GPa in good agreement with theoretical predictions [83]. Nanowires have recently been explored as building blocks to fabricate nanoscale electronic devices through self-assembly. Nanowire based field-effect transistors (FETs), p-n junctions, bipolar junction transistors, complementary inverters and resonant tunnelling diodes have been fabricated [84]. Dresselhaus and coworkers [85] have observed a semi-metal to semiconductor transition in Bi nanowire arrays when the diameter is 52 nm. Nanowires with very short lengths (usually few atoms across) also exhibit ballistic transport (conductance quantization in units of $2e^2h^{-1}$). Self-assembly of nanowires has been used by Huang *et al.* [86] for the fabrication of OR, AND, and NOR logic-gate structures.

As the dimension of the nanowire is reduced the range of phonon mean free path, the thermal conductivity is reduced due to the scattering by the boundaries. The reduced thermal conductivity is desirable for applications such as thermoelectric cooling and power generation. The thermoelectric figure of merit (Z) could be substantially enhanced for thin nanowires by carefully controlling their diameter, composition and carrier concentrations [87]. In contrast to quantum dots, the light emitted from nanowires is highly polarized along their longitudinal axes and polarization sensitive nanoscale photodetectors have been fabricated [88]. Surface plasmon properties of gold and silver nanorods have been investigated by El-Sayed and coworkers [89]. One dimensional nanostructures exhibit two surface plasmon corresponding to the transverse and longitudinal plasmon resonances. The longitudinal resonance energy is inversely proportional to the nanowire length. Room temperature UV-lasing from ZnO nanowire arrays have been observed [90]. Light induced insulator to conductor transition has been observed in ZnO nanowires by Kind *et al.* [91], which could be used as UV detectors and photo-switches.

Chapter 2

CARBON NANOTUBES BY NEBULIZED SPRAY PYROLYSIS

2.1 Introduction

Carbon nanotubes have been produced by a variety of techniques (see chapter 1 for more details) and pyrolysis of metallocenes such as ferrocene in a two stage furnace is a simple route for the synthesis of various types of carbon nanotubes [13]. Glerup *et al.* have modified this two stage furnace method and have used aerosol method for carrying the catalyst and carbon source for the synthesis of MWNTs and nitrogen doped MWNTs [92]. Ajayan and co-workers have synthesized long strands of SWNTs by the pyrolysis of a spray containing ferrocene, thiophene and n-hexane [93]. We have systematically examined the utility of nebulized spray pyrolysis for the synthesis of carbon nanotubes. Nebulized spray pyrolysis has been employed earlier for the preparation of sub-micron sized particles [94] and epitaxial thin films [95,96] of complex metal oxides. The advantage of using nebulized spray is the large number of parameters that can be utilized to control the pyrolysis reaction and it can be easily scaled into an industrial scale process, as the reactants are fed into the furnace continuously. We have been able to control the diameter distribution and quality of the nanotubes by adjusting the various available parameters like pyrolysis temperature, carrier gas flow rate, catalyst precursor concentration, various hydrocarbon sources and various catalyst precursors. We have characterized the nanotubes obtained by various experiments by electron microscopy and X-ray diffraction

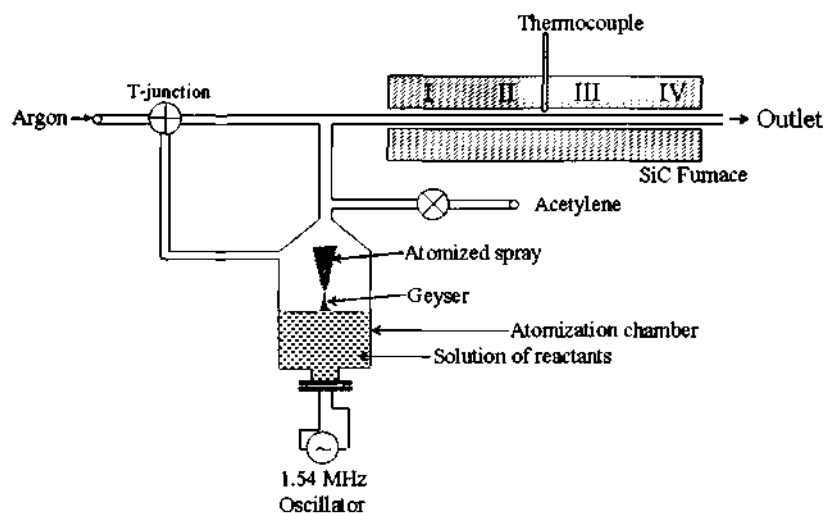


Figure 2.1: Schematic representation of the experimental set-up.

2.2 Nebulized Spray Pyrolysis

Nebulized spray is a spray generated by an ultrasonic atomizer [97]. When a high frequency (100 kHz-10 MHz range) ultrasonic beam is directed to a gas-liquid interface, a geyser forms at the surface. The height of the geyser is proportional to the acoustic intensity. The formation of the geyser is accompanied by the generation of a spray, resulting from the vibrations at the liquid surface and cavitation at the gas-liquid interface. The quantity of the spray produced is also a function of the acoustic intensity and of certain physical properties of the liquid (vapour pressure, viscosity and surface tension). In Figure 2.1, we show the schematic diagram of the experimental set-up. A piezoelectric transducer (made of PZT) is at the base of the atomization chamber. The transducer is connected to a high frequency voltage generator. The frequency of the voltage generator is fixed at a value close the resonance frequency of the transducer. By varying the voltage the acoustic intensity can be varied. During the atomization process, the liquid is heated close to 100 °C, hence, some of the atomized liquid may change into the vapour state which is detrimental to the spray homogeneity. To avoid this problem, the

nozzle carrying the mist from the atomization chamber should be narrow and long. A very narrow and long nozzle leads to collisions of droplets and there is change in the size distribution of the droplets. The relationship between the capillary wavelength (C) at the liquid surface and mean diameter of the atomized droplets (D) is given as below:

$$D = a \cdot C \quad (2.1)$$

where a is constant. From the Kelvin's equation, the capillary wavelength can be written as a function of surface tension of the liquid (s), density (r) and ultrasonic excitation frequency (f):

$$C = (8 \cdot \pi \cdot s / r \cdot f^2)^{1/3} \quad (2.2)$$

a has been experimentally determined to be 0.34. Therefore,

$$D = 0.34(8 \cdot \pi \cdot s / r \cdot f^2)^{1/3} \cong (ps / r f^2)^{1/3} \quad (2.3)$$

The frequency dependence of the D leads to a very narrow distribution in the droplet size. It has been shown that, at constant ultrasonic power level and gas flow rate, the amount of material transported (r):

$$r = ps / s \cdot h \quad (2.4)$$

where ps is the saturated vapour pressure of the liquid, s its surface tension and h its dynamic viscosity. The variation of droplet size and distribution for water as a function of frequency is shown in Figure 2.2.

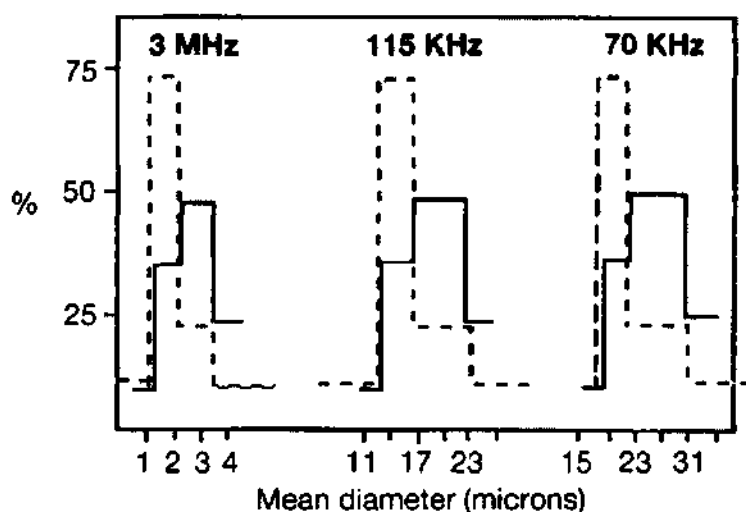


Figure 2.2: Variation of droplet size and distribution for water with frequency.

2.3 Experimental

The solution of the reactants was nebulized using a 1.54 MHz ultrasonic beam as shown in the Figure 2.1. In all the experiments, ultra high pure argon was used as the carrier gas and the gas flow rate was controlled using UNIT mass flow controllers. The average droplet size for the various solvents for 1.54 MHz frequency is approximately 2.2 microns. In all experiments, the atomized spray was carried into a 25 mm quartz tube that was placed in a SiC furnace which was held at a particular temperature (pyrolysis temperature). Ferrocene, nickelocene, cobaltocene and iron pentacarbonyl were used as both catalyst and carbon sources. Benzene, toluene, xylene, mesitylene and n-hexane were used as solvents for the catalyst and also act as carbon sources. We have also used acetylene as an additional carbon source in some of the pyrolysis experiments.

Silicon substrates were placed in the regions I, II, III and IV of the reactor to collect the product as shown in Figure 2.1. The quartz tube and the nebulization chamber are purged and oxygen is removed before the experiment. In a typical nebulized spray reaction, a solution of metallocene was

nebulized and passed into the furnace using 1000 sccm of argon for 30 min. After the reaction, the flow rate was reduced to 20 sccm and the furnace was allowed to cool. The products were collected after the tube cooled to room temperature. In the case of $\text{Fe}(\text{CO})_5$, it was nebulized for 5 minutes and the atomized droplets were carried into the furnace by a mixture of 100 sccm of acetylene and 1000 sccm of argon. The acetylene was stopped after 25 min. Pyrolysis of the atomized spray yielded MWNTs primarily in regions II and III while primarily carbon spheres were obtained in region IV in the case of ferrocene. We observed SWNTs in region IV when cobaltocene and nickelocene were used as catalyst precursors. We have changed the droplet size by increasing the ultrasonic excitation frequency to 2.6 MHz, the average droplet size decreases to 1.55 μm .

To compare the quality of the MWNTs produced by nebulized spray pyrolysis, we prepared arc-discharge MWNTs by striking an arc between two graphite electrodes in a helium atmosphere. The cathodic deposit was collected, powdered and sonicated in ethanol for 2 h to separate the turbostratic graphite from the MWNTs. The powder X-ray diffraction (XRD) patterns were recorded using a Seifert XRD 3000 TT instrument. The scanning electron microscope (SEM) images were obtained with a Leica S-440I microscope. Transmission electron microscope (TEM) images with a JEOL JEM 3010 instrument operating at an accelerating voltage of 300 kV.

2.4 Results and Discussion

Nebulized spray pyrolysis of a solution of ferrocene in toluene (20 g/l) gave a good yield of MWNTs in regions II and III as shown in Figure 2.3. The formation of the MWNTs was found to be sensitive to temperature. At lower temperatures, the yield of the MWNTs decreased and catalyst metal particles were obtained as seen in the SEM image in Figures 2.3(a) and (b).

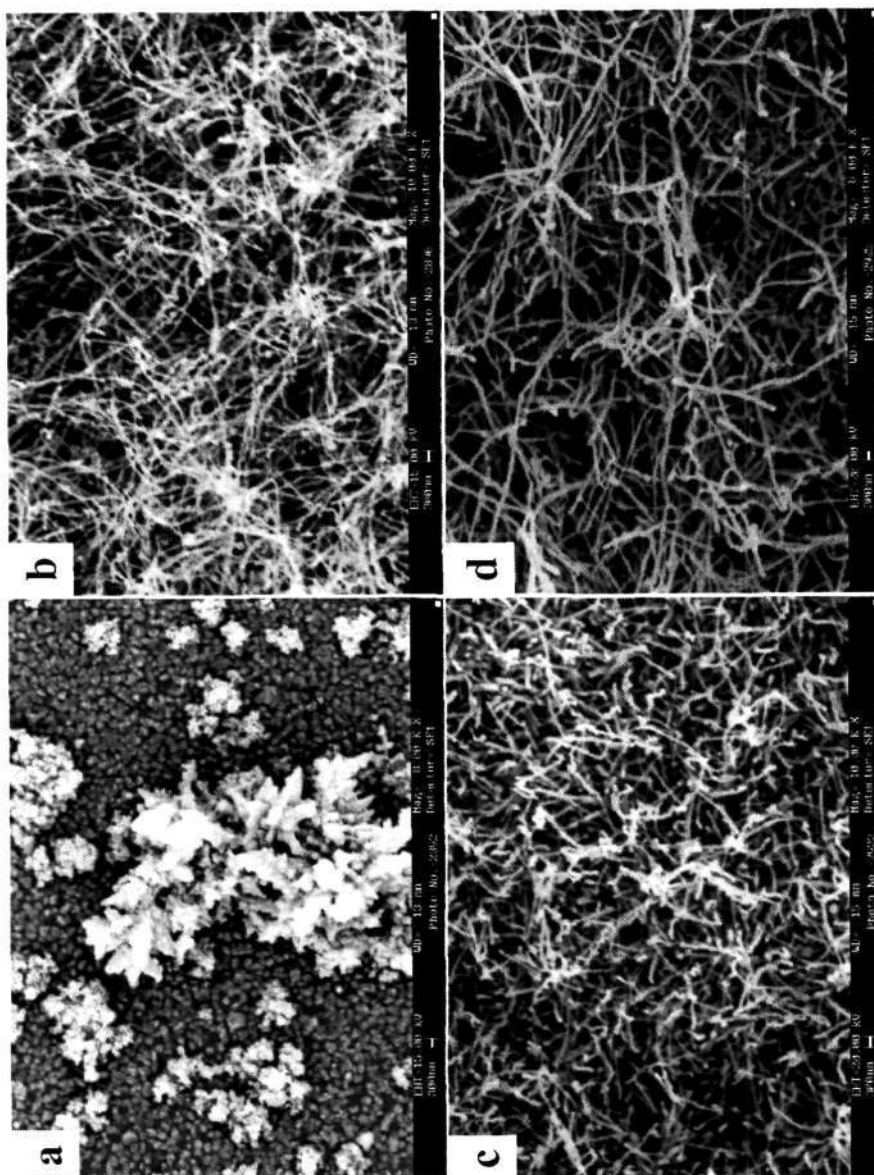


Figure 2.3: (a),(b)-SEM images of products obtained in region II and region III by pyrolysis of nebulized spray of 20 g/l solution of ferrocene in toluene at 840 °C. (c),(d) SEM images obtained by pyrolysis at 900 °C.

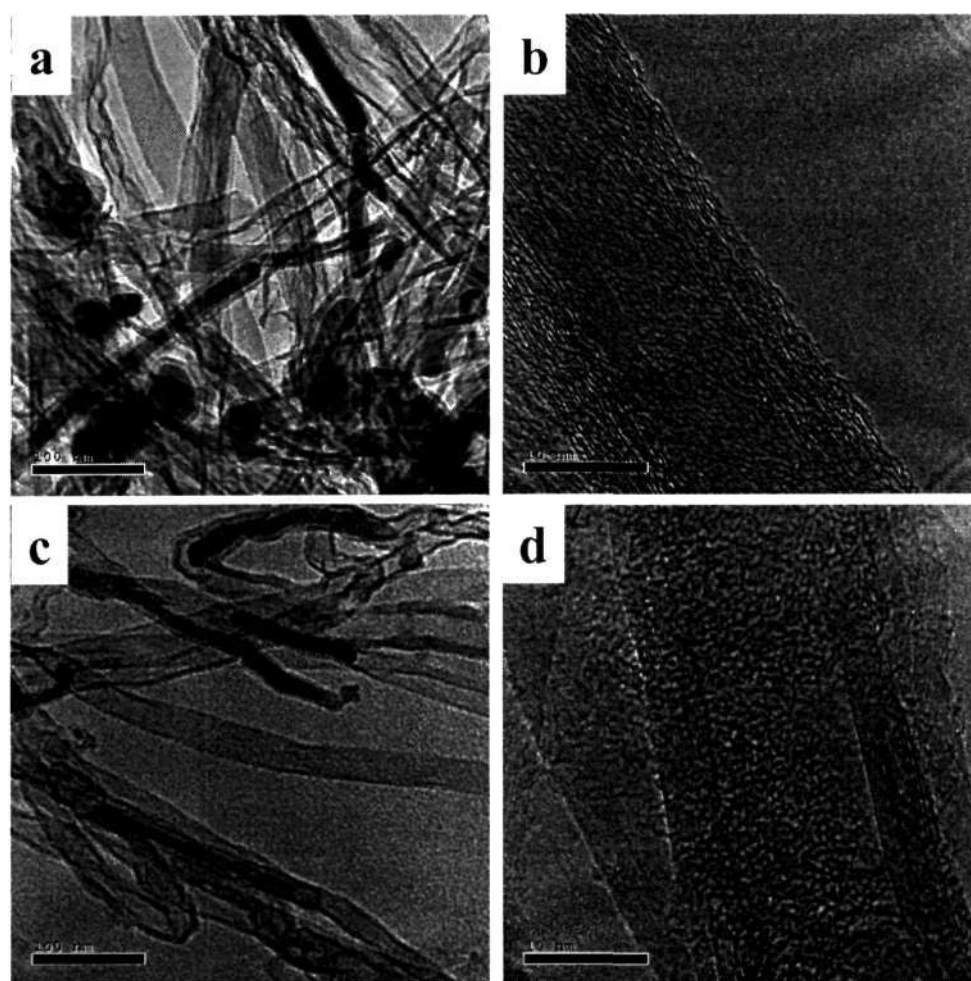


Figure 2.4: a,b-SEM images of products obtained in region II and region III by pyrolysis of nebulized spray of 20 g/l solution of ferrocene in toluene at 840 °C. c-d SEM images obtained by pyrolysis at 900 °C.

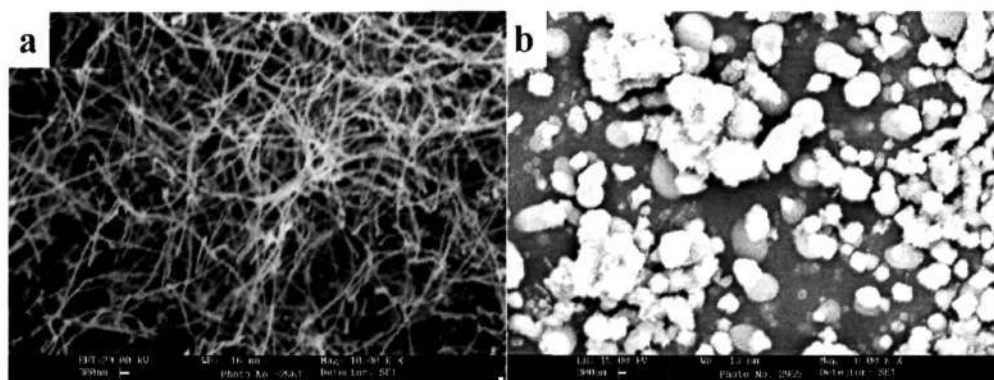


Figure 2.5: (a) SEM image of MWNTs obtained by the pyrolysis of a toluene solution of ferrocene (20 g/l) at 500 sccm of Argon flow at 900 °C and (b) SEM image of MWNTs obtained by the pyrolysis of the same solution at 2000 sccm Argon flow at 900 °C. (Region II)

The optimum temperature for the growth of MWNTs was found to be 900 °C with a large yield of MWNTs in both region II and III (See Figures 2.3 (c) and (d)). The nanotubes are approximately 40 nm in diameter and ten of microns long as revealed by the SEM images. At higher temperatures the yield of nanotubes decreased and was accompanied by the formation of shiny carbon films. The auto-pyrolysis of toluene and other solvents increases as the temperature increases and larger quantities of carbon spheres were obtained in region IV. In Figure 2.4, TEM images of MWNTs obtained by the nebulized spray pyrolysis of a solution of ferrocene in toluene (20 g/l) shows that many of the MWNTs are metal filled. The average diameter of MWNTs were estimated as 36 nm (diameter range of 36 ± 16 nm). From high-resolution electron microscopy (HREM), we found that the crystallinity of MWNTs increases with the increase in the pyrolysis temperature as seen in Figures 2.4(b) and (d).

The quantity of the reactants carried inside the furnace is directly proportional to the Ar flow rate. The flow rate of the carrier gas also affects the yield and quality of the MWNTs. At low flow rate of 200 sccm of argon, yield of MWNTs was negligible as little reactant was carried. Very short MWNTs

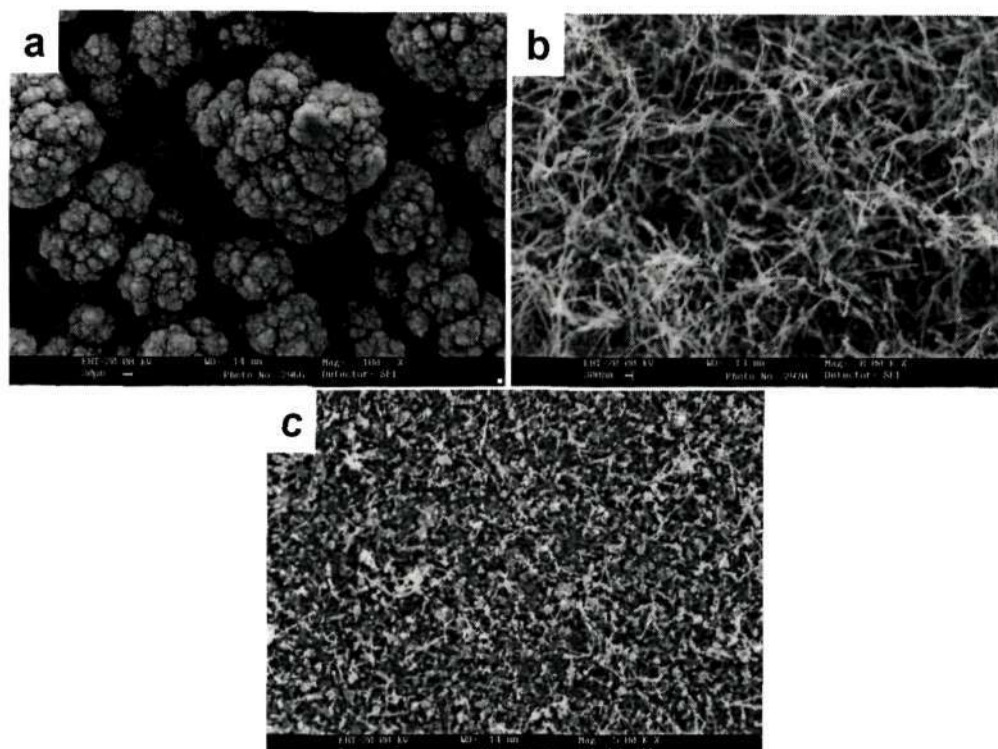


Figure 2.6: (a) and (b) SEM image of the MWNTs pyrolysis of toluene solution of ferrocene (80 g/l) at 900°C in region II and (c) SEM image of particles obtained in region III in the same reaction.

and large particles were obtained at a high flow rate of 2000 sccm of argon. A flow rate of 1000 sccm of argon was found to be ideal for the growth of MWNTs. In Figure 2.5(a), we show MWNTs obtained in region II when 500 sccm of argon was used and Figure 2.5(b) shows the large particles when the argon flow rate was 2000 sccm.

The concentration of ferrocene in toluene was found to be crucial in determining the yield of the MWNTs. Bulbs of MWNTs were obtained when the concentration of ferrocene was increased to 80 g/l (saturated solution) revealed by the SEM image in Figure 2.6(a). These bulbs indeed contain MWNTs as seen in Figure 2.5(b). As the concentration of ferrocene was increased the yield of MWNTs also increased. A concentration of 20 g/l was found out to be ideal as MWNTs were obtained in both regions II and III while at higher concentration catalyst particles were obtained in region III

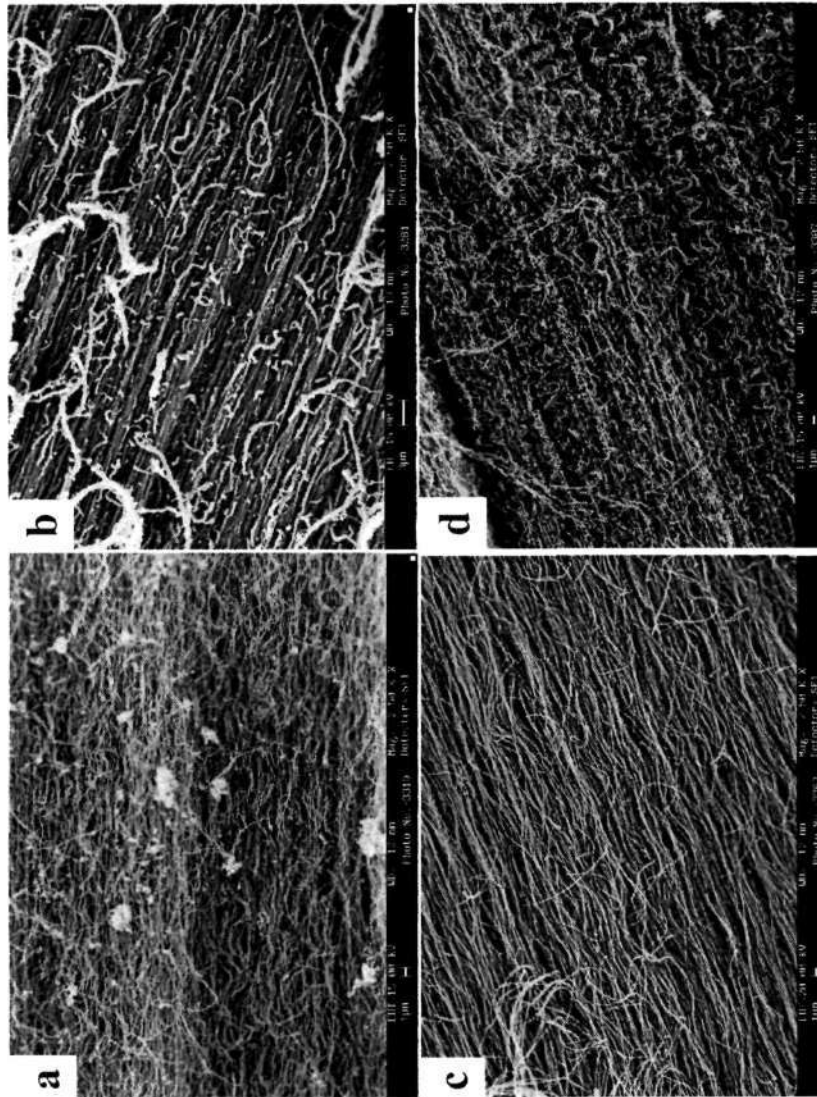


Figure 2.7: SEM images of MWNTs obtained by the pyrolysis of ferrocene in (a) benzene, (b) xylene, (c) mesitylene (d) n-hexane at 900 °C with an argon flow rate of 1000 sccm.



Figure 2.8: Photograph of aligned MWNT obtained by nebulized spray pyrolysis of toluene solution of ferrocene (80 g/l) at 900 °C with 100 sccm of acetylene as additional carbon source.

as seen in Figure 2.6(c). The average diameter of the MWNTs decreased to 23 nm and the distribution narrowed down to 23 ± 11 nm. In the absence of ferrocene only carbon spheres were obtained which is in agreement with our earlier observations in the laboratory [98]. Glerup et al. [92] observe that the diameter of the MWNTs to be proportional to the concentration of the catalyst. The concentration and droplet size in our experiments are different from their values. The larger droplet size and higher concentration indicates that there are multiple nucleation centers within the droplet. Even though there is multiple nucleation, the diameter distribution of MWNTs obtained from any particular region of the furnace was found to be narrow. Further, the bulbs of MWNTs are also an additional evidence for the formation of multiple nucleation within the droplet. We did not observe any significant changes when the droplet size was decreased to $1.55 \mu\text{m}$.

Aligned MWNT bundles were obtained when other hydrocarbon like benzene, xylene, mesitylene and n-hexane were used instead of toluene as seen

620.193
POH



in Figures 2.7. The choice of the solvent for the catalyst precursor is important to determine the nature of the final product as indicated by the above observation. The aligned MWNT bundles were with lengths greater than 100 micrometer and homogenous throughout the silicon substrate. The SEM images indicate aligned MWNTs without impurities such as nanoparticles and amorphous carbon can be obtained when mesitylene is used as a carbon source. The density of aligned MWNTs increases as we move from xylene to n-hexane with n-hexane solutions of ferrocene yielding the highest density of aligned MWNTs as seen in Figure 2.7. Large quantities of aligned MWNT can be obtained by our route as indicated by Figure 2.8. The diameter distribution plots for the MWNTs obtained with various carbon sources under similar reaction conditions is given in Figure 2.9. The nebulized spray pyrolysis of ferrocene in benzene yielded aligned MWNTs with an average diameter of 59 nm (diameter distribution: 59 ± 26 nm) as seen in Figure 2.9(a). Large quantities of graphite sheathed metal nanoparticles were also observed in addition to the MWNTs. In Figure 2.10(a), we show a typical TEM image of MWNTs and graphite sheathed metal nanoparticles when benzene was used a carbon source. Large and well-graphitized MWNTs were obtained when xylene and mesitylene (average diameters 100nm) were used as a carbon source as seen in Figures 2.10(b) and (c). Only aligned carbon nanotubes were observed when mesitylene and n-hexane were used as carbon sources. We consider n-hexane and mesitylene as ideal sources of carbon for the synthesis of aligned MWNTs as they yield copious quantities of MWNTs. The only disadvantage of using n-hexane is its relatively very high vapour pressure, which affects the quality of the atomized spray. Benzene, xylene, mesitylene and n-hexane appear to be better carbon sources when compared to toluene.

Aligned MWNT bundles can be obtained with toluene when acetylene

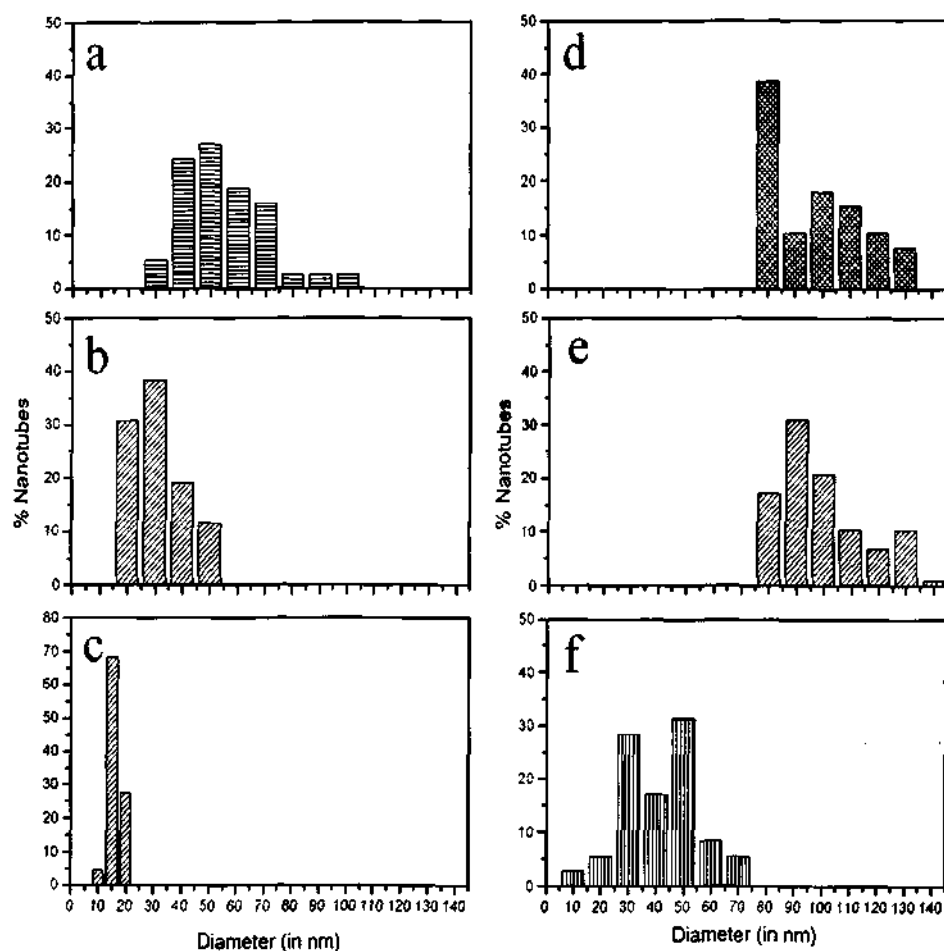


Figure 2.9: Diameter distribution plots of MWNTs obtained by the pyrolysis of ferrocene solution of (a) benzene, (b) toluene, (c) toluene with inclusion of 100 sccm of acetylene, (d) xylene (e) mesitylene and (f) n-hexane at 900 °C with an argon flow rate of 1000 sccm. The diameters were calculated from TEM micrographs.

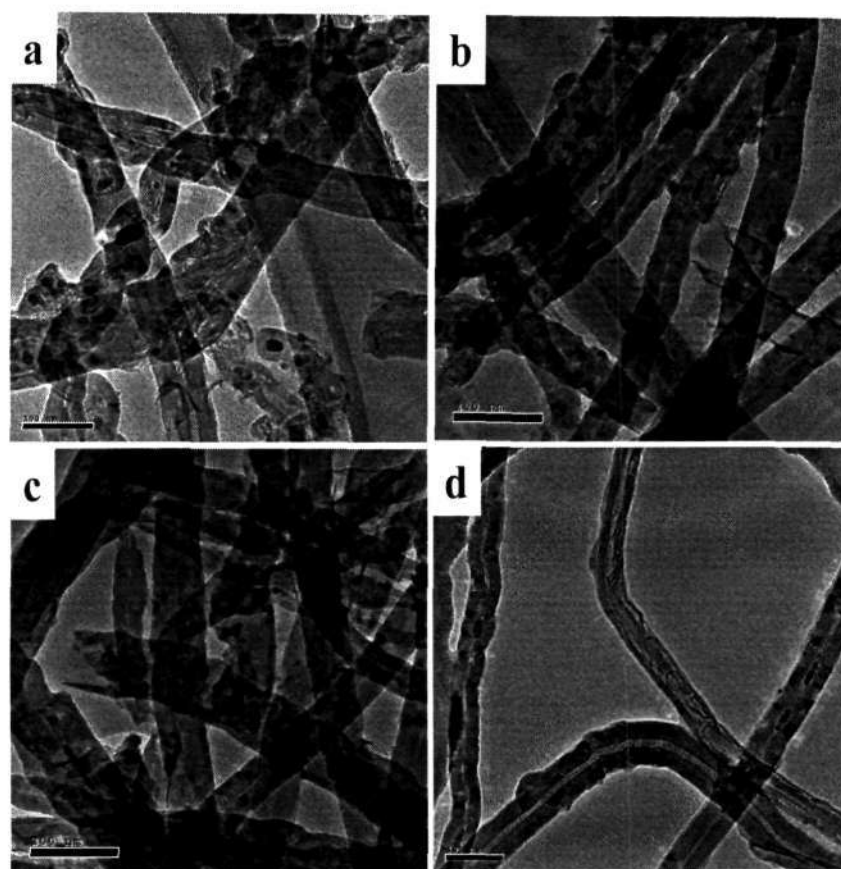


Figure 2.10: TEM images of MWNTs obtained by the pyrolysis of ferrocene in (a) benzene, (b) xylene, (c) mesitylene (d) n-hexane at 900 °C with an argon flow rate of 1000 sccm.

was added as additional carbon source. When 100 sccm of acetylene was included to the atomized spray of ferrocene in toluene, multi-layer aligned MWNT bundles were obtained as seen in Figure 2.11(a). A single layer of aligned MWNTs was obtained by reducing the nebulization time from 30 min to 5 min, while the acetylene flow was continued for the remaining 25 mins. The SEM image in Figure 2.11(b) shows 1 mm long MWNTs obtained by the method as described above. The density of aligned MWNTs depended on the flow rate of acetylene and concentration of ferrocene as seen Figures 2.11(c) and (d) respectively. By increasing the concentration of ferrocene, we were able to obtain highly dense aligned MWNT bundles with MWNTs of larger diameters. When the concentration of ferrocene was

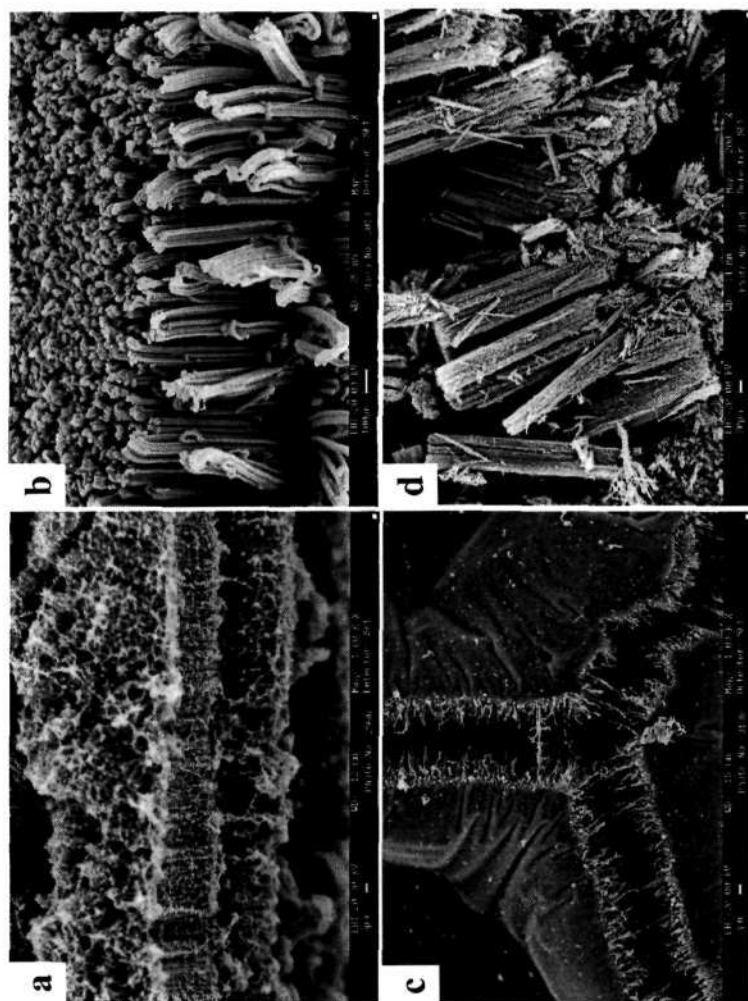


Figure 2.11: (a) SEM image of aligned MWNTs obtained by the pyrolysis of a solution of ferrocene in toluene (20 g/l) along with 100 sccm acetylene for 30m. (b) SEM image of aligned MWNTs obtained by the pyrolysis of toluene solution of ferrocene (20 g/l) for 5m and acetylene flow of 100 sccm for a duration of 30m. (c) SEM image of aligned MWNTs obtained at a lower flow rate of 50 sccm. (d) SEM image of highly dense aligned MWNTs obtained by the pyrolysis of higher concentration of ferrocene in toluene (80 g/l). The pyrolysis temperature in all the above is 900 °C

decreased to 10 g/l, MWNTs with no alignment were obtained indicating the presence of a critical concentration for the synthesis of aligned MWNT bundles by this approach. As the flow rate of acetylene was decreased to 50 sccm the density of the aligned MWNTs decreased (see Figure 2.11(c)). Figure 2.12 shows the TEM images of aligned MWNTs obtained by this approach. The diameter distribution of the MWNTs decreases drastically when the nebulization time is reduced to 5 min, here MWNTs with an average diameter of 18 nm (diameter distribution 18 ± 4.5 nm) were obtained in the region II as seen in Figure 2.9(c). The MWNTs obtained by the inclusion of acetylene are more graphitized than the MWNTs obtained under similar conditions in the absence of acetylene (see inset of Figure 2.12(b)), indicating acetylene is a good carbon source. Decreasing the pyrolysis temperature did not decrease the crystallinity of MWNTs as seen in the inset of Figure 2.12(c). The number of graphitic layer increased as the concentration of ferrocene was increased as seen in Figure 2.12(d) indicating the increase in the size of the catalyst particle.

We also carried out pyrolysis reactions with other metallocenes like cobaltocene and nickelocene. The solubility of cobaltocene in toluene was a limiting factor and the solubility was found out to be close to 10 g/l. In Figures 2.13(a)-(c), we show the TEM images of the nanotubes obtained by the nebulized spray pyrolysis of a saturated solution of cobaltocene in toluene. MWNTs with smaller diameters were obtained in region II (diameter ranging between 5-25 nm). We observed few isolated SWNTs in region IV along with a large amount of amorphous carbon covered metal nanoparticles. In Figure 2.13(d), we show a typical TEM image of MWNTs obtained by the nebulized spray pyrolysis of a 20.0 g/l solution of nickelocene in toluene.

We also used $\text{Fe}(\text{CO})_5$ as a metal source and it can be used without any addition of solvent. Nebulized spray pyrolysis of $\text{Fe}(\text{CO})_5$ alone yields bead

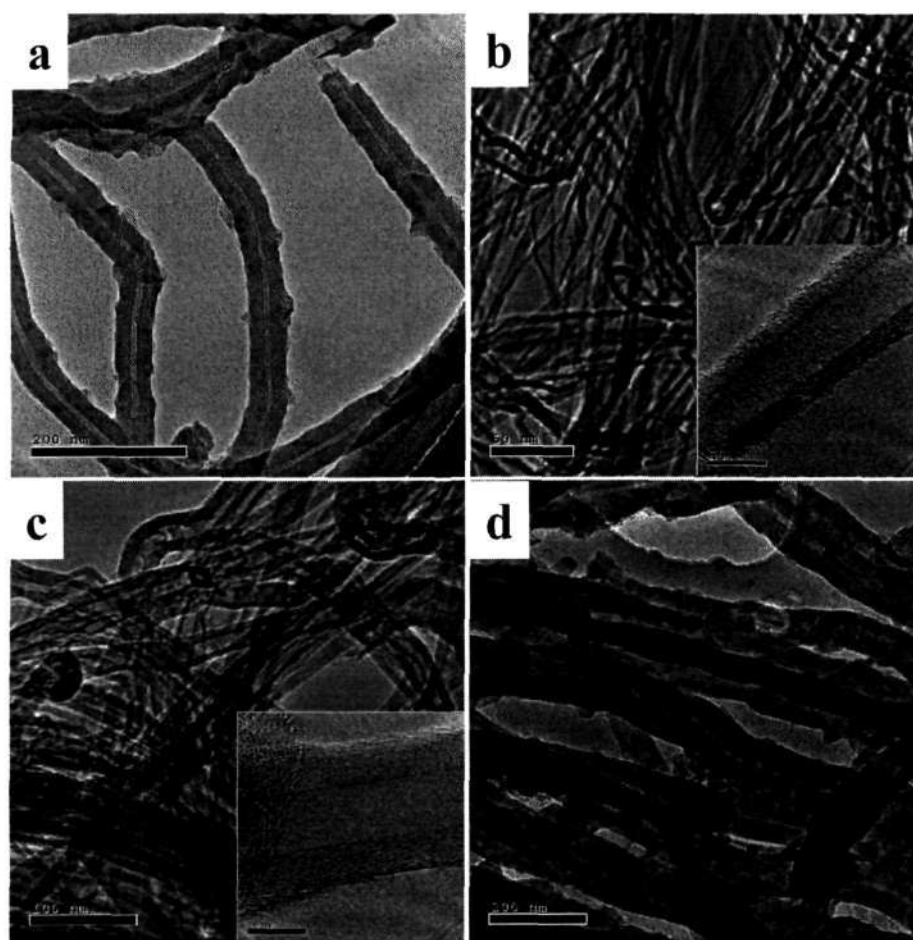


Figure 2.12: (a) TEM image of aligned MWNTs obtained by the pyrolysis of a solution of ferrocene in toluene (20 g/l) along with 100 sccm acetylene for 30m. (b) TEM image of aligned MWNTs obtained by the pyrolysis of toluene solution of ferrocene (20 g/l) for 5m and acetylene flow of 100 sccm for 30m., inset shows the HRTEM image for the same sample. (c) TEM image of aligned MWNTs obtained at a lower temperature of 840 °C. (d) TEM image of highly dense aligned MWNTs obtained by the pyrolysis of ferrocene solution (80 g/l).

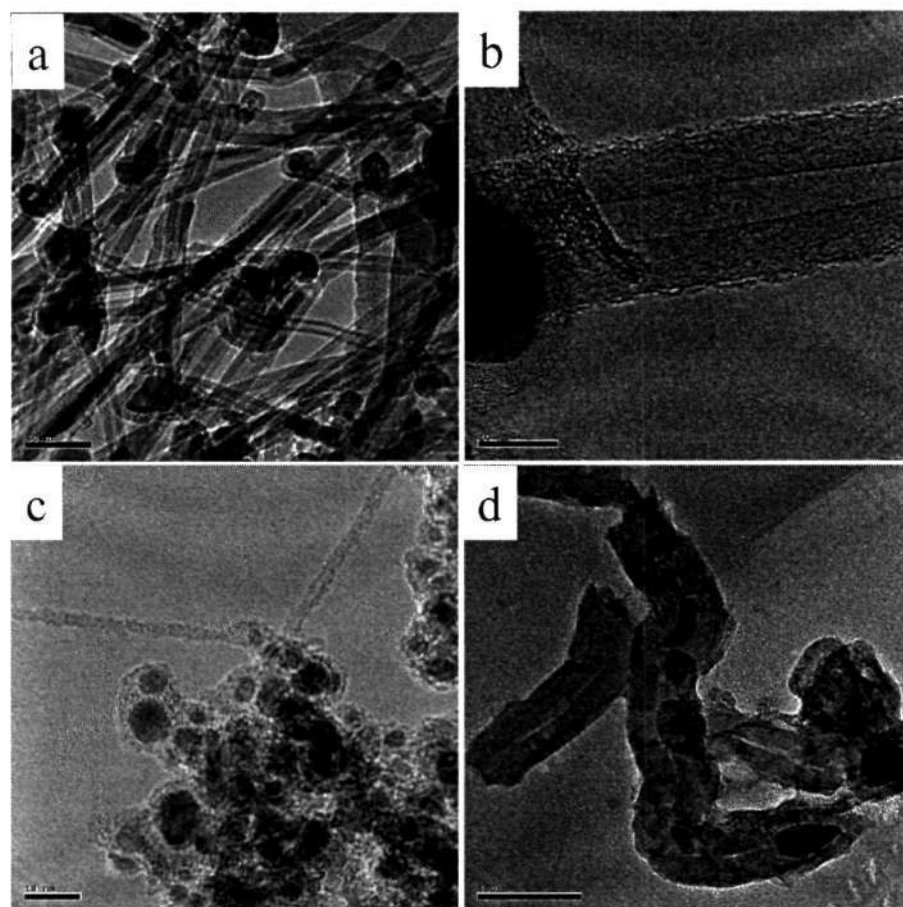


Figure 2.13: (a) TEM image of MWNTs obtained in Region II by the nebulized spray pyrolysis of cobaltocene in toluene (saturated), (b) HREM image of the same as in (a), (c) TEM image of SWNTs in Region IV by the nebulized spray pyrolysis of cobaltocene in toluene and (d) TEM image of MWNTs obtained by the nebulized spray pyrolysis of nickelocene in toluene (20.0 g/l)

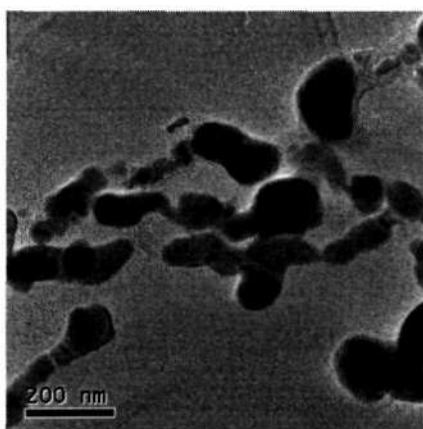


Figure 2.14: TEM image of bead-like nanostructures obtained by the nebulized spray pyrolysis of $\text{Fe}(\text{CO})_5$ at 900°C

like connected structures in regions I and IV of the furnace as seen in Figure 2.14. The addition of acetylene yields aligned MWNTs in regions II and III while carbon coated metal particles (5-15 nm in diameter) were obtained in region IV. In Figure 2.15(a), we show a typical SEM image of aligned MWNTs obtained by the pyrolysis of a nebulized spray of $\text{Fe}(\text{CO})_5$ at 900°C with a flow 100 sccm of acetylene and 1000 sccm of argon. The TEM image in Figure 2.15(b), shows that the aligned MWNTs have an average diameter of 33 nm. The MWNTs obtained by this route are well graphitized as seen in Figure 2.15(c). The only disadvantage in using $\text{Fe}(\text{CO})_5$ is the corrosion of the atomizer electrode as $\text{Fe}(\text{CO})_5$ is very reactive.

MWNTs exhibit squared Lorentzian (001) and saw-tooth (hk0) in their X-ray diffraction pattern [38]. We have used X-ray diffraction to obtain the crystallinity of the nanotubes. In Figure 2.16, we compare the powder X-ray diffraction patterns of the MWNTs obtained by the various routes to that of the arc discharge MWNTs. It seems that xylene is the best hydrocarbon source for the synthesis of well graphitized MWNTs by nebulized spray pyrolysis from X-ray diffraction results.

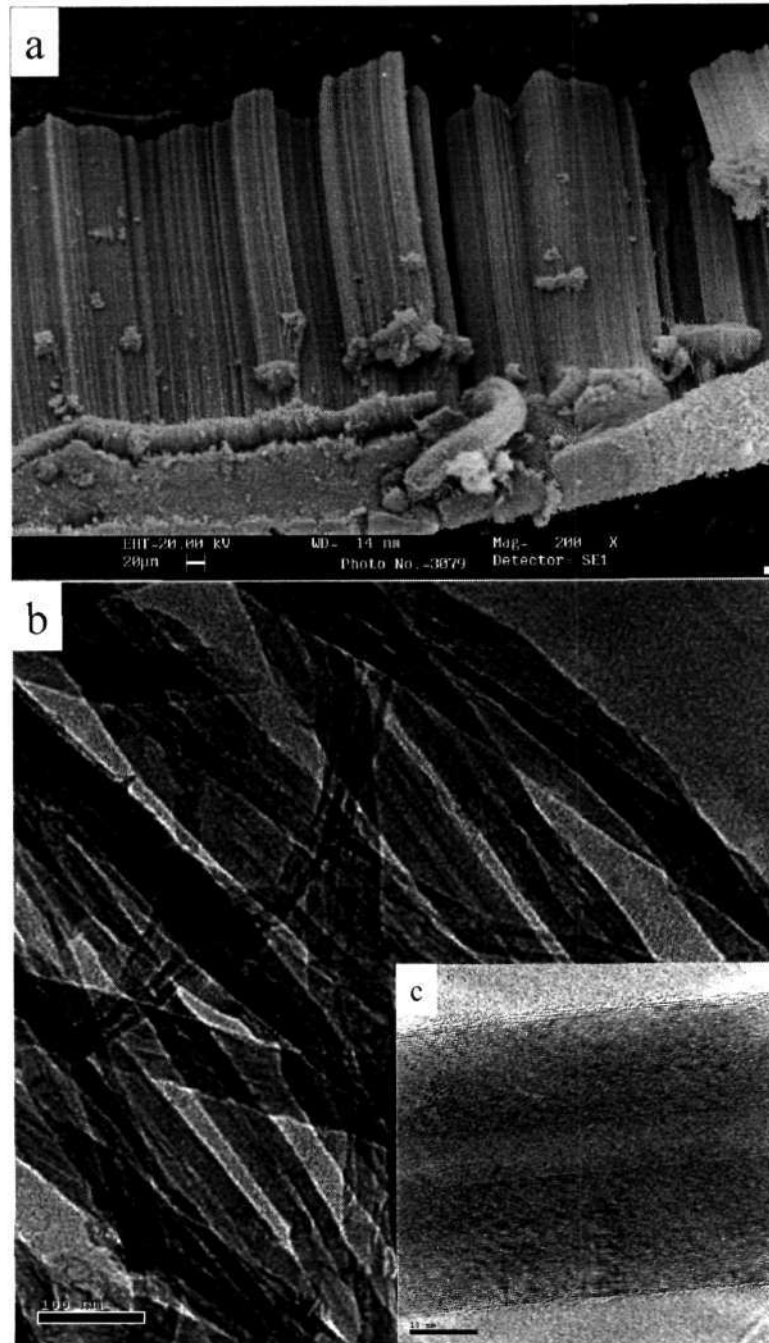


Figure 2.15: (a) SEM image of aligned MWNTs obtained by the nebulization of $\text{Fe}(\text{CO})_5$ in the presence of 100 sccm acetylene. (b) TEM image of the aligned MWNTs. (c) HREM image of a MWNT

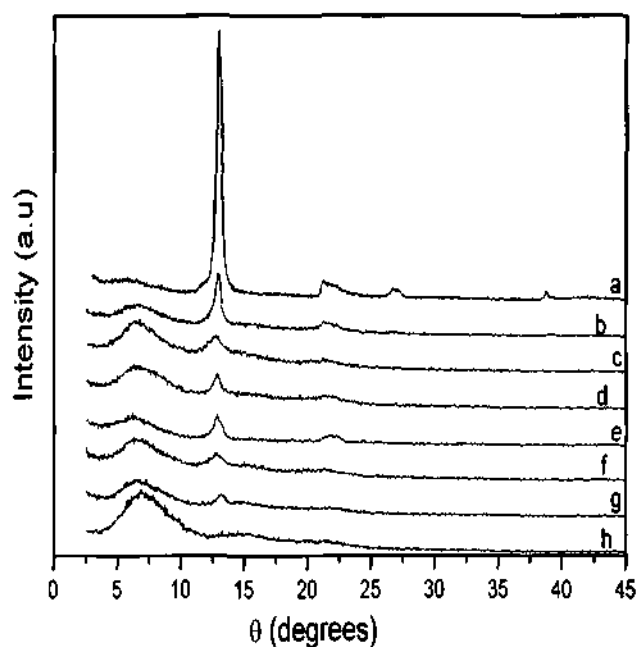


Figure 2.16: Powder X-ray diffraction pattern of (a) arc-discharge MWNTs, (b)-(h) MWNTs obtained in region III when xylene, toluene with acetylene, mesitylene, benzene, $\text{Fe}(\text{CO})_5$ -acetylene, n-hexane and toluene were used as the carbon sources.

2.5 Conclusions

Nebulized spray pyrolysis can be conveniently used for the continuous production of MWNTs. The quality of the product is dependent on the pyrolysis temperature, carrier gas flow rate, additional carbon sources used and the catalyst precursor concentration. Many of the hydrocarbons yield aligned MWNT bundles, and SWNTs were obtained in certain instances. The inclusion of acetylene to an atomized spray of ferrocene in toluene yield aligned MWNT bundles with a narrow diameter distribution. Nebulized spray pyrolysis of iron pentacarbonyl in the presence of acetylene also yield aligned MWNT bundles. Well-graphitized MWNTs were obtained when xylene was used as the additional carbon source.

Chapter 3

A NEW METHOD OF PURIFICATION OF CARBON NANOTUBES BASED ON HYDROGEN TREATMENT

3.1 Introduction

Multi-walled carbon nanotubes (MWNTs) are generally synthesized by the arc evaporation of graphite or by the pyrolysis of hydrocarbons over metal nanoparticles. Single-walled carbon nanotubes (SWNTs) have been produced by arc evaporation as well as by laser ablation of metal-impregnated graphite rods. MWNTs, SWNTs and aligned carbon nanotube bundles are obtained in a single step by the pyrolysis of organometallic precursors (Chapter 1 for more details). The as-synthesized nanotubes usually contain impurities such as amorphous carbon and metal nanoparticles, the latter being specially prominent when metal catalysts are employed.

Purification of carbon nanotubes, therefore, is an important problem in carbon nanotube research. Acid-washing eliminates metal particles to an extent but this is inhibited by the graphitic carbon coating on the metal particles. Dujardin et al. [99] have employed acid washing and air oxidation to purify SWNTs obtained by laser ablation, while Smalley and coworkers [100] have used micro-filtration to eliminate amorphous carbon and catalyst particles. Fullerenes are also removed by solvent extraction. Tohji et al. [101] have used hydrothermal treatment to remove the amorphous carbon from the nanotube surface. Most of the procedures reported in the literature [99–101] employ air oxidation for removing the amorphous carbon. Margrave and coworkers [102] have outlined the use of gas-phase based on

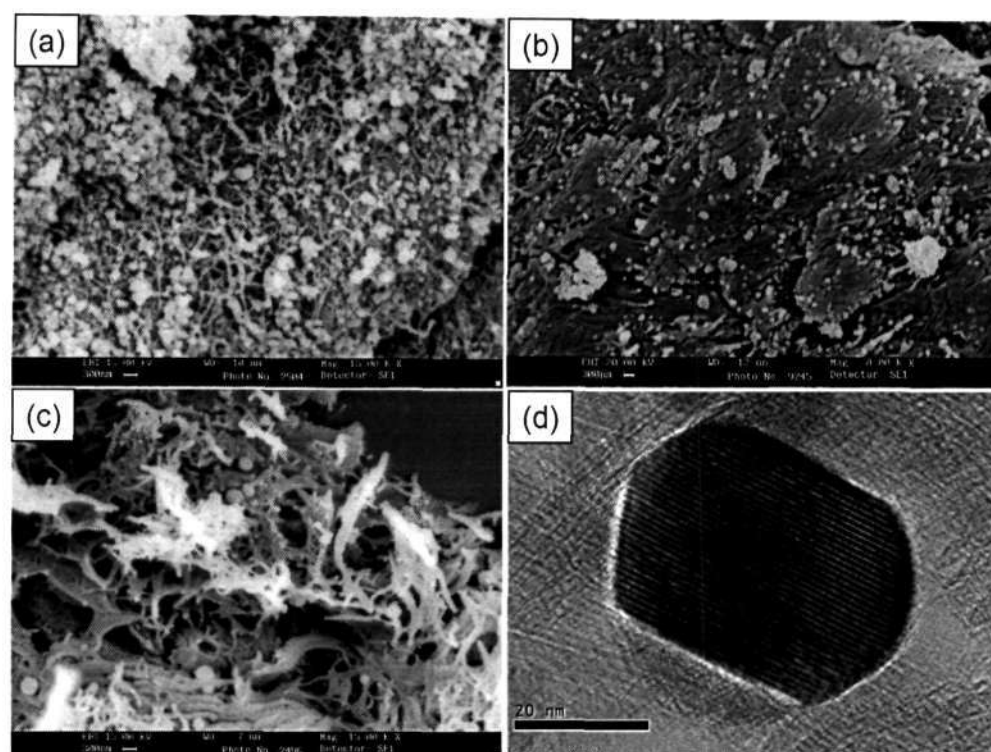


Figure 3.1: SEM images of (a) as-synthesized arc-SWNTs, (b) after acid washing and (c) after first hydrogen treatment. (d) TEM image of an agglomerated metal particle after first hydrogen treatment.

selective oxidation of carbonaceous impurities for the purification of SWNTs. Metal catalyst particles present in the as-synthesized sample often catalyze the oxidation of SWNTs. High-temperature annealing of the purified samples helps in the removal of the functional groups created on the nanotube surface during the acid treatment and the purification procedures are sample dependent [103]. Martinez et al. have suggested the use of air oxidation and microwave acid digestion to purify arc-discharge SWNTs [104]. Sen et al. have examined the effect of oxidation conditions on the sample purity on SWNTs prepared by arc-discharge method and have used Near Infrared (NIR) spectroscopy to quantify the SWNT purity [105]. Wiltshire et al. [106] have reported a comparative study of acid and thermal oxidative treatment of HiPCO SWNTs. Due to the importance of purification in nanotube research, we have explored an alternative method involving high-temperature

hydrogen treatment. The method has been most effective in purifying both SWNTs by arc-discharge and laser ablation as well as MWNTs. We have also studied the efficacy of this strategy for the purification of SWNTs obtained by the high pressure CO disproportionation (HiPCO).

3.2 Experimental

Arc discharge SWNTs (arc SWNTs) were synthesized by the method as reported by Journet et al. [10] using a composite rod containing Y (1 at.%) and Ni (4.2 at.%) as the anode and a graphite rod as the cathode, under a helium pressure of 660 torr with a current of 100 A and 30 V. The nanotubes were heated in air at 300 °C for 12 h and then stirred in conc. HNO₃ at 60 °C for 24 h in order to dissolve the metal nanoparticles. The product was washed with distilled water, dried, dispersed in ethanol under sonication, and filtered using Millipore (0.3 μm) filter paper. The filtered product was dried in an oven at 100 °C for 2 h. The sample was heated to 1000 °C in a furnace at a rate of 3 degrees per minute, in flowing hydrogen at 100 sccm (standard cubic centimeter per minute) and held at that temperature for 2 h. The resulting sample was again stirred in conc. HNO₃ at 60 °C for 3 h and finally heated in a furnace at 1000 °C for 2 h in flowing hydrogen (100 sccm). A similar procedure was employed for the purification of SWNTs obtained by laser ablation (laser SWNTs). A CS₂ extraction was carried out on the laser SWNTs and subsequently treated with 8 N HCl at 60 °C for 24 h to dissolve the metal nanoparticles. The nanotubes were heated in flowing hydrogen (100 sccm) at 1000 °C for 2 h and the product was again stirred with 8 N HCl at 60 °C for 3 h and finally heated at 1000 °C for 2 h in flowing hydrogen (100 sccm). We have carried out similar experiments with HiPCO SWNTs. In the case of HiPCO SWNTs the samples were heated at 800 °C instead of 1000 °C. Suspensions of SWNTs for recording Visible-NIR

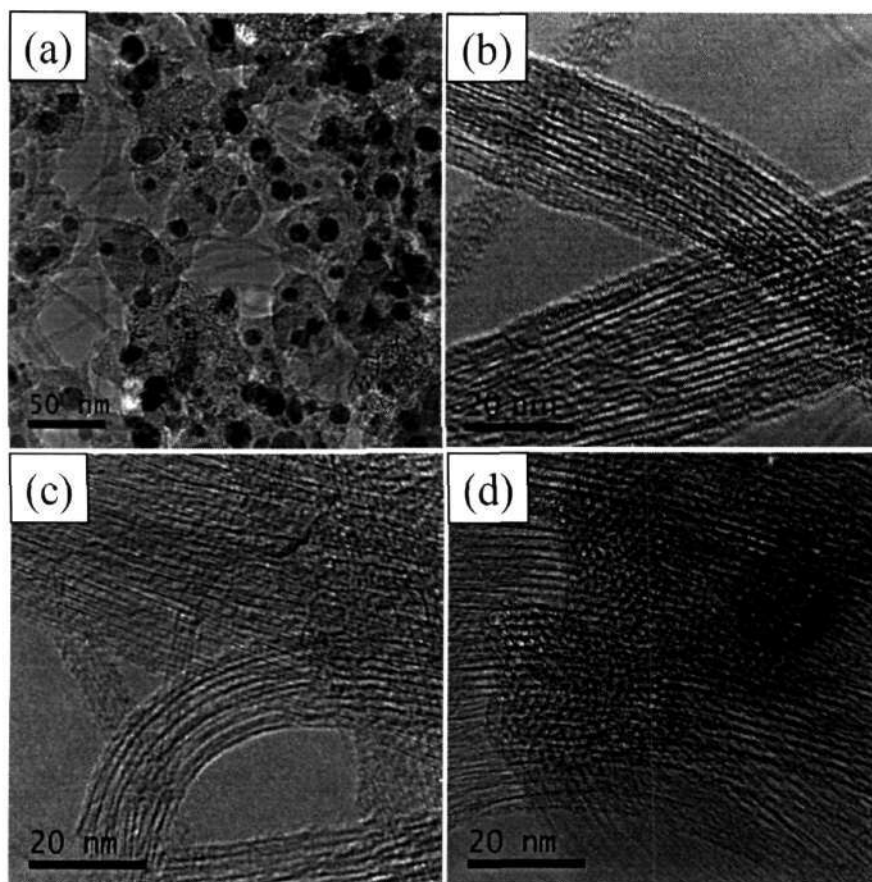


Figure 3.2: TEM images of (a) as-synthesized arc SWNTs, (b) after first acid washing, (c) after first hydrogen treatment and (d) after second hydrogen treatment.

spectroscopy were prepared as reported by O'Connell et al. [107]. We used H_2O instead of D_2O . Arc-discharge MWNTs were prepared by striking an arc between two graphite electrodes in a He atmosphere. The cathodic deposit was collected, powdered and sonicated in ethanol to separate the nanotubes from the heavier turbostatic graphite. The nanotubes were then refluxed in a 2:1 mixture of conc. HNO_3 and conc. H_2SO_4 (acid treated MWNTs) for 20 h. The acid treated MWNTs were hydrogen treated at 1100°C for 2 h. Aligned MWNT bundles were obtained by ferrocene pyrolysis (see chapter 2) and were subjected to acid treatment before they were heated in hydrogen at 1100°C . The nanotubes were characterized at each stage by powder X-ray diffraction, Scanning Electron Microscopy (SEM), Transmission Electron

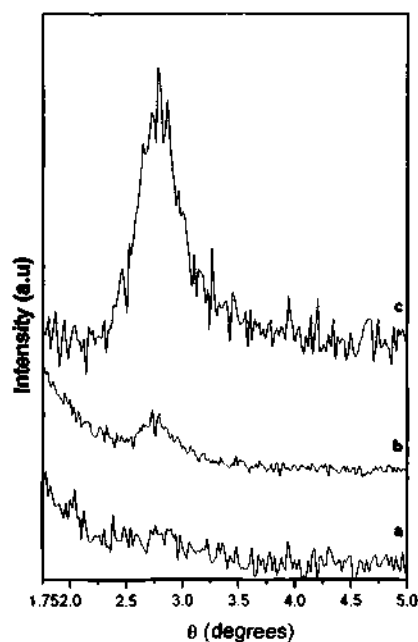


Figure 3.3: XRD pattern of (a) as-synthesized arc SWNTs, (b) after first acid washing and (c) after the second hydrogen treatment.

Microscopy (TEM) and Raman spectroscopy. The powder X-ray diffraction patterns were recorded using a Seifert XRD 3000 TT instrument. The SEM images were obtained with a Leica S-440I microscope and TEM images with a JEOL JEM 3010 instrument operating at an accelerating voltage of 300 kV. Raman measurements were performed in a 90° geometry using a Jobin Yvon TRIAX 550 triple grating spectrometer equipped with a cryogenic charge-coupled device camera, using diode-pumped frequency doubled solid state Nd:YAG laser of 532 nm (Model DPSS 532-400, Coherent Inc. USA).

3.3 Results and Discussion

The as-synthesized arc SWNTs contain a large amount of impurities as seen in the SEM image in Figure 3.1(a). TEM images reveal the presence of amorphous carbon and metal nanoparticles apart from SWNT bundles

(Figure 3.2(a)). The image also reveals that the SWNTs bundles have a diameter approximately 10 nm. Most of the metal nanoparticles got dissolved in the ensuing acid washing, but the nanotubes are covered with amorphous carbon as can be seen in the electron microscope images in Figures 3.1(b) and 3.2(b). The amorphous carbon is removed by high-temperature hydrogen treatment while the small metal nanoparticles melt and agglomerate into larger particles as clearly visible from Figure 3.1(c). It is well known that the melting points of small clusters are much lower than the bulk. Figure 3.1(d) shows a TEM image of an agglomerated metal particle. In bulk, nickel (m.p 1453 °C) and yttrium (m.p 1522 °C) melt above the temperatures employed in our purification procedure. Melting and agglomeration of the metal nanoparticles occurs in the 750 – 850 °C range. The absence of amorphous carbon is clearly evident from the TEM image in Figure 3.2(c). TEM images also reveal that the bundles grow in size and have diameters in the range 20-50 nm after the hydrogen treatment. These metal particles are removed second acid washing carried out for a shorter duration. The second acid treatment is followed by the high temperature hydrogen treatment at 1000 °C to obtain pure SWNTs. A TEM image of the purified SWNTs is shown in Figure 3.2(d). We do observe any hollow onion-like structures often found in SWNTs purified by other methods [101], indicating thereby that carbon covering on the metal particles is etched away by hydrogen.

SWNTs form a triangular lattice and give a distinctive low angle reflection in the XRD pattern [11]. In Figure 3.3, we show the low-angle XRD patterns of the as-synthesized and acid-treated SWNTs as well as those obtained after second hydrogen treatment. The (1,0) diffraction line is not observed in the case of as-synthesized SWNTs and appears as a small hump in acid treated SWNTs. This line is seen as an intense peak in the case of second hydrogen-treated sample. The mean diameter of the purified SWNTs is estimated to

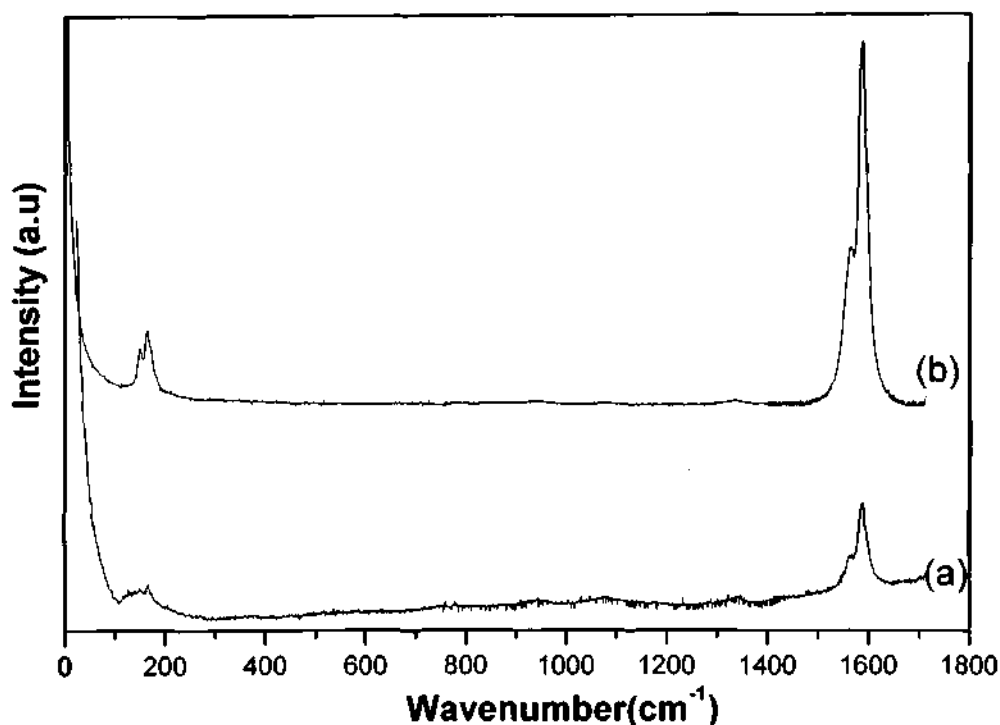


Figure 3.4: Raman spectra of arc SWNTs- (a) as-synthesized and (b) after second hydrogen treatment.

be 1.52 nm from the (1,0) diffraction line. The diameters of the SWNTs were calculated using the relationship:

$$D = (d_{11} / \text{Cos}(\theta)) - 0.312 \text{ nm}$$

The G-band and the radial-breathing modes of SWNTs in the Raman spectra are strong in intensity while the other Raman modes are weak. The Raman spectra of the as-synthesized and purified arc SWNTs is shown in Figure 3.4. The as-synthesized sample (curve (a)) shows a G-band which is split into two bands at 1562 cm^{-1} and 1586 cm^{-1} . The D-band appears as a broad peak centered at 1343 cm^{-1} indicating that the sample contains amorphous carbon. The second order Raman bands appears as weak peaks centered at 941 cm^{-1} and 1075 cm^{-1} . The purified sample shows an intense split G-band (1563 cm^{-1} and 1585 cm^{-1}) and strong radial-breathing modes. The D-band is considerably weaker after hydrogen treatment. The diameter

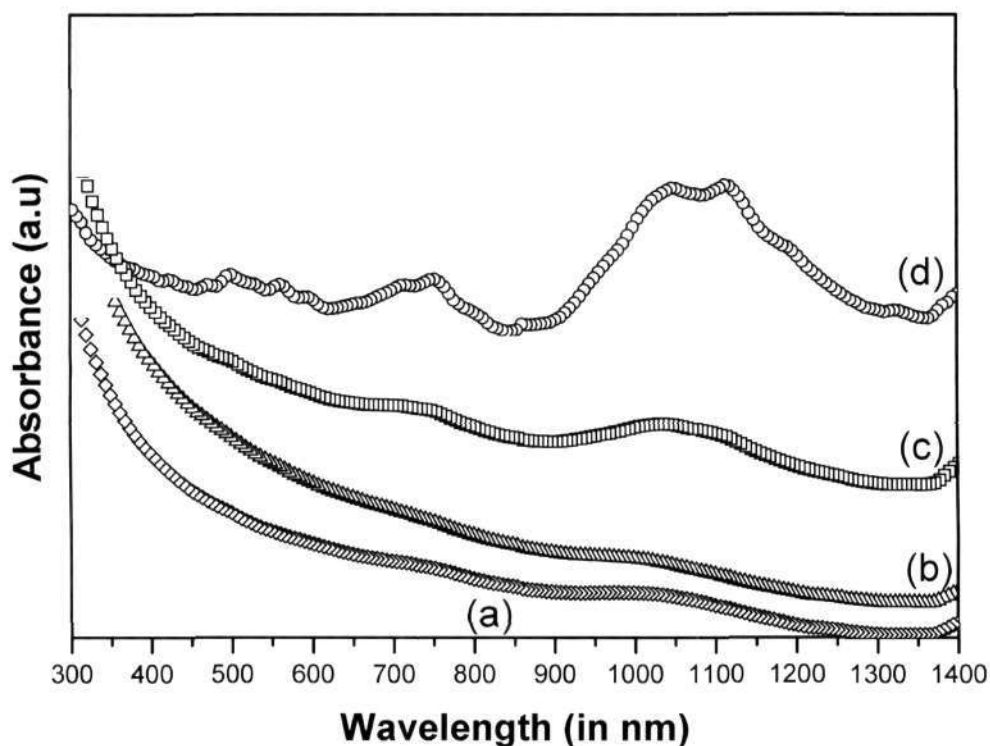


Figure 3.5: Visible-NIR spectra of arc SWNTs- (a) as-synthesized, (b) after acid washing , (c) after first hydrogen treatment and (d) final product.

of the SWNTs can be calculated from the radial breathing modes by using the formula:

$$D = 248 \text{ cm}^{-1} / \nu \text{ (in cm}^{-1}\text{)}$$

The radial breathing modes show the diameters lie in the range 1.32-1.89 nm, in agreement with the calculated diameter distribution obtained from TEM images and low-angle x-ray diffraction. The Visible-NIR spectra of the arc SWNTs at various stages of purification is shown in Figure 3.5. Due to their one-dimensional nature, carbon nanotubes exhibit van Hove singularities in the electronic density of states. Visible NIR spectroscopy provides additional evidence to the one-dimensional nature. The peak centered at 1100 nm is due to the second van Hove singularity transition and the second set of peaks near 700 nm due to the first van Hove singularity transition of metallic nanotubes. The intensity of the two bands increases markedly on

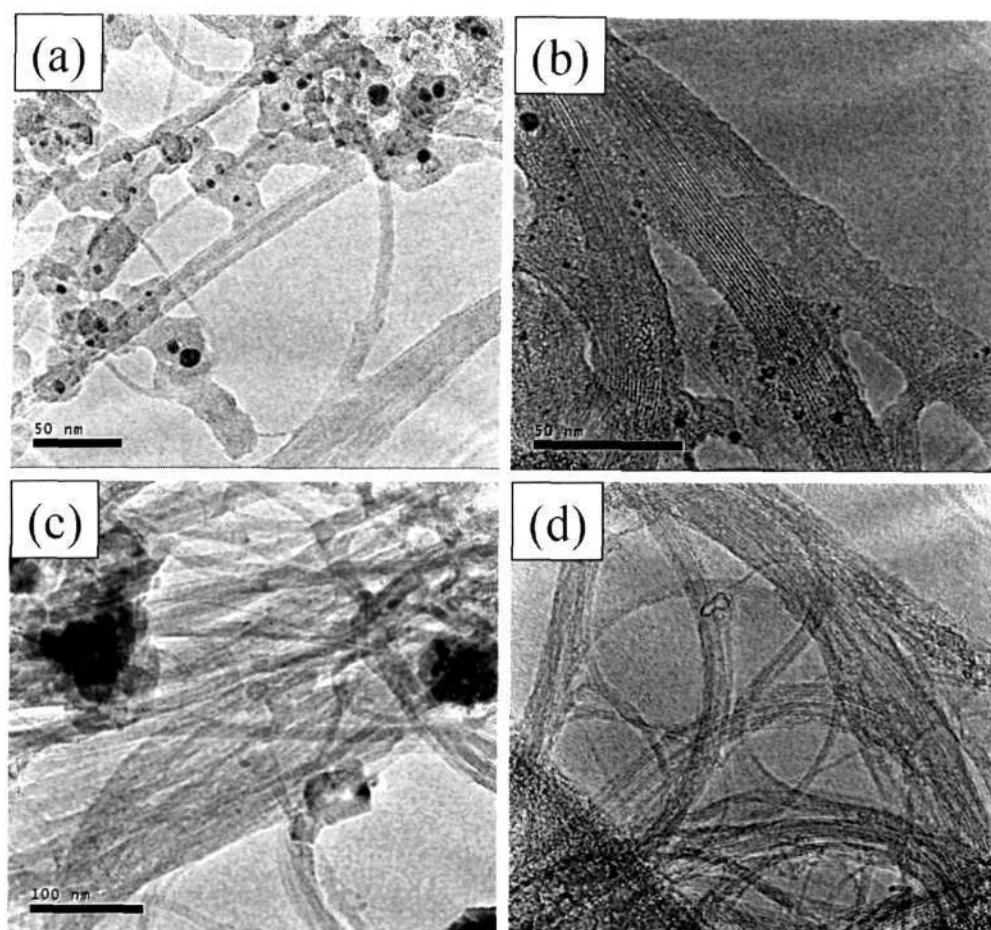


Figure 3.6: TEM images of laser SWNTs- (a) as-synthesized, (b) after first acid washing, (c) after first hydrogen treatment and (d) after second hydrogen treatment.

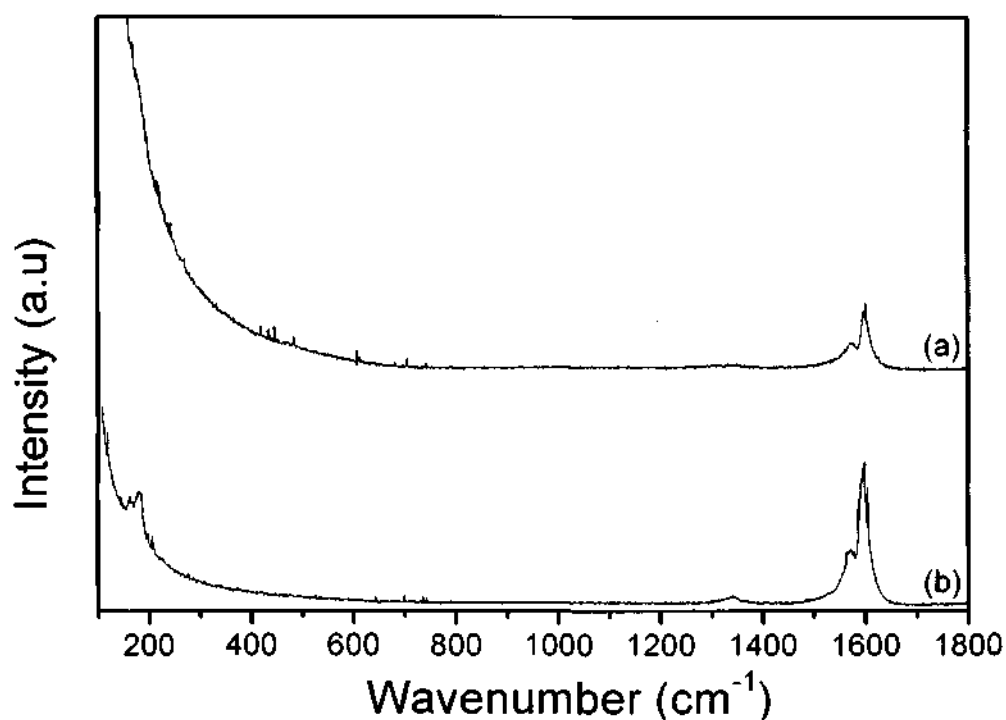


Figure 3.7: Raman spectra of laser SWNTs after (a) first acid washing and (b) second hydrogen treatment.

hydrogen treatment.

We have carried out hydrogen treatment of SWNTs obtained by laser ablation. The TEM images in Figure 3.6 show the laser SWNTs at various stages of purification. The average diameter of the SWNTs was approximately 1.4 nm. Fullerenes, metal nanoparticles, amorphous carbon and SWNT bundles are present in the as-synthesized laser SWNTs (Figure 3.6(a)). The fullerenes were removed by CS₂ extraction and the metal nanoparticles were partly dissolved in acid. After the acid washing, amorphous carbon continues to cover the SWNTs (Figure 3.6(b)). This amorphous carbon was removed by a hydrogen treatment at 1000 °C as can be seen in Figure 3.6(c). Similar to the arc SWNTs, we observe an agglomeration of the undissolved metal nanoparticles, which could be removed by the subsequent acid treatment. The nanotubes heated again in hydrogen at

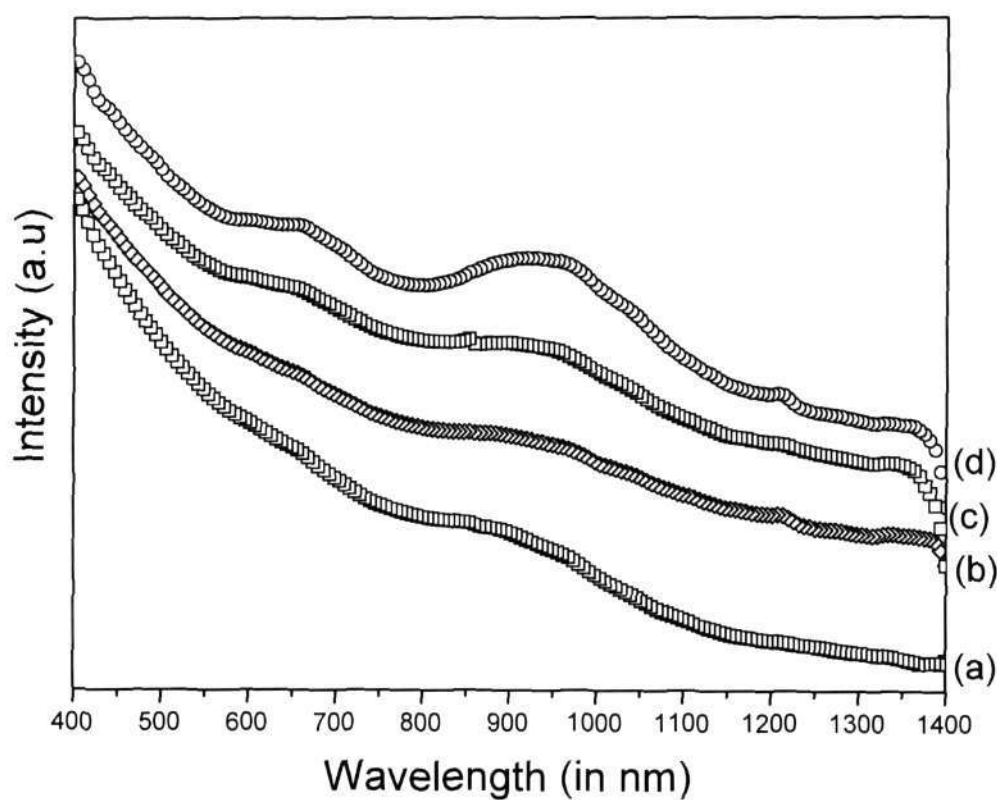


Figure 3.8: Visible-NIR spectra of laser SWNTs- (a) as-synthesized, (b) after first acid washing, (c) after first hydrogen treatment and (d) after second hydrogen treatment.

1000 °C were indeed of high purity (Figure 3.6(d)). The purity of the nanotubes was also revealed in the Raman and visible-NIR spectra. In Figure 3.7, we show the Raman spectra of the first acid washed laser SWNTs (curve (a)) and that after the second hydrogen sample (curve (b)). The Raman spectra of the acid washed laser SWNTs shows a weak doubly split G-band (1570 and 1596 cm^{-1}). The intensity of the G-band increases drastically after purification and the radial breathing modes are also clearly observed. The average diameter of the laser SWNTs, calculated from the radial breathing mode is 1.37 nm in line with the TEM observations. The visible-NIR spectra of laser SWNTs at various stages of purification is similar to that of the arc SWNTs as their diameters are comparable (Figure 3.8).

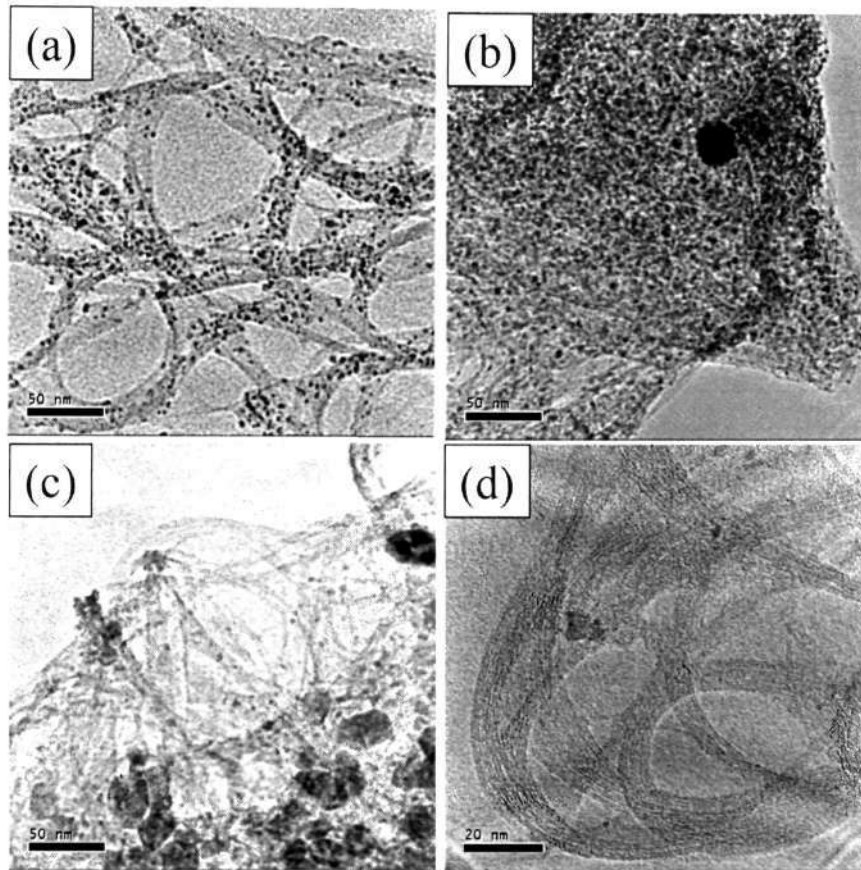


Figure 3.9: TEM images of (a) as-synthesized HiPCO SWNTs, (b) after first acid washing, (c) after first hydrogen treatment and (d) after second hydrogen treatment.

The TEM image in Figure 3.9 (a), reveals the presence of metal nanoparticles and amorphous carbon in the as-synthesized HiPCO SWNTs. Large quantities of SWNT bundles with an average diameter of $\bar{20}$ nm are also seen. The SWNTs agglomerate into larger bundles after acid washing (Figure 3.9(b)). The undissolved metal nanoparticle agglomerate into larger particles after hydrogen treatment at 800 °C (Figure 3.9(c)). We do not observe amorphous carbon after the hydrogen treatment. The metal nanoparticles got readily dissolved in the ensuing acid washing and the SWNTs were again hydrogen treated at 800 °C. The Raman spectra of acid treated and final hydrogen treated HiPCO SWNTs is shown in Figure 3.10A. The intensity of both the G-band and the radial breathing modes is higher in the case of the

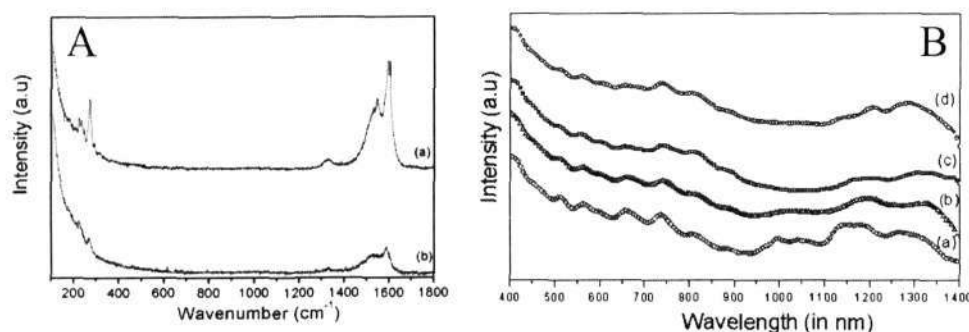


Figure 3.10: A- Raman spectra of HiPCO SWNTs after (a) first acid washing and (b) second hydrogen treatment.; B-Visible-NIR spectra of HiPCO SWNTs- (a) as-synthesized, (b) after first acid washing, (c) after first hydrogen treatment and (d) after second hydrogen treatment.

acid treated SWNTs. The diameter distribution is bimodal with the average diameters of 1.09 nm (228 cm^{-1}) and 0.9 nm (273 cm^{-1}). The intensity the 273 cm^{-1} band decrease drastically with hydrogen treatment. The visible-NIR spectra in Figure 3.10B show no significant change in the intensity of the bands. There is a slight change in the band due to the transition between the second van Hove singularity of semiconduction nanotubes (band from 950-1400 nm, see curve 3.10B (a)). The band is broad due the large variation in the diameters and the chirality of SWNTs present in the sample. After hydrogen treatment the band narrows (1100-1400 nm). This could be due to the etching of small diameter SWNTs by hydrogen. The SWNTs obtained by the HiPCO process are defective and are not as crystalline as those obtained by the laser ablation or arc-discharge processes.

We have examined the efficacy of the high temperature hydrogen treatment procedure for MWNTs. Acid treated MWNTs contain a large amount of amorphous carbon as seen in the SEM and TEM images in Figures 3.11(a) and (b). The amorphous carbon is removed by the high temperature hydrogen treatment (Figures 3.11(c) and (d)). The high resolution electron microscope (HREM) image shown as an inset in Figure 3.11(b) indicates that

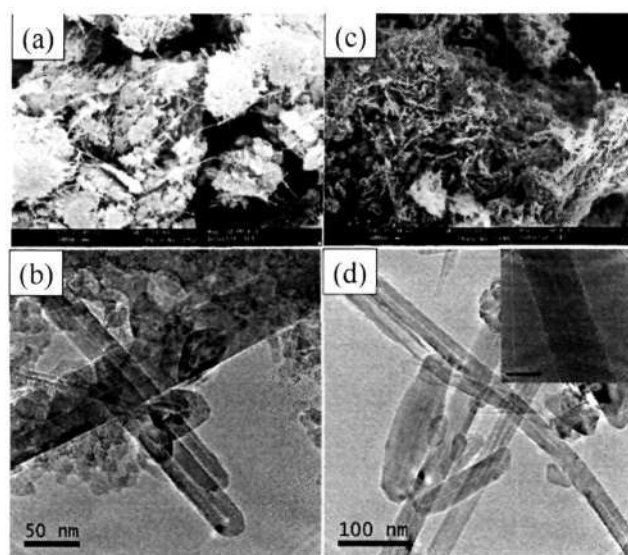


Figure 3.11: (a) SEM image of acid refluxed arc discharge MWNTs, (b) SEM image after hydrogen treatment at 1100 °C. (c) and (d) are the respective TEM images.

the crystalline nature of the MWNTs is well-preserved after the acid and hydrogen treatment. The Raman confirm the high purity of the MWNTs subjected to these treatments (Figure 3.12). The G/D band intensity improves significantly after hydrogen treatment.

We find that aligned carbon nanotubes are also effectively purified by high temperature hydrogen treatment as revealed by the TEM images in Figure 5.13. We have carried out thermogravimetric analysis of MWNTs and SWNTs just after acid treatment and after hydrogen treatment. The main difference is that the low temperature weight loss due to amorphous carbon is not found after hydrogen treatment. In the case of laser SWNTs, the oxidation temperature is substantially increased after purification.

3.4 Conclusion

In conclusion, we have developed a new and effective method for the purification of SWNTs and MWNTs. The method involves acid washing followed by

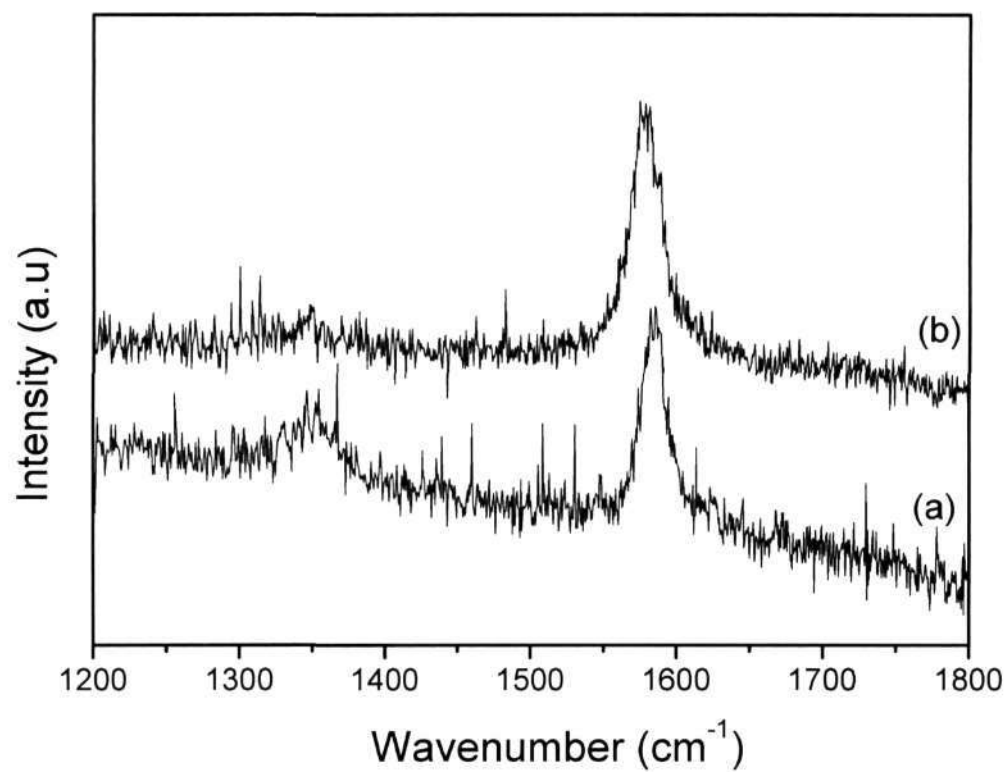


Figure 3.12: Raman spectra of arc-discharge MWNTs after : (a) acid reflux and (b) hydrogen treatment at 1100 °C.

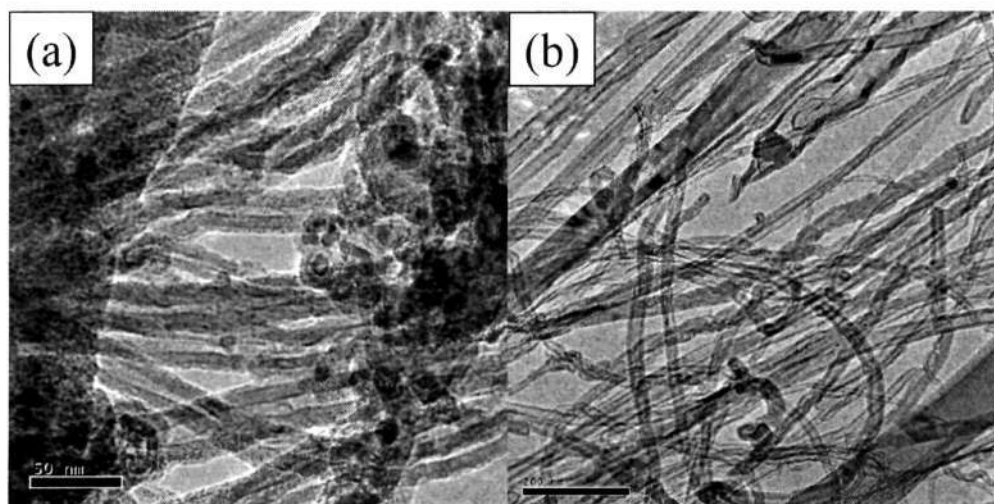


Figure 3.13: TEM images of pyrolysis MWNTs- (a) as-synthesized and (b) after hydrogen treatment at 1100 °C.

the high-temperature hydrogen treatment repeated twice. Excellent SWNTs containing little or no amorphous carbon and metal particles are obtained by this means, as verified by microscopy, XRD and spectroscopic techniques.

Chapter 4

A NEW METHOD FOR THE PREPARATION OF METAL NANOWIRES BY THE NEBULIZED SPRAY PYROLYSIS OF PRECURSORS

4.1 Introduction

Nanowires constitute an important class of 1D nanomaterials, which provide models to study the relationship between electrical transport, optical and other properties with dimensionality and size confinement. In recent years, several methods have been described for the synthesis of nanowires of different materials [3,68]. General methods for the synthesis include methods involving vapor-solid or vapor-liquid-solid growth and the use of templates such as anodic alumina membranes (AAO) [108,109], carbon nanotubes [110], etc. Nanowires of metals such as Au and Ag have been synthesized by a seed-mediated approach as well as by solution-based methods [111–113]. Laser ablation has been employed to obtain nanowires of Si and Ge [74].

In this chapter, we outline the use nebulized spray pyrolysis (NSP) of solutions of simple metal precursors for the preparation of metal nanowires. This technique has been used earlier for the preparation of thin films and of oxide powders [94–96]. The method is simple, template-free and inexpensive. The versatility of this method is demonstrated by the synthesis of single-crystalline nanowires of zinc, cadmium and lead. It is noteworthy that there are very few reports in the literature on the synthesis of zinc and lead nanowires, and no report on cadmium nanowires. For example, zinc

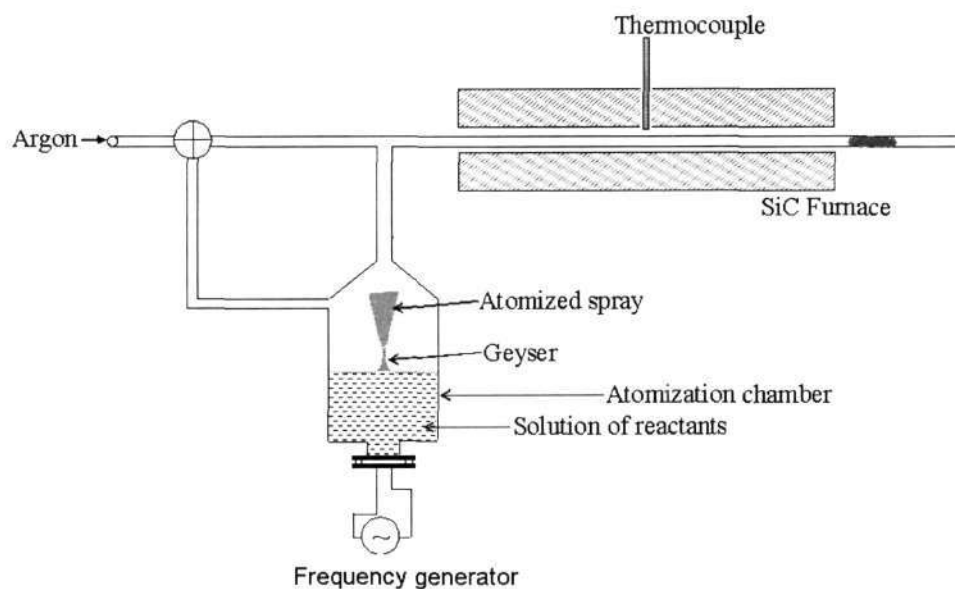


Figure 4.1: Schematic diagram of the experimental set-up used for the synthesis of metal nanowires.

nanobelts have been obtained by the carbothermal reduction of ZnS [114], while nanowires are prepared by the reduction of ZnO with graphite in an NH_3 atmosphere [115]. Single-crystalline lead nanowires have been synthesized by the decomposition of lead acetate in ethylene glycol [116]. In the NSP process, we have employed methanolic solutions of metal acetate to produce nanowires of zinc, cadmium and lead. We have also studied the effect of oxidation on the zinc and cadmium nanowires.

4.2 Experimental

The schematic diagram of the experimental set-up used for the synthesis of metal nanowires is illustrated in Figure 4.1. All chemicals were obtained from Aldrich Chemicals. In a typical experiment, a methanolic solution of the acetate of zinc, cadmium or lead was prepared with a concentration of 40 g/l. This solution was nebulized and the spray carried into a pre-heated silicon carbide furnace maintained between 800 and 900 °C using Ar as a carrier

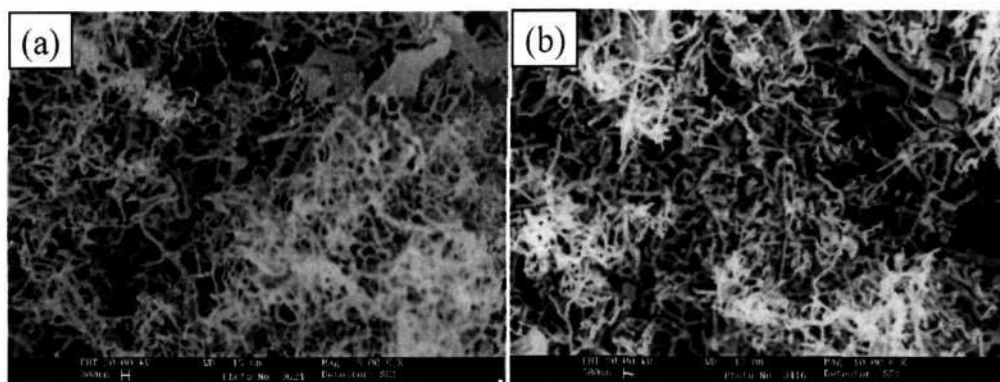


Figure 4.2: SEM image of zinc nanowires obtained by the NSP of methanolic solution of zinc acetate at (a) 800 °C and (b) 900 °C

gas. Typical flow rates of Ar used were between 500-1000 standard cubic centimeter per minute (sccm). All experiments were performed using a quartz tube with an inner diameter of 25 mm. The reaction was typically carried out for 30 min. The shiny deposits obtained at the outlet (shown in Figure 4.1) was used for further analysis. Powder X-ray diffraction (XRD) patterns were recorded using a Seifert XRD 3000 TT instrument. SEM images were obtained with a Leica S-440I microscope. TEM images were recorded with a JEOL JEM 3010 instrument operating at an accelerating voltage of 300 kV fitted with a Gatan CCD camera. The photoluminescence measurements were carried out at room temperature using a 325 nm excitation wavelength with a Perkin-Elmer model LS50B luminescence spectrometer. The Thermogravimetric analysis (TGA) of the samples was carried out on a Mettler-Toledo-TG-850 instrument.

4.3 Results and Discussion

Solutions of metal acetates in methanol were carried by a suitable carrier gas (Ar) into a preheated furnace to obtain nanowires of the corresponding metals. The product gets deposited in the cooler regions of the

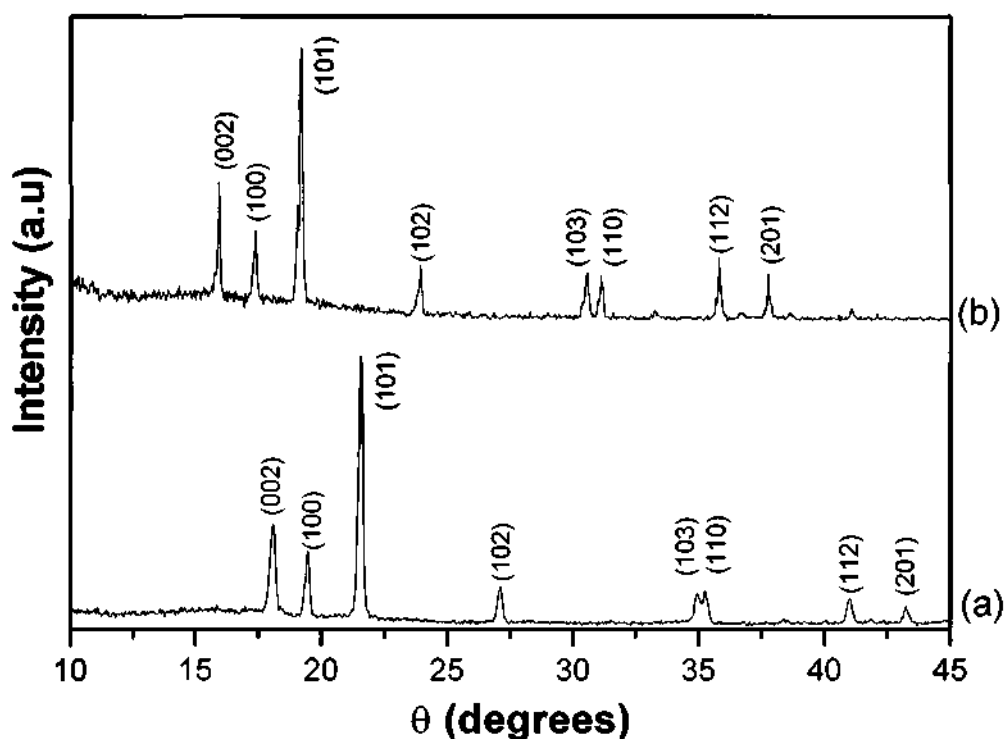


Figure 4.3: X-ray diffraction pattern of (a) zinc nanowires and (b) cadmium nanowires obtained by the NSP.

quartz tube (near the outlet, see Figure 4.1), where the temperature is in the 200 – 300 °C range. Zinc nanowires were obtained in copious quantities as a gray, shiny deposit when the pyrolysis of zinc acetate in methanol was carried out at 800 – 1000 °C. The scanning electron microscope (SEM) images of the nanowires reveal the length of the nanowires are in the order of several tens of microns (Figure 4.2). The XRD pattern shown in Figure 4.3(a), is characteristic of the hexagonal structure of zinc (JCPDS card: No. 04-0831, $a = 2.67 \text{ \AA}$ and $c = 4.95 \text{ \AA}$). Low-magnification transmission electron microscope (TEM) images in Figure 4.4(a) illustrates that nanowires have a diameters in the 50-100 nm range. The nanowires appear to have a zigzag morphology but there are no catalyst droplets at the wire ends. A few nanosheets of zinc were also occasionally observed (Figure 4.4(b)). The selected area electron diffraction pattern (SAED) of a nanowire is shown in Figure 4.4(c), shows

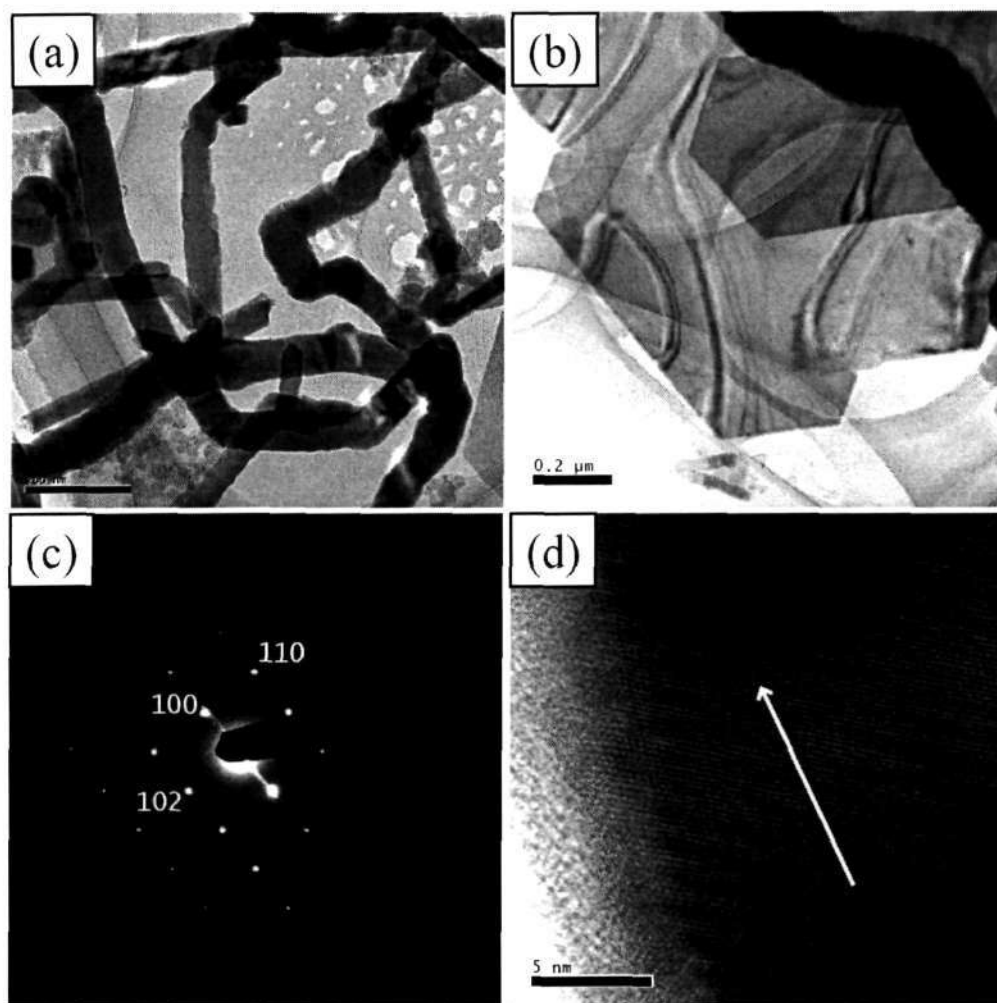


Figure 4.4: (a) and (b) low-magnification TEM images of zinc nanowires and nanosheets obtained by the NSP of methanolic solution of zinc acetate, (c) SAED pattern of a single zinc nanowire and (d) HREM image of a zinc nanowire. The arrow in (d) indicates the growth direction.

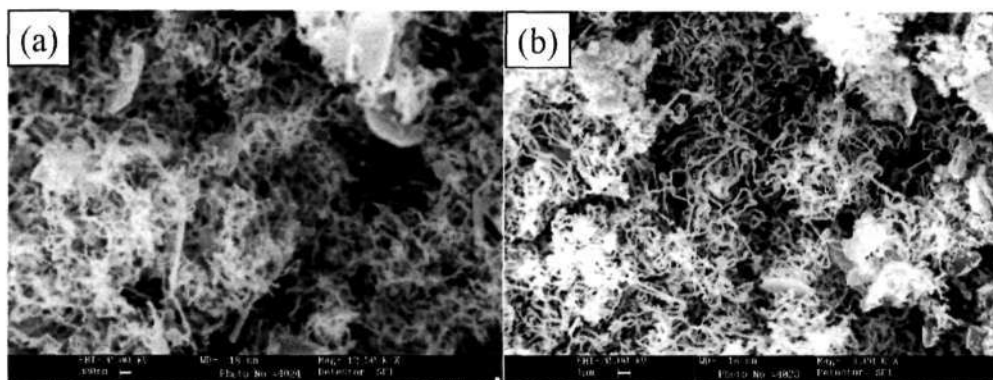


Figure 4.5: SEM images of cadmium nanowires obtained by the nebulized spray pyrolysis of cadmium acetate.

reflections due to the (102), (100) and (110) planes of zinc, confirming the nanowires to be single-crystalline. The high-resolution electron microscope (HREM) image of a single nanowire in Figure 4.4(d) has lattice spacing of 0.208 nm, corresponding to the (101) planes of zinc. The (101) plane makes an angle of 50° with the growth direction of the nanowire denoted by an arrow in the figure.

We have extended the synthetic procedure to obtain cadmium nanowires, which do not seem to have been reported hitherto. The gray deposit obtained at the outlet by using cadmium acetate as the metal source. SEM images in Figure 4.5 reveals the high yield of nanowires obtained. The nanowires were 60-150 nm in diameter and tens of microns in length. The XRD pattern of the nanowires is consistent with the hexagonal structure of cadmium (JCPDS card: No. 05-0674, P6/mmc, $a = 2.97 \text{ \AA}$ and $c = 5.62 \text{ \AA}$) as shown in Figure 4.3(b). The presence of cadmium nanowires and nanosheets is illustrated by the TEM images in Figure 4.6. The ends of the nanowires do not show the presence of any droplet as in the case of Zn nanowires. On increasing the temperature of the reaction from 800 to 1000 °C, the diameters of the nanowires obtained increased to approximately 700 nm. The HREM image of a single nanowire in Figure 4.7 shows a lattice spacing of 0.257 nm,

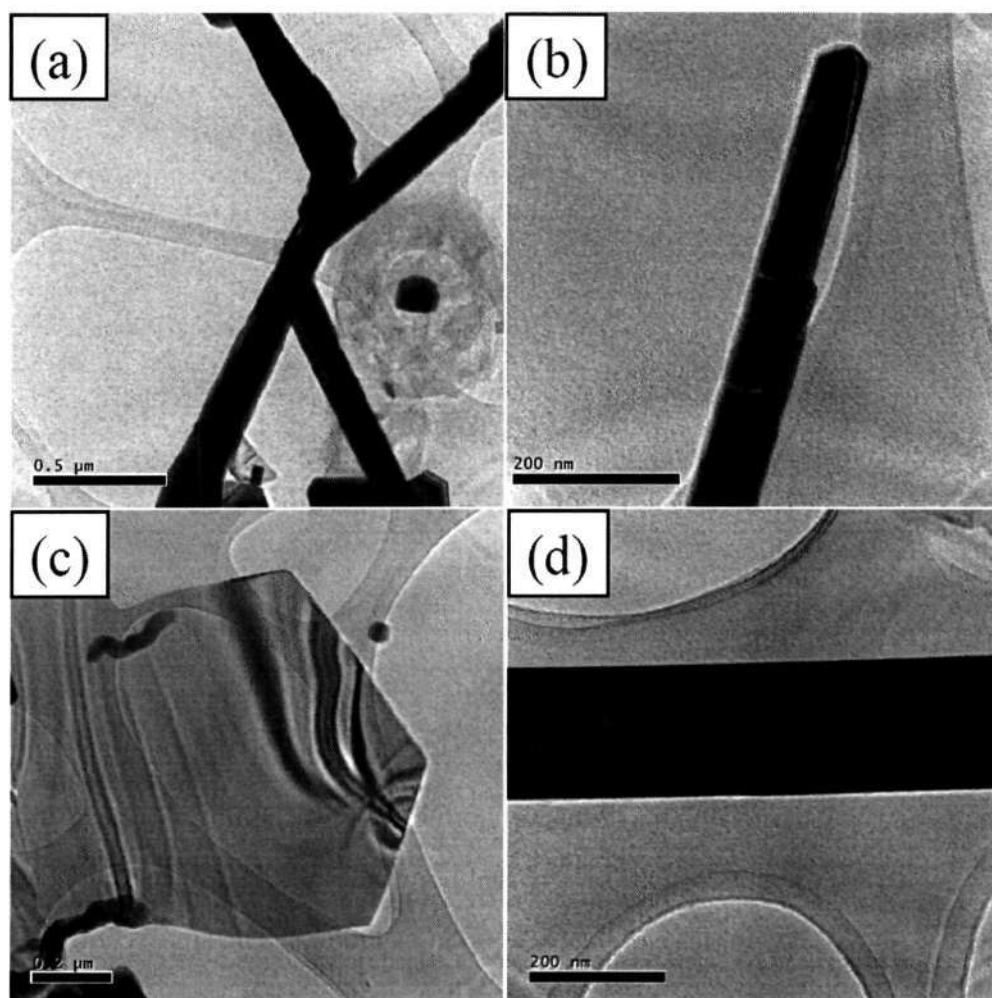


Figure 4.6: TEM images of cadmium nanowires and nanosheets obtained by the NSP of cadmium acetate in methanol at 800 °C.

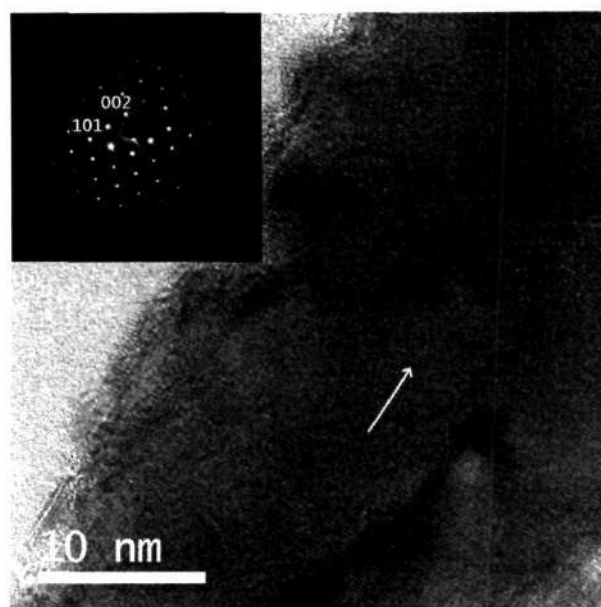


Figure 4.7: HREM of a cadmium nanowire. The arrow shows the growth direction. SAED of the nanowire is shown as inset

corresponding to the (100) lattice planes of cadmium.

The single-crystalline nature of the nanowires is also borne out by the SAED pattern of a nanowire given as an inset in Figure 4.7, the reflections corresponding to the (101) and (002) planes. Preliminary experiments show that it is possible to synthesize lead nanowires as shown by the SEM image in Figure 4.8. The nanowires have diameters between 50-100 nm with lengths of a few microns. The formation of metal nanowires by NSP of methanolic solutions of metal acetates can be understood as follows. The spray contains tiny droplets with diameters of 1-2 microns, which are transported by the carrier gas into the furnace maintained at 800–1000 °C. At this temperature, the melting and decomposition of the acetates into metal vapor occurs, probably aided by the hydrogen gas formed by the decomposition of methanol into hydrogen and carbon monoxide. No metal oxide impurity occurs due to the strong reducing atmosphere. The metal vapor condenses in the cooler regions on the quartz tube to form nanowires. The absence of metal droplets at the ends of the nanowires strongly suggests that the nanowires grow by

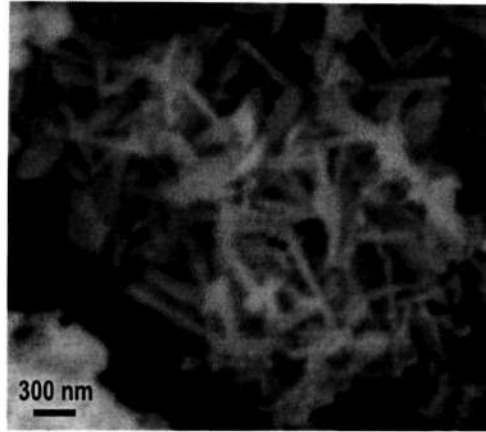


Figure 4.8: SEM image of lead nanowires obtained by the NSP of lead acetate in methanol at 1000 °C

the vapor-solid mechanism.

Conversion of one nanowire to another has been of interest. Gates et al. [117] have converted Se nanowires into Ag_2Se nanowires by using a soft chemistry. It was our aim to study the effect of oxidation on the Zn nanowires. The Zn nanowires were heated in air at 450 °C at a rate of 5 °C/ min for 4 h to yield ZnO as indicated by the XRD pattern in the inset of Figure 4.9(a) (JCPDS card: No. 36-1451, P63mc, $a = 3.25 \text{ \AA}$ and $c = 5.21 \text{ \AA}$). There was no impurity corresponding to Zn indicating the complete oxidation of the nanowires. The SEM image in Figure 4.10 reveals the nanostructures to be tubular in nature, although the dimensions are similar to those of the starting Zn nanowires.

We show TEM images in Figure 4.11(a) and (b) to demonstrate the hollow nature of the ZnO nanotubes, with diameters in the 60-100 nm range. The nanotubes are made-up of crystallites with a size of 10 to 20 nm, wherein each crystallite is single-crystalline. The SAED pattern shown in the inset of Figure 4.11(c) confirms that the nanotubes are made of such crystallites. The HREM image of a part of ZnO nanotube in Figure 4.11(d) shows a lattice spacing of 0.26 nm, corresponding to the (002) lattice planes of ZnO.

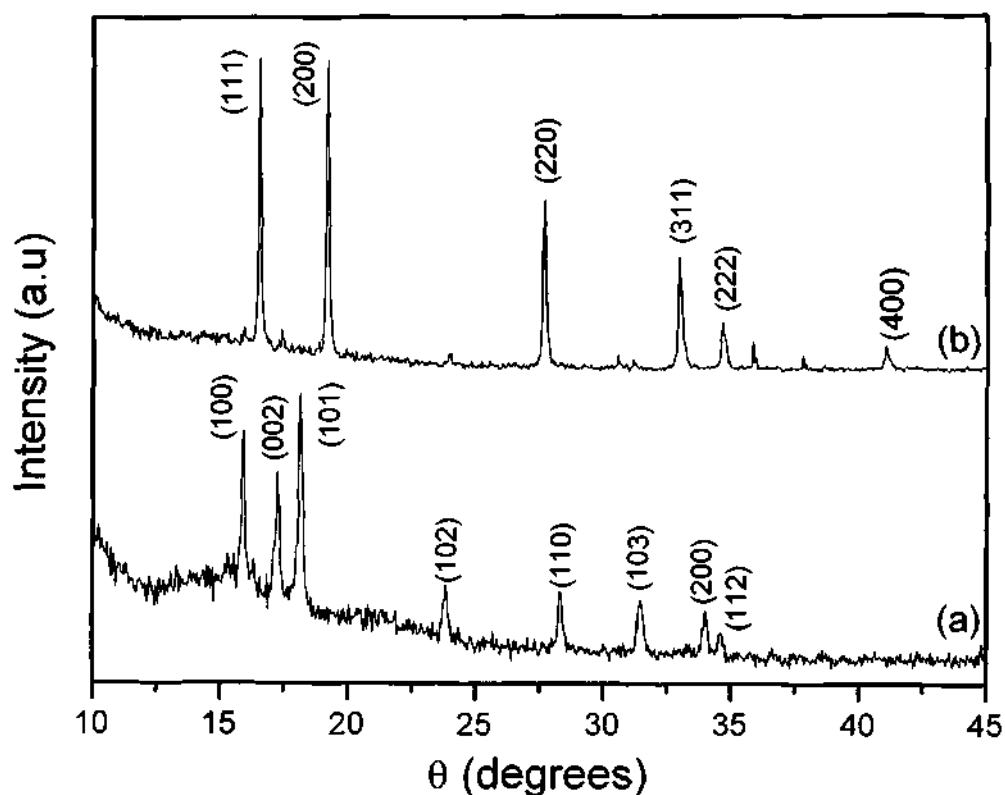


Figure 4.9: XRD patterns of (a) ZnO and (b) CdO obtained by the oxidation of zinc and cadmium nanowires.

Photoluminescence spectrum obtained by us show peaks at 382 nm, 435 nm and 485 nm (Figure 4.12). The 382 nm peaks is due to the band-edge emission while the origin of 435 nm and 485 nm peaks are not clear. ZnO is a wide bandgap (3.37 eV) semiconductor and has been extensively investigated for short wavelength light-emission, transparent conducting and piezoelectric material. Though there have been several reports on the synthesis of ZnO nanowires [118], there have been relatively fewer on ZnO nanotubes [119,120].

We also carried out oxidation of cadmium nanowires under similar conditions. The XRD pattern in Figure 4.9(b) reveals the conversion of hexagonal cadmium into cubic CdO (JCPDS card:No. 05-0640, $Fm\bar{3}m$, $a = 4.70 \text{ \AA}$). Most of the nanowires melt before they oxidized leading to the loss in morphology (Figure 4.13(a)). TEM images show the presence of necklace-like nanostructures (Figure 4.13(b)).

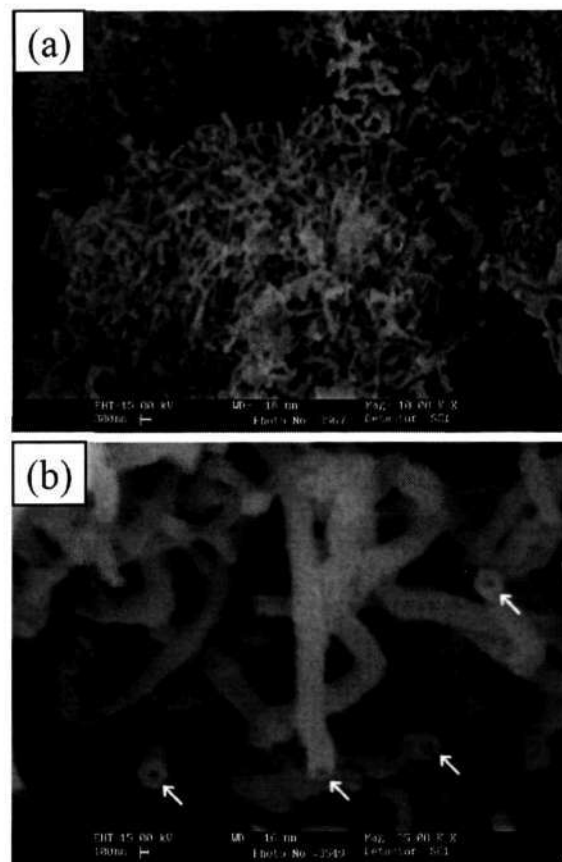


Figure 4.10: SEM images of ZnO obtained by the oxidation of zinc nanowires at 450 °C.

Thermogravimetric analysis of zinc nanowires and cadmium nanowires in flowing O₂ gas revealed that the oxidation begins at roughly 310 °C for zinc and 350 °C for cadmium (Figure 4.14), presumably at the surfaces of the nanowires, followed by the diffusion of metal from the center of the nanowire towards the surface. In the case of zinc, the metal gets oxidized into the oxide giving hollow ZnO nanotubes. The cadmium nanowires melt before they get oxidized (m.p. of cadmium is 320.9 °C) while zinc gets oxidized before it can melt (m.p. of zinc is 419 °C.)

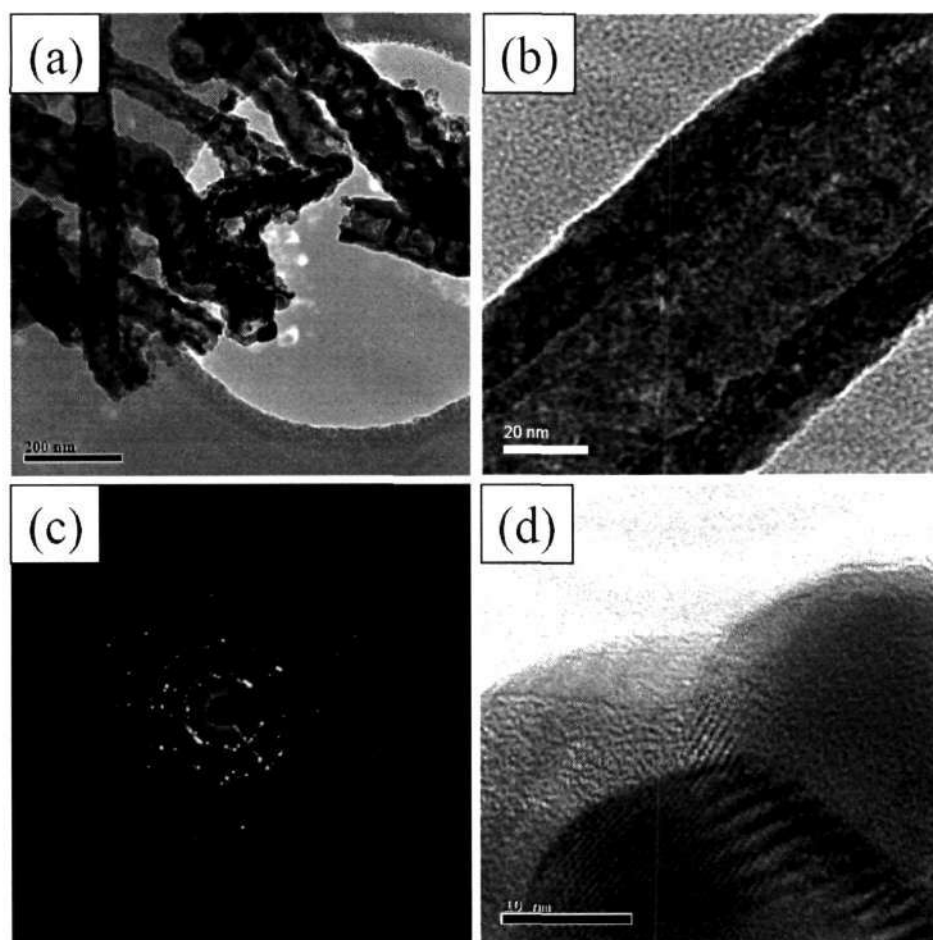


Figure 4.11: (a) and (b) TEM images of ZnO nanotubes, (c) SAED pattern of a ZnO nanotube and (d) HREM image of a part of ZnO nanotube.

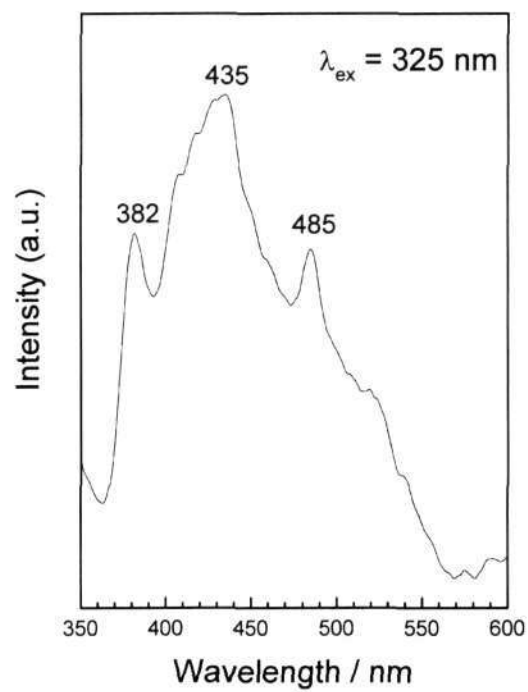


Figure 4.12: Photoluminescence spectrum of ZnO nanotubes.

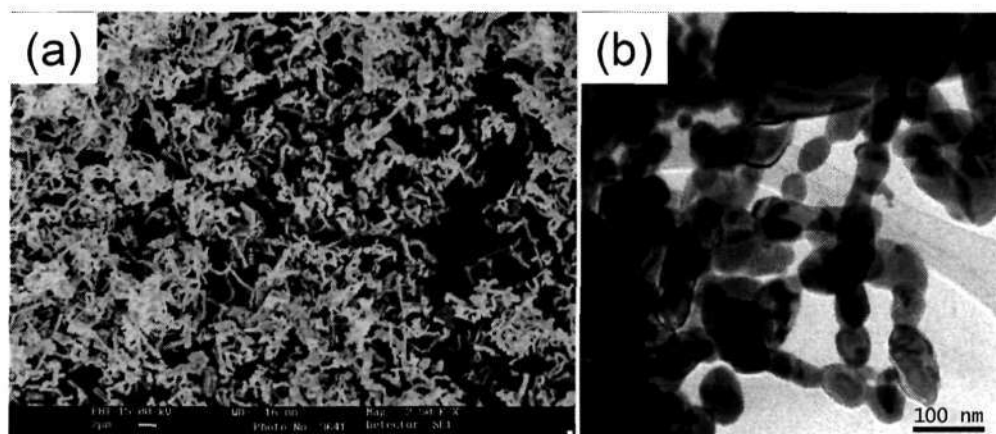


Figure 4.13: (a) SEM and (b) TEM image of CdO obtained by the oxidation of cadmium nanowires.

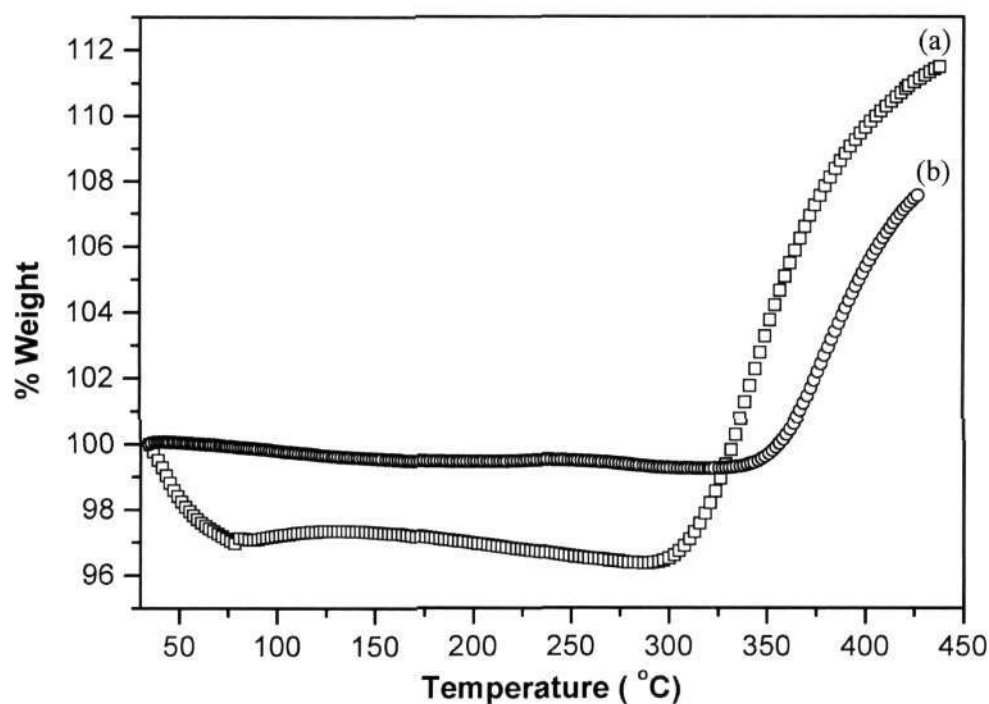


Figure 4.14: TG curves of (a) Zn nanowires and (b) Cd nanowires carried out under oxygen atmosphere.

4.4 Conclusions

In conclusion, we have demonstrated the synthesis of nanowires of three metals by the novel technique of nebulized spray pyrolysis. This can be extended to synthesize nanowires of other metals, elemental materials and alloys. An advantage of this method is that the nanowires obtained are in high yields and single-crystalline. Though we have used metal acetates as precursors, we believe that other metal salts soluble in methanol could be used to obtain metal nanowires by the nebulized spray pyrolysis route. It is noteworthy that we also can obtain nanostructures of oxides by the oxidation of the metal nanowires.

Chapter 5

POLYANILINE-CARBON NANOTUBE COMPOSITES

5.1 Introduction

Composites of carbon nanotubes with polymers and other materials would modify many of their properties [121]. Accordingly, there has been interest in studying composites of polyaniline (PANI) with carbon nanotubes. Aniline has been polymerized at carbon nanotube electrodes by Downs *et al.* [122] to obtain PANI films giving rise to novel surface characteristics and high current densities of the electrodes. Cochet *et al.* [123] have prepared PANI-nanotube composites by the in-situ polymerization of aniline in the presence of multi-walled carbon nanotubes (MWNTs). The composites so prepared had enhanced electronic properties. Films of PANI-MWNTs composites have been prepared by in-situ and ex-situ methods by Zengin *et al.* [124], who find that the electrical conductivity of the composites to be higher than that of the pristine nanotubes. We were interested in studying PANI composites with MWNTs as well as single-walled nanotubes (SWNTs). For this purpose, we have prepared PANI-nanotubes composites by in-situ polymerization of aniline in the presence of MWNTs and acid treated MWNTs. We have characterized these composites along with the PANI composites prepared with acid treated MWNTs subjected to treatment with thionyl chloride. We have carried out similar studies with SWNTs. We have measured electrical resistivities of the various PANI-nanotube composites.

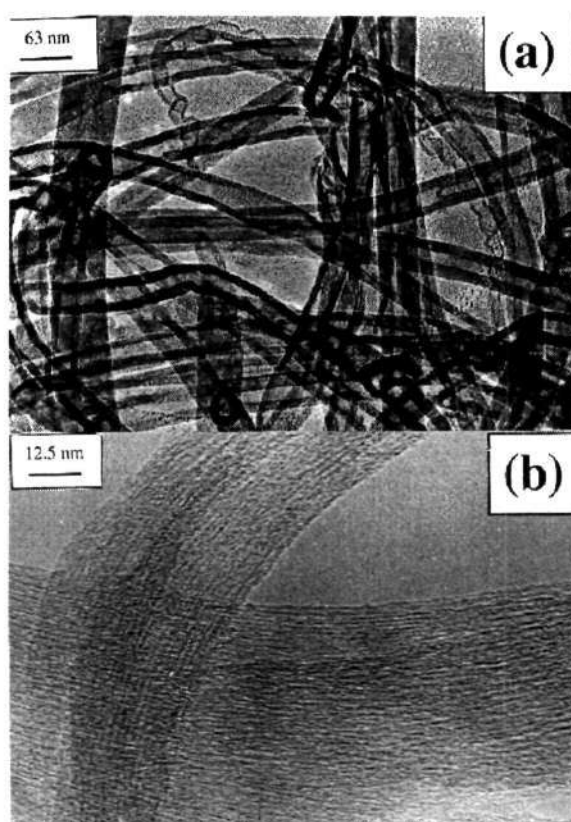


Figure 5.1: Representative TEM images of the nanotubes as synthesized for the preparation of PANI-nanotube composites- (a) pyrolysis MWNTs and (b) arc-discharge SWNTs

5.2 Experimental

MWNTs for the study were prepared by the arc evaporation of graphite at 10 V and 50 A dc [125]. The acid treated MWNTs were prepared by refluxing the MWNTs in a mixture of conc. H_2SO_4 and conc. HNO_3 (2:1 ratio by volume) for one h. The resulting mixture was then allowed to cool and diluted with distilled water. The acid treated MWNTs were then filtered and washed thoroughly with distilled water to remove any traces of the acid. Such nanotubes are always open and contain acidic sites on the surface [126,127]. The chlorination of the acid treated MWNTs was carried out by stirring acid treated MWNTs in thionyl chloride at 100 °C for a day in an argon

atmosphere. The sample was then washed with distilled water and filtered. Similar samples were prepared with MWNTs generated from the pyrolysis of acetylene over iron nanoparticles that were well dispersed over silica [128]. The SWNTs for the experiments were prepared by the method as reported by Journet *et al.* [10]. The acid treated SWNTs were prepared by sonicating the nanotubes in a mixture of conc. H_2SO_4 and conc. HNO_3 (2:1 ratio by volume) for 20 min. The chlorination of the SWNTs was also carried out in the same manner as described earlier for multi-walled nanotubes.

HCl doped polyaniline (PANI) was prepared by the method similar to that of Fite *et al.* [129]. Ammonium persulfate (5.6 g) was dissolved in 100 ml of 1 M aqueous HCl solution and was cooled to 0°C. Aniline (5 ml) was taken in a round bottom flask containing 100 ml of 1M aqueous HCl solution and was cooled to 0°C. The oxidizing agent was slowly added to the aniline solution under sonication at 0°C. The sonication was carried out for another 2 h after the addition of the oxidizing agent. The product was filtered and washed thoroughly with distilled water first and later with methanol to remove the oligomers. The filtered sample was dried under a dynamic vacuum at room temperature for 24 h to ensure the absence of moisture, which affects the conductivity of polyaniline [130]. We have prepared composites of unfunctionalized, acid treated and chlorinated MWNTs and SWNTs with polyaniline. The nanotube-PANI composites were prepared as follows. The nanotubes were added to aniline and sonicated for 15 min and later 1.0M aqueous HCl solution was added. The compositions of the composites of MWNTs are 2:1 and 1:2 by weight of aniline and MWNTs. The PANI-SWNT composites were prepared with a 1:1 ratio of aniline and SWNTs.

The composites and the parent nanotubes were characterized by X-ray powder diffraction (XRD), scanning electron microscopy (SEM), transmission

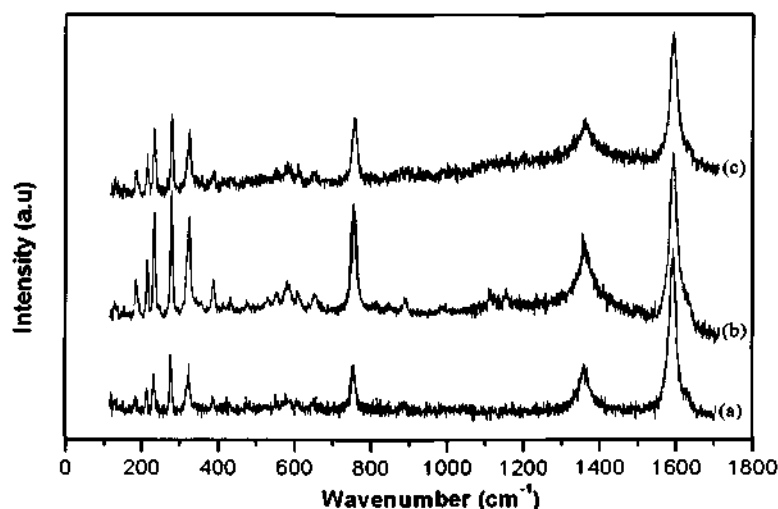


Figure 5.2: Raman spectra of MWNTs-(a) as-prepared,(b) after acid treatment and (c) after chlorination of the surface with thionyl chloride.

electron microscopy(TEM), infrared spectroscopy and Raman spectroscopy. The electric properties were measured by the 4-probe technique between 30°C and -258°C . The powder X-ray diffraction patterns was recorded using a Seifert XRD 3000 TT instrument. All the SEM images were obtained with a Leica S-440I microscope and TEM images with a JEOL JEM 3010 instrument operating at an accelerating voltage of 300 kV. The IR measurements were done on Bruker FT-IR spectrometer. The Raman measurements were performed in a 90 degrees geometry using a Jobin Yvon TRIAX 550 triple grating spectrometer equipped with a cryogenic charge-coupled device camera, using diode-pumped frequency doubled solid state Nd:YAG laser of 532 nm (Model DPSS 532-400, Coherent Inc. USA).

5.3 Results and Discussion

In Figure 5.1, we show the TEM images of pyrolysis MWNTs and SWNTs to illustrate the quality of the nanotubes employed for the preparation of the

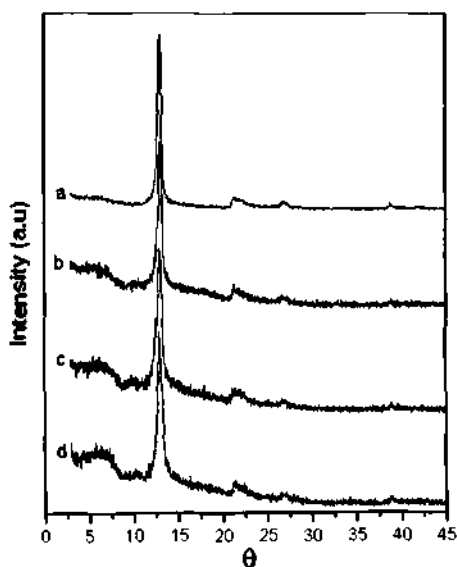


Figure 5.3: XRD patterns of PANI-MWNT (2:1) composites- (a) pristine MWNTs, composite (b) with as-prepared MWNTs, (c) with acid treated MWNTs and (d) with chlorinated MWNTs.

composites with PANI. In Figure 5.2, the Raman spectra of the as prepared MWNTs, acid treated MWNTs and chlorinated MWNTs illustrates how the nanotube character is retained even after various treatments. We observe the E_{2g} in-plane stretching vibration at 1590 cm^{-1} , a shoulder around 1615 cm^{-1} corresponding to the D-line and the 1360 cm^{-1} mode due to the D-line (from sp^3 carbons). In the acid treated MWNTs, the intensity of the 1360 cm^{-1} increases slightly indicating an increase in the number of sp^3 carbons after acid treatment.

Figure 5.3 shows the XRD pattern for MWNTs and polyaniline nanotube composites. The multi-walled carbon nanotubes show only $(hk0)$ and $(00l)$ reflections. The diffraction pattern of multi-walled nanotubes exhibit four major reflections: (002) reflections at 3.435 \AA (which corresponds to the interplanar spacing between the graphene sheets in the nanotubes), (001) reflections at 2.132 \AA with squared Lorentzian line shape, (004) reflection at 1.705 \AA and (110) reflections at 1.231 \AA .

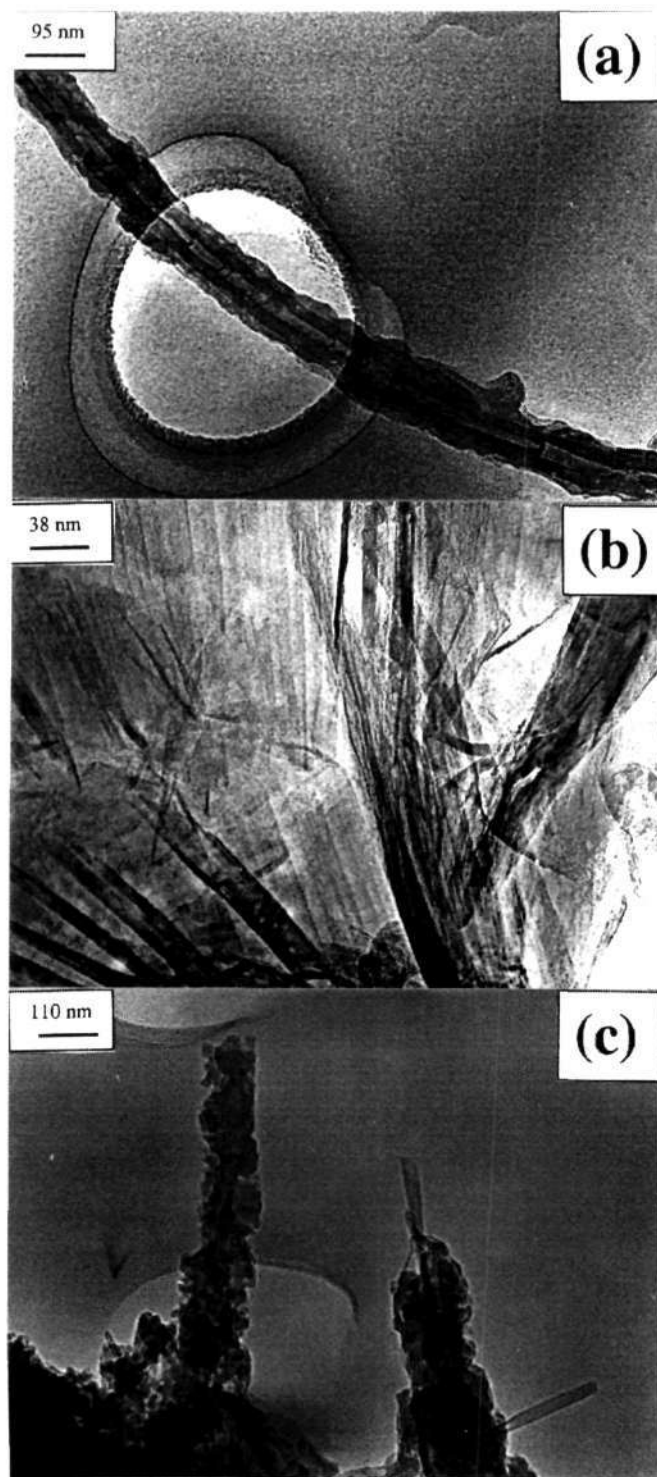


Figure 5.4: TEM images of PANI-MWNT (2:1) composites with: (a) as-prepared MWNTs, (b) acid treated MWNTs and (c) chlorinated MWNTs.

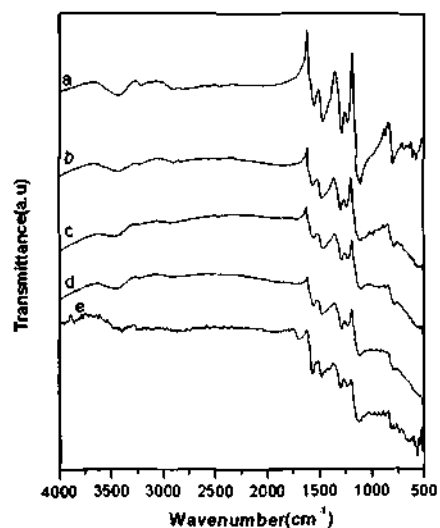


Figure 5.5: IR spectra of PANI-nanotube composites with - (a) PANI, (b) PANI-MWNT (2:1), (c) PANI-acid treated MWNT (2:1), (d) PANI-chlorinated MWNT (2:1) and (e) PANI-chlorinated MWNT (1:2)

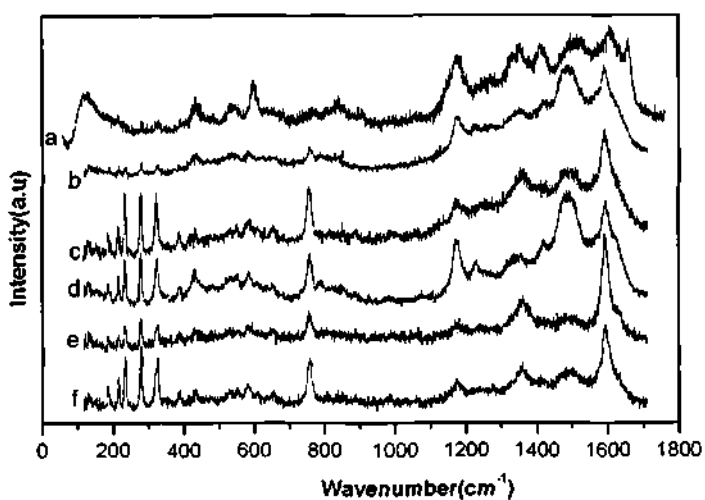


Figure 5.6: Raman spectra of PANI-nanotube composites: (a) as prepared PANI, (b) composite with as prepared MWNTs (2:1), (c) acid treated MWNTs (2:1), and (d) chlorinated MWNTs (2:1), (e) acid treated MWNTs (1:2) and (f) chlorinated MWNTs (1:2).

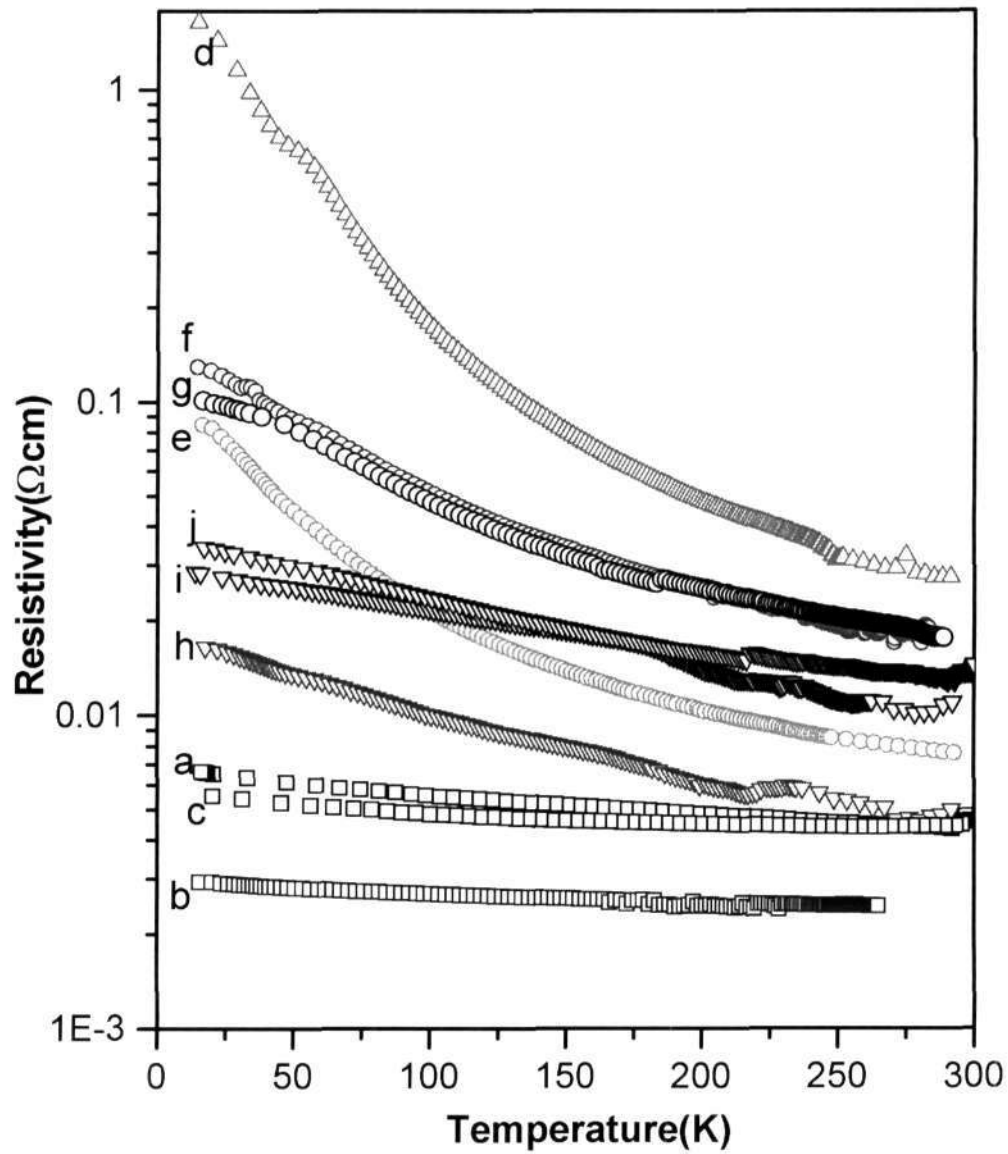


Figure 5.7: Electrical resistivities of PANI-MWNT composites: (a) as prepared MWNTs, (b) acid treated MWNTs, (c) chlorinated MWNTs, (d) PANI, 2:1 composite with (e) as-prepared MWNTs, (f) with acid treated MWNTs and 1:2 composites with (h) as-prepared MWNTs, (i) with acid treated MWNTs and (j) with chlorinated MWNTs

In Figure 5.4a we show the TEM image of a MWNT covered by polyaniline. The TEM image in Figure 5.4b corresponds to the composite of PANI with acid treated MWNTs (2:1). Figure 5.4c shows the TEM image of the PANI-chlorinated MWNTs (2:1) composite. In Figure 5.5, we compare the infrared spectrum of PANI with spectra of the composites of PANI with MWNTs. We do not see any significant changes in the N-H stretching or the N=quinoid=N- bands in the PANI composite with the as prepared MWNTs. Interestingly, the band positions in the IR spectra of the PANI composite with acid treated MWNTs (2:1) and chlorinated MWNTs (2:1) show negligible changes as can be seen from Figures 5.5c and d. The relative intensities of the N=quinoid=N- band, however, are slightly different specially in the spectra the composites of PANI with acid treated and chlorinated MWNTs (Figures 5.5 c-e). We also see an additional band at 1700 cm^{-1} in the spectrum of the PANI-chlorinated MWNT (1:2) composite shown Figure 5.5e.

The Raman spectra of the PANI-nanotube composites shown in Figure 6, we see characteristic bands due to polyaniline along with the nanotube bands. The in-plane deformation (600 cm^{-1}) which is characteristic of the para-disubstituted benzene unit is hardly observed in the composites. There is a significant change in the intensity of the band at 1486 cm^{-1} compared to the band at 1180 cm^{-1} in all the composites. The band at 1180 cm^{-1} is due to the C-H in-plane bending which is characteristic of the para-disubstituted benzene unit and the band at 1486 cm^{-1} corresponds to the C=N stretching of the quinone diimine structure [131]. There appears to be an increase in the quinone diimine units in the PANI composite compared to PANI. In the PANI-MWNT (1:2) composite we observe the expected decrease in the intensities of the parent bands due to PANI.

In Figure 5.7, we compare electrical resistivities of the parent nanotubes with that PANI and the 1:2 composites of PANI with multi-walled nanotubes.

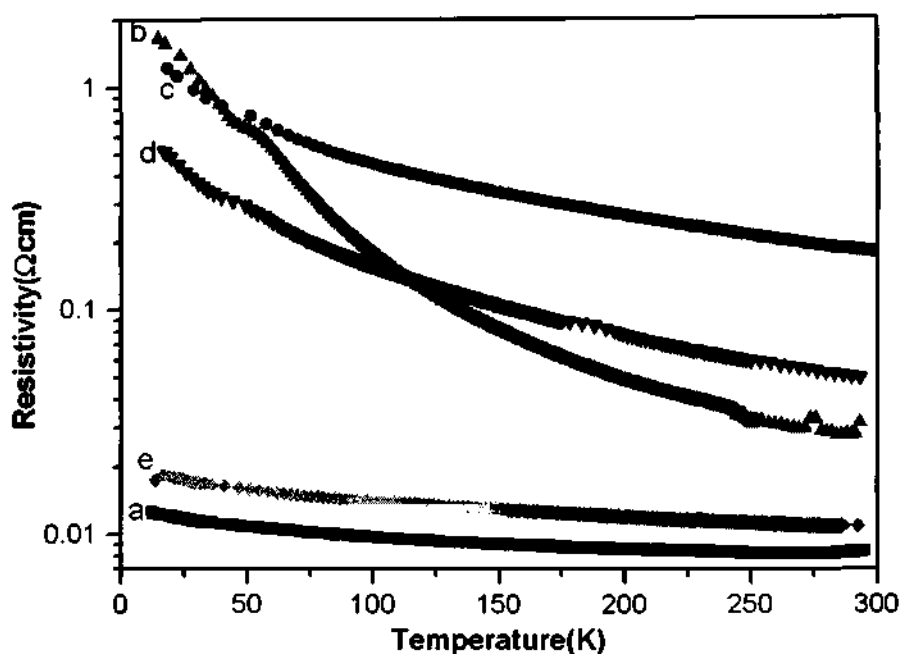


Figure 5.8: Electrical resistivities of PANI-SWNT composites: (a) as prepared SWNTs, (b) PANI, 1:1 composite with (c) as-prepared SWNTs, (d) with acid treated SWNTs and (e) with chlorinated SWNTs.

The resistivities of the MWNTs are low and nearly temperature independent (curves a-c). Polyaniline shows insulating type behavior with a strong temperature dependence of resistivity (curve d). The resistivity of the MWNTs decreases slightly on acid treatment but the resistivity of the chlorinated MWNTs is similar to that of the pristine MWNTs. The resistivities of the 1:2 as well as 2:1 PANI-MWNT composites fall in between the resistivities of PANI and MWNTs (curves e-j). The resistivities of the 2:1 composites show a similar behavior. In Figure 5.8, we show the electrical resistivities of the 1:1 PANI-SWNT composites. The PANI-SWNT (1:1) composite shows a slightly higher resistivity than PANI while the PANI-acid treated SWNT composite shows a resistivity close to that of PANI. The resistivity of the PANI-chlorinated SWNT composite is close to that of the SWNTs.

5.4 Conclusions

Composites of polyaniline with the pristine multi-walled nanotubes as well as acid treated and chlorinated nanotubes can be prepared by the in-situ polymerization of aniline by ammonium persulfate as an oxidizing agent. The PANI-nanotube composites are best characterized by Raman spectroscopy and electron microscopy. The electrical resistivities differ from those of the parent nanotubes or that of PANI. The results show that the electrical resistivity of the PANI-nanotube composites can be manipulated through the variation of the composition as well as by the prior treatment of the nanotubes.

Bibliography

- [1] (a) Special issue on nanostructured materials, *Chem. Mater.*, **8** (1996)
(b) Special issue on nanoscale materials, *Acc. Chem. Res.*, **32** (1999).
(c) Special issue on carbon nanotubes, *Acc. Chem. Res.*, **35** (2002).
- [2] M. Faraday, *Philos. Trans. R. Soc. London.*, **147**, 145 (1857)
- [3] Y. Xia, P. Yang, Y. Sun, Y. Wu, B. Mayers, B. Gates, Y. Yin, F. Kim, H. Yun, *Adv. Mater.*, **15**, 353 (2002).
- [4] H.W. Kroto, J.R. Heath, S.C. O'Brien, R.F. Curl and R.E. Smalley, *Nature*, **318**, 162 (1985).
- [5] W. Kratschmer, L. D. Lamb, K. Fostiropoulos, D. R. Huffman, *Nature*, **347**, 354 (1990).
- [6] S. Iijima, *Nature*, **354**, 6348 (1991).
- [7] D. T. Colbert, J. Zhang, S. M. McClure, P. Nikolaev, J. H. Hafner, D. W. Owens, P. G. Kotula, C. B. Carter, J. H. Weaver, R. E. Smalley, *Science*, **266**, 1218 (1994).
- [8] S. Iijima, T. Ichihashi, *Nature*, **363**, 603 (1993).
- [9] D. S. Bethune, C. H. Kiang, M. S. de Vries, G. Gorman, R. Savoy, J. Vazquez, R. Beyers, *Nature*, **363**, 605 (1993).
- [10] C. Journet, W. K. Maser, P. Bernier, A. Loiseau, M. Lamy de la Chapelle, S. Lefrant, P. Deniard, R. Lee, J. E. Fischer, *Nature*, **388**, 756 (1997).

- [11] A. Thess, R. Lee, P. Nikolaev, H. Dai, P. Petit, J. Robert, C. Xu, Y. H. Lee, S. G. Kim, A. G. Rinzler, D. T. Colbert, G. E. Scuseria, D. Tomnek, J. E. Fischer, R. E. Smalley, *Science*, **273**, 483 (1996).
- [12] C. N. R Rao, B. C. Satishkumar, A. Govindaraj and M. Nath, *ChemPhyChem*, **2**, 78 (2001).
- [13] C. N. R Rao, A. Govindaraj, *Acc. Chem. Res.*, **35**,998 (2002).
- [14] C. N. R. Rao, A. Govindaraj, R. Sen and B. C. Satishkumar, *Mat. Res. Innovat.*, **2**, 128 (1998).
- [15] W.K Hsu, J.P Hare, M. Terrones, H.W. Kroto, D.R.M Walton and P.J.F Harris, *Nature*, **377**, 687 (1995).
- [16] Y. Gogotsi, J. A. Libera, *J. Mater. Res.*, **15**, 2591 (2000).
- [17] M. J. Yacaman, M. M. Yoshida, L. Rendon, T. G. Santiesteban, *Appl. Phys. Lett.*, **62**, 202 (1993).
- [18] V. Ivanov, J. B. Nagy, Ph. Lambin, A. Lucas, X. B. Zhang, D. Bernaerts, G. Van Tendeloo, A. Amelinckx, J. Van Landuyt, *Chem. Phys. Lett.*, **223**, 329 (1994).
- [19] K. Hernadi, A. Fonseca, J. B. Nagy, D. Bernaerts, J. Riga, A. Lucas, *Synth. Met.*, **77**, 31 (1996).
- [20] N. M. Rodriguez, *J. Mater. Res.*, **8**, 3233 (1993).
- [21] W. Z. Li, S. S. Xie, L. X. Qian, B. H. Chang, W. Y. Zhou, R. A. Zhao, G. Wang, *Science*, **274**, 1701 (1996)
- [22] G. Che, B. B. Laxmi, C. R. Martin, E. R. Fisher, R. S. Ruoff, *Chem. Mater.*, **10**, 260 (1998).

- [23] Z. F. Ren, Z. P. Huang, J. W. Wu, J. H. Wang, P. Bush, M. P. Siegal, P. N. Provencio, *Science*, **282**, 1105 (1998).
- [24] R. Sen, A. Govindaraj, C. N. R. Rao, *Chem. Phys. Lett.*, **267**, 276 (1997).
- [25] R. Sen, A. Govindaraj, C. N. R. Rao, *Chem. Mater.*, **9**, 2078 (1997).
- [26] M. Yudasaka, R. Kikuchi, Y. Ohki and S. Yoshimura, *Carbon*, **35**, 195 (1997).
- [27] C. N. R. Rao, R. Sen, B. C. Satishkumar, A. Govindaraj, *Chem Commun.* 1998, 1998 1525.
- [28] B. C. Satishkumar, A. Govindaraj, C. N. R. Rao, *Chem. Phys. Lett.*, **299**, 158 (1999).
- [29] B. C. Satishkumar, A. Govindaraj, P. V. Vanitha, A. K. Raychaudhuri, C. N. R. Rao, *Chem. Phys. Lett.*, **362**, 301 (2002).
- [30] B. C. Satishkumar, P. J. Thomas, A. Govindaraj, C. N. R. Rao, *Appl. Phys. Lett.*, **77**, 2530 (2000).
- [31] F. L. Deepak, A. Govindaraj, C. N. R. Rao, *Chem. Phys. Lett.*, **345**, 5 (2001).
- [32] B. C. Satishkumar, A. Govindaraj, R. Sen, C. N. R. Rao, *Chem. Phys. Lett.*, **293**, 47 (1998).
- [33] H. M. Cheng, F. Li, G. Su, Y. H. Pan, L. L. He, X. Sun and M. S. Dresselhaus, *Appl. Phys. Lett.*, **72**, 3282 (1998).
- [34] H. Dai, A. G. Rinzler, P. Nikolaev, A. Thess, D. T. Colbert, R. E. Smalley, *Chem. Phys. Lett.*, **260**, 471 (1996)
- [35] E. Flahaut, A. Govindaraj, A. Peigney, Ch. Laurent, A. Sousset, C. N. R. Rao, *Chem. Phys. Lett.*, **300**, 236 (1999).

- [36] S. Iijima, *MRS Bulletin*, **19**, 43 (1994).
- [37] S. Amelinckx, A. Lucas, P. Lambin, *Rep. Prog. Phys.*, **62**, 1471 (1999)
- [38] R. Seshadri, A. Govindaraj, H. N. Aiyer, R. Sen, G. N. Subbanna, A. R. Raju, C. N. R. Rao, *Current Science*, **66**, 839 (1994).
- [39] R. A. Jishi, L. Venkataraman, M. S. Dresselhaus, G. Dresselhaus, *Chem. Phys. Lett.*, **220**, 186 (1994).
- [40] A. M. Rao, E. Richter, S. Bandow, P. C. Eklund, K. A. Williams, S. Fang, K. R. Subbaswamy, M. Meno, A. Thess, R. E. Smalley, G. Dresselhaus, M. S. Dresselhaus, *Science*, **275**, 187 (1997)
- [41] M. S. Dresselhaus, G. Dresselhaus, A. Jurio, A. G. Souza Filho, M. A. Pimenta, R. Saito, *Acc. Chem. Res.*, **35**, 1070 (2002).
- [42] M. Endo, H. W. Kroto, *J. Phys. Chem.*, **96**, 6941 (1992).
- [43] T. W. Ebbesen, J. Tabuchi, K. Tanigaki, *Chem. Phys. Lett.*, **191**, 336 (1992).
- [44] S. Iijima, P. M. Ajayan, T. Ichihashi, *Phys. Rev. Lett.*, **69**, 3100 (1992)
- [45] R. T. K. Baker, P. S. Harris, in *Chemistry and Physics of carbon*, eds. P. L. Walker, P. A. Thower (Marcel Dekker), 1978, vol **14**.
- [46] A. Oberlin, M. Endo, T. Koyama, *J. Cryst. Growth*, **32**, 335 (1976)
- [47] J. W. Mintmire, B. I. Dunlap, C. T. White, *Phys. Rev. Lett.*, **68**, 631 (1992).
- [48] N. Hamada, S. Sawada, A. Yoshiyama, *Phys. Rev. Lett.*, **68**, 1579 (1992)
- [49] R. Saito, M. Jujita, G. Dresselhaus, M. S. Dresselhaus, *Appl. Phys. Lett.*, **60**, 2204 (1992)

- [50] J. W. G. Wildoer, L. C. Venema, A. G. Rinzler, R. E. Smalley, C. Dekker, *Nature*, **391**, 59 (1998).
- [51] T. W. Odem, J. L. Huang, P. Kim, C. M. Lieber, *Nature*, **391**, 62 (1998)
- [52] W. Liang, M. Bockrath, D. Bozovic, J. H. Hafner, M. Tinkam, H. Park, *Nature*, **411**, 665 (2001).
- [53] S. J. Tans, A. R. M. Verschueren, C. Dekker, *Nature*, **393**, 49 (1999).
- [54] P. Avouris, *Acc. Chem. Res.*, **35**, 1026 (2002).
- [55] M. Menon, D. Srivastava, *Phys. Rev. Lett.*, **79**, 4453 (1997).
- [56] J. Hone, I. Ellwood, M. Munro, A. Mizel, M. L. Cohen, A. Zettl, A. G. Rinzler, R. E. Smalley, *Phys. Rev. Lett.*, **80**, 1042 (1998).
- [57] P. Kim, L. Shi, A. Majumdar, P. L. McEuen, *Phys. Rev. Lett.*, **87**, 215502 (2001).
- [58] K. H. An, W. S. Kim, Y. S. Park, J. M. Moon, D. J. Base, S. C. Lim, Y. S. Lee, Y. H. Lee, *Adv. Funct. Mater.*, **11**, 387 (2001).
- [59] C. Niu, E. K. Sickel, R. Hoch, D. Moy, H. Tennent, *Appl. Phys. Lett.*, **70**, 1480 (1997).
- [60] R. H. Baughman, C. Cui, A. A. Zakidov, Z. Iqbal, J. N. Berisci, G. M. Spinks, G. G. Wallace, A. Mazzoldi, D. D. Rossi, A. G. Rinzler, O. Jaschinski, S. Roth, M. Kertesz, *Science*, **284**, 1340 (1999).
- [61] A. C. Dillon, K. M. Jones, T. A. Bekkedahl, C. H. Kiang, D. S. Bethune, M. J. Heben, *Nature*, **386**, 377 (1997)
- [62] G. Gundiah, A. Govindaraj, N. Rajalakshmi, K. S. Dhathathreyan, C. N. R. Rao, *J. Mater. Chem.*, **13**, 209 (2003).

- [63] Y. Saito, *J. Nanosci. Nanotech.*, **3**, 39 (2003)
- [64] W. B. Choi, D. S. Chung, J. H. Kang, H. Y. Kim, Y. W. Jin, I. T. Han, Y. H. Lee, J. E. Jung, N. S. Lee, G. S. Park and J. M. Kim, *Appl. Phys. Lett.*, **75**, 3129-3131 (1999)
- [65] R. B. Sharma, V. N. Tondare, D.S. Joag, A. Govindaraj, C.N.R. Rao, *Chem. Phys. Lett.*, **344**, 283 (2001).
- [66] S. R. Mishra, H. S. Rawat, S. C. Mehendale, K. C. Rustagi, A. K. Sood, R. Bandyopadhyay, A. Govindaraj, C. N. R. Rao, *Chem. Phys. Lett.*, **317**, 510 (2000).
- [67] J. J. Davis, K. S. Coleman, B. R. Azamian, C. B. Bagshaw, M. L. H. Green, *Chem. Eur. J.*, **9**, 3732 (2003).
- [68] C. N. R. Rao, F. L. Deepak, G. Gundiah, A. Govindaraj, *Prog. Sol. Sta. Chem.*, **31**, 5 (2003)
- [69] R. S. Wigner, W. C. Ellis, *Appl. Phys. Lett.*, **4**, 89 (1964)
- [70] (a) B. Gates, B. Mayers, B. Cattle, Y. Xia, *Adv. Funct. Mater.*, **12**, 219 (2002); (b) B. Gates, Y. Yin, Y. Xia, *J. Am. Chem. Soc.*, **122**, 12582 (2000)
- [71] U. K. Gautam, M. Nath, C. N. R. Rao, *J. Mater. Chem.*, **13**, 2845 (2003).
- [72] B. Gates, Y. Xia, *J. Mater. Chem.*, **12**, 1875 (2002)
- [73] (a) B. Messer, J. H. Song, M. Huang, Y. Wu, F. Kim, P. Yang, *Adv. Mater.*, **12**, 1526 (2000); (b) J. Song, B. Messer, Y. Wu, H. Kind, P. Yang, *J. Am. Chem. Soc.*, **123**, 9714 (2001).
- [74] A. M. Morales, C. M. Lieber, *Science*, **279**, 208 (1998).

- [75] X. Duan, C. M. Lieber, *Adv. Mater.*, **12**, 298 (2000).
- [76] Z. W. Pan, Z. R. Dai, Z. L. Wang, *Science*, **291**, 1947 (2001).
- [77] Y. Wu, P. Yang, *J. Am. Chem. Soc.*, **123**, 3165 (2001).
- [78] (a) S. T. Lee, N. Wang, Y. F. Zhang, Y. H. Tang, *MRS Bull.*, 36 (1999);
(b) N. Wang, Y. H. Tang, Y. F. Zhang, C. S. Lee, S. T. Lee, *Phys. Rev. B*, **58**, R16024 (1998).
- [79] C. N. R. Rao, G. Gundiah, F. L. Deepak, A. Govindaraj, A. K. Cheemam, *J. Mater. Chem.*, **14**, 440 (2004).
- [80] T. J. Trentler, K. M. Hickman, S. C. Geol, A. M. Viano, P. C. Gibbons, W. E. Buhro, *Science*, **270**, 1791 (1995)
- [81] J. D. Holmes, K. P. Johnston, R. C. Doty, B. A. Korgel, *Science*, **287**, 1471 (2000).
- [82] (a) Y. Wu, P. Yang, *Adv. Mater.*, **13**, 520 (2001); (b) Y. Y. Wu, P. D. Yang, *Appl. Phys. Lett.*, **77**, 43 (2000)
- [83] E. W. Wong, P. E. Sheehan, C. M. Lieber, *Science*, **277**, 1971 (1997).
- [84] (a) X. Duan, Y. Huang, Y. Cui, J. Wang, C. M. Lieber, *Nature*, **409**, 66 (2001); (b) D. H Cobden, *Nature*, **409**, 32 (2001); (c) Y. H. Huang, X. Duan, Y. Cui, L. J. Lauhon, K. H. Kim, C. M. Lieber, *Science*, **294**, 1313 (2001).
- [85] Z. Zhang, X. Sun, M. S. Dresselhaus, J. Y. Ying, *Phys. Rev. B*, **61**, 4850 (2000)
- [86] Y. Huang, X. Duan, Q. Wei, C. M. Lieber, *Science*, **291**, 630 (2001).

- [87] (a) L. D. Hicks, M. S. Dresselhaus, *Phys. Rev. B*, **47**, 16631 (1993); (b) Y. M. Lin, S. B. Cronin, J. Y. Ying, M. S. Dresselhaus, J. P. Heremans, *Appl. Phys. Lett.*, **76**, 3944 (2000)
- [88] J. F. Wang, M. S. Gudixsen, X. F. Duan, Y. Cui, C. M. Lieber, *Science*, **293**, 1455 (2001).
- [89] M. A. El-Sayed, *Acc. Chem. Res.*, **34**, 257 (2001).
- [90] M. Huang, S. Mao, H. Fieck, H. Yan, Y. Wu, H. Kind, E. Weber, R. Russo, P. Yang, *Science*, **292**, 1897 (2001).
- [91] H. Kind, H. Yan, M. Law, B. Messer, P. Yang, *Adv. Mater.*, **14**, 158 (2003).
- [92] (a) M. Glerup, H. Kanzow, R. Almairac, M. Castignolles, P. Bernier, *Chem. Phys. Lett.*, **377**, 293 (2003); (b) M. Glerup, M. Castignolles, M. Holzinger, G. Hug, A. Loiseau, P. Bernier, *Chem. Commun.*, 2542 (2003).
- [93] H. W. Zhu, C. L. Xu, D. H. Wu, B. Q. Wei, R. Vajtai, P. M. Ajayan, *Science*, **296**, 884 (2002).
- [94] P. Muragavel, M. Kalaiselvam, A. R. Raju, C. N. R. Rao, *J. Mater. Chem.*, **7**, 1433 (1997).
- [95] A. R. Raju, H. N. Aiyer, C. N. R. Rao, *Chem. Mater.*, **7**, 225 (1995).
- [96] H. N. Aiyer, A. R. Raju, C.N.R Rao, *Chem. Mater.*, **9**, 755 (1997).
- [97] M. Langlet and J.C Joubert, in *Chemistry of Advanced Materials* (IUPAC monograph) Edited by C.N.R. Rao, Blackwell Scientific publishers, 55 (1993).
- [98] A. Govindaraj, R. Sen, B. V. Nagaraju, C. N. R. Rao, *Phil. Mag. Lett.*, **76**, 363 (1997).

- [99] E. Dujardin, T.W. Ebbesen, A. Krishnan, M. M. Treacy, *Adv. Mater.*, **10**, 611 (1998).
- [100] (a) S. Bandow, A. M. Rao, K. A. Williams, A. Thess, R. E. Smalley, P. C. Eklund, *J. Phys. Chem. B*, **101**, 8839 (1997). (b) K. B. Shelimov, R. O. Esenaliev, A. G. Rinzler, C. B. Huffman, R. E. Smalley, *Chem. Phys. Lett.*, **282**, 429 (1998); (c) A. G. Rinzler, J. Liu, P. Nikolaev, C. B. Huffman, Rodrigues-Macas, P. J. Boul, A. H. Lu, D. Heymann, D. T. Colbert, R. S. Lee, J. E. Fischer, A. M. Rao, P. C. Eklund, R. E. Smalley, *Appl. Phys. A*, **67**, 29 (1998).
- [101] (a) K. Tohji, T. Goto, H. Takahashi, Y. Shinoda, N. Shimizu, B. Jeyadevan, I. Matsuoka, Y. Saito, A. Kasuya, T. Ohsuna, K. Hiraga, Y. Nishina, *Nature*, **383**, 679 (1996); (b) K. Tohji, T. Goto, H. Takahashi, Y. Shinoda, N. Shimizu, B. Jeyadevan, I. Matsuoka, Y. Saito, A. Kasuya, S. Ito, Y. Nishina, *J. Phys. Chem. B*, **101**, 1974 (1997).
- [102] (a) J. L. Zimmerman, R. K. Bradley, C. B. Huffman, R. H. Hauge, J. L. Margrave, *Chem. Mater.*, **12**, 1361 (2000); (b) I. W. Chiang, B. E. Brinson, R. E. Smalley, J. L. Margrave, R. H. Hauge, *J. Phys. Chem. B*, **105**, 1157 (2001); (c) I. W. Chiang, B. E. Brinson, A. Y. Huang, P. A. Willis, A. J. Bronikowski, J. L. Margrave, R. E. Smalley, R. H. Hauge, *J. Phys. Chem. B*, **105**, 8297 (2001).
- [103] A. C. Dillon, T. Gennett, K. M. Jones, J. L. Alleman, P. A. Parilla, M. J. Heben, *Adv. Mater.*, **11**, 1354 (1999).
- [104] M. T. Martinez, M. A. Callejas, A. M. Benito, W. K. Maser, M. Cochet, J. M. Andrs, J. Schreiber, O. Chauvet, J. L. G. Fierro, *Chem. Commun.*, 1000 (2002).

- [105] R. Sen, S. M. Rickard, M. E. Itkis, R. C. Haddon, *Chem. Mater.*, **15**, 4273 (2003).
- [106] J. G. Whitshire, A. N. Khlobystov, L. J. Li, S. G. Lyapin, G. A. D. Briggs, R. J. Nicholas, *Chem. Phys. Lett.*, 2004, **386**, 239 (2004).
- [107] M. J. O'Connell, S. M. Bachilo, C. B. Huffman, V. C. Moore, M. S. Strano, E. H. Haroz, K. L. Rialon, P. J. Boul, W. H. Noon, J. Ma, R. H. Hauge, R. B. Weisman, R. E. Smalley, *Science*, **297**, 593 (2002).
- [108] D. A. Mawlawi, C. Z. Liu, M. Moskovits, *J. Mater. Res.*, **9**, 1014 (1994).
- [109] K. Nielsch, F. Mullet, A-P Li, U. Gosele, *Adv. Mater.*, **12**, 582 (2000).
- [110] A. Govindaraj, B. C. Satishkumar, M. N. Nath, C. N. R. Rao, *Chem. Mater.*, **12**, 202 (2000).
- [111] B. D. Busbee, S. O. Obare, C. J. Murphy, *Adv. Mater.*, **15**, 414 (2003).
- [112] Y. Sun, B. Gates, B. Mayers, Y. Xia, *Nano Lett.*, **2**, 165 (2002).
- [113] K. Soulantica, A. Maisonnat, F. Senocq, M. C. Fromen, M. J. Casanove, B. Chaudret, *Angew. Chem. Int. Ed.*, **40**, 2984 (2001).
- [114] Y. Wang, L. Zhang, G. Meng, C. Liang, G. Wang, S. Sun, *Chem. Commun.*, 2632 (2001).
- [115] Y. Yan, P. Liu, M. J. Romero, M. M. A. Jassim, *J. Appl. Phys.*, **93**, 4807 (2003).
- [116] Y. Wang, T. Herricks, Y. Xia, *NanoLett.*, **3**, 1163 (2003).
- [117] B. Gates, Y. Wu, Y. Yin, P. Yang, Y. Xia, *J. Am. Chem. Soc.*, **123**, 11500 (2001).
- [118] M. H. Huang, Y. Wu, H. Feick, N. Tran, E. Weber, P. Yang, *Adv. Mater.*, **13**, 113 (2001).

- [119] J. Zhang , L. Sun , C. Liao, C. Yan, *Chem. Commun.*, 262 (2002).
- [120] G. Gundiah, S. Mukhopadhyay, U. G. Tumkurkar, A. Govindaraj, U. Maitra, C. N. R. Rao, *J. Mater. Chem.*, **13**, 2118 (2003).
- [121] R. C. Haddon(Ed.), Special issue on carbon nanotubes, *Acc. Chem. Res.*, **35**, 997 (2002).
- [122] C. Downs, J. Nugent, P. M. Ajayan, D. J. Duquette, K. S. V. Santhanam , *Adv. Mater.*, **11**, 1028 (1999).
- [123] M. Cochet, W. K. Maser, A. M. Benito, M. A. Callejas, M. T. Martnez, J-M. Benoit, J. Schreiber, S. Lefrant, O. Chauvet, *Chem Commun.*, 1450 (2001).
- [124] H. Zengin, W. Zhou, J. Jin, R. Czerw, D. W. Smith Jr, L Echevoyen, D. L. Carroll, S.H. Foulger, J. Ballato, *Adv. Mater.*, **14**, 1480 (2002).
- [125] C. N. R. Rao, R. Seshadri, A. Govindraj, R. Sen, *Mater. Eng.* **R15**, 209 (1995).
- [126] S. C. Tsang, Y. K. Chen, P. J. F. Harris, M. L. H. Green, *Nature*, **372**, 159 (1994).
- [127] B. C. Satishkumar, A. Govindraj, J. Mofokeng, G. N. Subbana, C. N. R. Rao, *J. Phy B*, **29**, 4925 (1996).
- [128] M. Nath, B. C. Satishkumar, A. Govindraj, C. P. Vinod, C. N. R. Rao, *Chem. Phy. Let.*, **322**, 333 (2000).
- [129] C. Fite, Y. Cao, A. J. Heeger, *Solid State Com.*, **70**, 245 (1989).
- [130] A. G. MacDiarmid, A. J. Epstein , *Faraday Discuss. Chem Soc.*, **88**, 317 (1989).

-
- [131] Y. Furukawa, F. Ueda, Y. Hyodo, I. Harada, T. Nakajima, T. Kawagoe,
Macromolecules, **21**, 1297 (1988).

620.173

1988